Dark Matter Indirect Detection and Bremsstrahlung Processes

Thomas David Jacques

Submitted in total fulfilment of the requirements
of the degree of Doctor of Philosophy

August 2011

School of Physics
The University of Melbourne

Abstract

It is now well established that some form of Dark Matter (DM) makes a sizeable contribution to the total matter-energy abundance of the Universe, yet DM still evades detection and its particle properties remain unknown. Indirect detection provides an important probe of some of these fundamental properties. DM self-annihilation throughout the Universe is expected to lead to an observable signal of standard model particles at Earth, and any observed flux of standard model particles from a particular region acts as an upper limit on the annihilation signal from that region.

In Chapter 1, we give an introduction to our current knowledge of DM. We begin with the historic and recent evidence for the existence of DM based on its gravitational effects, before describing our current knowledge of DM formation history and abundance. We then describe and compare a number of competing DM density profiles for our galaxy, highlighting the large uncertainties towards the Galactic center. There are currently a large number of DM candidates, sometimes called the 'Candidate Zoo'. We briefly introduce several of the most popular candidates, describing their history and motivation. We then move on to describe current searches for DM, focusing on indirect detection, which aims to detect DM via an observable flux of its SM annihilation products. We detail the major constraints on the DM self-annihilation cross section, and examine some potential signals from DM annihilation. We also describe constraints on DM from direct detection and collider searches. Finally, we introduce bremsstrahlung processes in the context of DM annihilation,

where a particle such as a gamma-ray is radiated from one of the DM annihilation products at the Feynman diagram level.

In Chapter 2, we use gamma-ray data from observations of the Milky Way, Andromeda (M31), and the cosmic background to calculate robust upper limits on the dark matter self-annihilation cross section to monoenergetic gamma rays, $\langle v\sigma \rangle_{\gamma\gamma}$, over a wide range of dark matter masses. We do this in a model-independent and conservative way, such that our results are valid across a broad spectrum of DM models and astrophysical assumptions. In fact, over most of this range, our results are unchanged if one considers just the branching ratio to gamma rays with energies within a factor of a few of the endpoint at the dark matter mass. If the final-state branching ratio to gamma rays, $Br(\gamma\gamma)$, were known, then $\langle v\sigma \rangle_{\gamma\gamma}/Br(\gamma\gamma)$ would define an upper limit on the *total* cross section.

In Chapter 3, we take advantage of the fact that annihilation to charged leptons will inevitably be accompanied by gamma rays due to radiative corrections to place similar limits on the the annihilation cross section to an electron-positron pair, $\langle v\sigma \rangle_{e^+e^-}$. Photon bremsstrahlung from the final state particles occurs at the Feynman diagram level, yet the gamma-ray spectrum per annihilation is approximately model independent, such that our analysis applies to a broad class of DM models. We compare the expected annihilation signal with the observed gamma-ray flux from the Galactic Center, and place conservative upper limits on the annihilation rate to an electron-positron pair. We also constrain annihilation to muon and tau lepton pairs. We again make conservative choices in the uncertain dark matter density profiles, and note that our constraints would only be strengthened if the density were more tightly constrained. The spectrum per annihilation produces hard gamma rays near the kinematic cutoff, and we find that the constraints on $\langle v\sigma \rangle_{e^+e^-}$ are weaker than those on $\langle v\sigma \rangle_{\gamma\gamma}$ only by a factor of $\sim 10^{-2}$, as expected since the $2 \rightarrow 3$ process is suppressed relative to the $2 \rightarrow 2$ process.

Annihilation to leptons will also be accompanied by massive gauge bosons due to electroweak radiative corrections. In Chapter 4 we examine a case where DM annihilates exclusively to neutrinos at the $2 \to 2$ level, and gamma rays, leptons and hadrons will inevitably be produced due to electroweak bremsstrahlung. We explicitly calculate the ratio of the rate for the three electroweak bremsstrahlung modes $\chi\chi \to \nu\bar{\nu}Z$, $e^+\nu W^-$ $e^-\bar{\nu}W^+$ to the rate for the $2 \to 2$ process $\chi\chi \to \nu\bar{\nu}$.

Electroweak bremsstrahlung plays a larger role in the special case where the annihilation rate to leptonic modes suffers helicity suppression. While it has long been known that photon bremsstrahlung can lift the helicity suppression, we show in Chapter 5 that electroweak bremsstrahlung is also capable of lifting this suppression, such that the branching ratio to the 3-body electroweak bremsstrahlung final states can greatly exceed the branching ratio to an electron-positron or neutrino pair. We explicitly calculate the electroweak bremsstrahlung cross section in a typical leptophilic model.

In Chapter 6 we examine observational signatures of dark matter annihilation in the Milky Way arising from these electroweak bremsstrahlung contributions to the annihilation cross section. Here we calculate the spectra of stable annihilation products produced via $\gamma/W/Z$-bremsstrahlung. After modifying the fluxes to account for the propagation through the Galaxy, we set upper bounds on the annihilation cross section via a comparison with observational data. We show that stringent cosmic ray antiproton limits preclude a sizable dark matter contribution to observed cosmic ray positron fluxes in the class of models for which the bremsstrahlung processes dominate.

Declaration

This is to certify that:

(i) the thesis comprises only my original work towards the PhD except where indicated in the Preface,

(ii) due acknowledgement has been made in the text to all other material used,

(iii) the thesis is less than 100,000 words in length, exclusive of tables, maps, bibliographies, appendices and footnotes.

Thomas David Jacques

Date: / /

Preface

This thesis is comprised of seven main chapters (not including supplementary materials such as the bibliography and appendices). Chapter 1 is an original literature review. Chapters 2, 3, 4 and 6 are based on Publications 1, 3, 2 and 5 respectively, while Chapter 5 is based on Publications 4 and 6 (see Page 141 for the publication list). Chapter 7 is the conclusion.

These publications were done in collaboration with N. Bell (Publications 1, 2, 3, 4, 5, 6), J. Dent and T. Weiler (Publications 2, 4, 5 and 6), J. Beacom, G. Mack and H. Yuksel (Publication 1), A. Galea and L. Krauss (Publication 6). While J. Beacom, N. Bell and T. Weiler are responsible for the original inspiration for many of these publications, all calculations, results and analyses are my own work, with the exception of Section 5.2 and Appendices A, B and C, where T. Weiler made a significant contribution.

Acknowledgements

My heartfelt thanks go to my supervisor Nicole Bell, who has been my mentor and guide through this journey and without whom none of this would have been possible. To all of my collaborators, Ahmad Galea, Greg Mack, Hasan Yuksel, James Dent, John Beacom, Lawrence Krauss and Tom Weiler, it has been a great pleasure to work with you, and I look forward to continuing that work in the future. To Ray Volkas and Andrew Melatos, the other members of my advisory panel, thank you for providing the valuable gifts of perspective and motivation. To Damien George, Ben Carson, Sandy Law and Andrew Coulthurst, thank you for welcoming me into the group when I first arrived, and being ideal role models as I found my feet. Jayne Thompson and Nadine Pesor, thank you for being such wonderful office mates and peers through both good times and not so good. To Nick Setzer, Kallia Petraki, Benedict von Harling, Donatello Dolce and all of the academics and postdocs in TPP, thank you for sharing your wisdom and experience. To all the other members of TPP, and all of my fellow students in the School of Physics, thank you for making my time here a wonderful experience I will always treasure. And not least, thank you to my parents, whose love and support have always been there for me.

Contents

List of Figures

1

Introduction to Dark Matter

It is now well established that the Universe consists of more than the observable baryonic matter. The identity of the dark component is one of the greatest mysteries in physics. At present, it is believed that the Universe is primarily made up of some form of dark energy or cosmological constant, responsible for the present day accelerating expansion of the Universe, while the matter content consists mostly of some unknown Dark Matter (DM), the focus of this thesis, with baryonic matter contributing only a small fraction to the total matter-energy content of the Universe.

1.1 Evidence, Abundance and Structure

1.1.1 Rotation Curves

Some of the most convincing evidence for the existence of DM comes from observations of the rotation curves of nearby galaxies. The rotational velocity at radius r is related to the mass enclosed within that radius $M(r)$,

$$v = \sqrt{\frac{G_N\,M(r)}{r}}, \tag{1.1}$$

where $G_N = 6.67 \times 10^{-11}\mathrm{m}^3\,\mathrm{kg}^{-1}\,\mathrm{s}^{-2}$. The rotational velocity as a function of radius is usually measured via redshift of the neutral Hydrogen 21 cm line [3], and

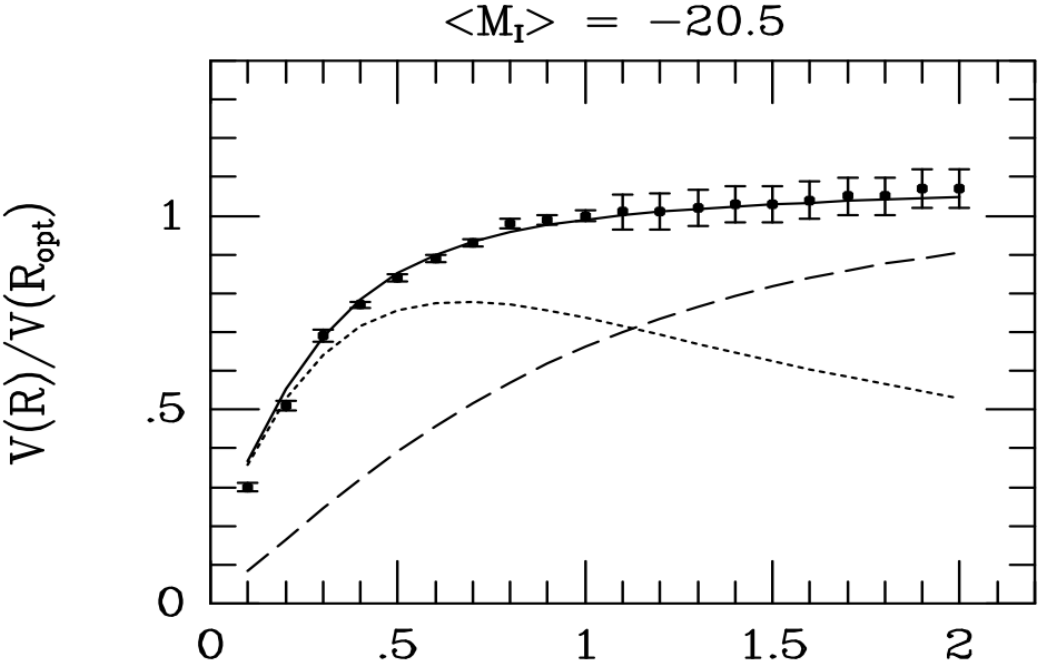

Figure 1.1: Best fits to the universal rotation curve from Ref. [1], for galaxies within a luminosity bin centered on $\langle M_I \rangle = -20.5$. Dotted line shows contribution from the luminous disk, dashed line from the dark halo.

compared with the velocity expected from observation of the distribution of luminous matter. Ref. [1] has calculated rotation curves for a compilation of hundreds of spiral galaxies, and confirms the strong evidence for a non-luminous component to the galactic mass. If there were no DM, the rotational velocity would fall beyond R_{opt}, defined as the radius containing the bulk of the luminosity of the galaxy. Instead, the rotational velocity becomes roughly constant beyond R_{opt}, implying that there is a dark component to the mass, contributing to a total mass proportional to r. The rotation curve for a compilation of galaxies falling into the $\langle M_I \rangle = -20.5$ luminosity bin is shown in Fig. 1.1 from Ref. [1].

1.1.2 Mass to Light Ratio of Clusters

The first evidence for the existence of DM came from observations of the Coma cluster of galaxies by Fritz Zwicky in 1933 [4, 5]. The virial theorem relates the kinetic energy E_K of a system with the potential energy V_{pot}. In an idealized system, $E_K = -\frac{1}{2}V_{pot}$, and this is used in conjunction with measurements of the dispersion of the radial velocities of galaxies within the cluster to derive the total mass. Zwicky compared this with the mass derived from observation of the total luminosity, finding a mass-to-light ratio of some 400 solar masses per solar luminosity, well above that expected if the cluster were composed solely of baryonic matter.

1.1.3 Gravitational Lensing

According to Einstein's theory of general relativity, light will propagate along geodesics which become curved in the presence of large concentrations of mass. This results in a lensing effect when there is a large mass between a light source and the observer, with the angle of deflection proportional to the mass of the object causing the lensing. For example, Ref. [6] uses data from the Hubble Space Telescope [7] to make detailed maps of the mass distribution of the galaxy cluster 0024+1654.

Observation of multiple images of the light source is called strong lensing, while weak lensing is the distortion of the image of the light source. Microlensing is an effect where no distortion is seen, but a background star briefly appears brighter due to the passing of a transient lensing object. For a review of the theory of gravitational lensing, see e.g. Ref. [8].

Recent observations of the pair of colliding galaxy clusters 1E0657-558, known colloquially as the Bullet Cluster, have provided some of the best observational evidence yet for dark matter [9]. Observations by the Chandra X-ray observatory [10] show that the intergalactic hot gas which makes up the bulk of the luminous baryonic matter of the clusters collided and interacted as the clusters passed through each other. However, gravitational lensing calculations performed using 5 optical image data sets show that the vast bulk of the mass of these clusters is no longer coincident with the luminous matter to a significance of 8σ, and did not interact as the cluster collided. This is, by definition, dark matter: non-luminous matter that is only weakly interacting. This is the first conclusive observation of a structure that has had its luminous matter stripped from the bulk of the mass, allowing separate observations of the two regions. Observations of other colliding clusters have since provided further evidence for the existence of DM [11, 12].

Microlensing has been used to constrain the prevalence of MACHOs (Massive Compact Halo Objects), which had been proposed as a DM candidate. These are small astrophysical objects such as planets or dead stars that emit little or no light. The prevalence of MACHOs, and their potential as a DM candidate, have been mostly ruled out by searches in the Magellanic Clouds. Only a few lensing events were seen, and MACHOs can only account for a tiny fraction of the DM [13, 14].

1.1.4 Cosmic Microwave Background

The best measurements of the DM abundance and the composition of the Universe come from observations of the cosmic microwave background (CMB), a remnant of the thermal plasma of the early Universe. Before recombination of electrons and protons into neutral hydrogen, electromagnetic interactions coupled photons and baryons into a fluid. Since recombination at $T \sim 3000K \sim 1\,\mathrm{eV}$, the CMB photons have been freely propagating throughout the Universe.

It is relatively easy to convert between the photon spectrum from the era of recombination and the CMB now. The CMB spectrum is remarkably close to a blackbody of temperature 2.726 K, and is isotropic at the level of 10^{-5}. However, recent high-precision observations of the CMB, such as those by the Wilkinson Microwave Anisotropy probe (WMAP), detail anisotropies or fluctuations in the temperature and polarisation, which provide a good determination of several cosmological parameters [15, 16].

Quantum fluctuations of the inflaton field lead to fluctuations in the photon and matter distributions. This in turn leads to temperature and polarisation anisotropies in the CMB today, as photons in deeper gravitational potential wells will have less energy today than those escaping areas of lower gravity.

Anisotropies in the CMB are measured via the angular power spectra of the temperature and polarization maps. These spectra shows a number of peaks, the location of which are strongly dependent on the cosmological matter and energy abundances. In combination with data from the Sloan Digital Sky Survey [17] and the Hubble Space Telescope [7], WMAP provides precise determination of these quantities [16, 18]

$$\begin{aligned} \Omega_b h^2 &= 0.02260 \pm 0.00053, & \Omega_M h^2 &= 0.1334^{+0.0056}_{-0.0055}, \\ \Omega_\Lambda &= 0.728^{+0.015}_{-0.016}, & \Omega_{\rm tot} &= 1.0023^{+0.0056}_{-0.0054}, \end{aligned} \tag{1.2}$$

where $\Omega_i \equiv \rho_i/\rho_c$ is the abundance in units of the critical density, ρ_c, which corresponds to a geometrically flat Universe, the Hubble parameter is defined as $h = H_0/(100\,\mathrm{km\,s^{-1}Mpc^{-1}}) = 0.704^{+0.013}_{-0.014}$ [16], and Ω_b, Ω_M, Ω_Λ, $\Omega_{\rm tot}$ are the baryonic, total matter, dark energy and total matter-energy abundances respectively.

The DM makes up the difference between the baryon and total matter abundances, showing that DM dominates the matter content of the Universe. Note that these measurements suggest a flat or very nearly flat universe, $\Omega_{\rm tot} \simeq 1$.

1.1.5 Thermal Relic Dark Matter

If DM is produced thermally in the early universe, it is called a thermal relic, and its formation history is well understood. At high temperatures $T > m_\chi$, when the annihilation rate of dark matter is sufficiently large compared with the expansion rate of the universe, the dark matter has a thermal distribution, and thus has an abundance roughly equal to that of photons. The annihilation rate matches the production rate, and the DM remains in thermal equilibrium. As the universe expands, the temperature drops below the DM mass, so that the abundance of DM becomes Boltzmann suppressed, by a factor proportional to $e^{-m_\chi/T}$.

Eventually the annihilation rate cannot keep up with the expansion of the universe, thermal equilibrium cannot be maintained, and the particle is said to be decoupled; Annihilation drops dramatically and the abundance stabilises. This is known as freezeout, and the abundance and cross section of DM at freezeout determines the relic abundance today.

The relic density (density today of a thermal relic) can then be calculated using the annihilation cross section and entropy considerations, with the final result from e.g. [19, 20, 21]

$$\Omega_{DM}h^2 \approx \frac{3\times 10^{-27}\text{cm}^3\,\text{s}^{-1}}{\langle v\sigma\rangle}. \tag{1.3}$$

where we define σ as the self-annihilation cross section, $\sigma \equiv \sigma_A$, unless otherwise stated, and $\langle v\sigma\rangle$ is the thermal average of the product of the DM self-annihilation cross-section and velocity. If the DM has a thermal distribution, this thermal average can be performed in the non-relativistic limit using the formula [19]

$$\langle v\sigma\rangle = \frac{2}{\sqrt{\pi}}\left(\frac{m_\chi}{T}\right)^{\frac{3}{2}}\int_0^\infty v_{\text{lab}}\sigma\sqrt{\epsilon}e^{-m_\chi\epsilon/T}d\epsilon, \tag{1.4}$$

where T is the temperature of the DM thermal distribution, m_χ is the DM mass, $\epsilon = v_{\text{rel}}^2/(1-v_{\text{rel}}^2)$ and v_{rel} is the relative velocity of the DM particles. Note that $\langle v\sigma\rangle \neq v\sigma$ and they should not be used interchangeably. For brevity, we describe both as 'the cross section', although it should be clear from context which we are referring to.

Using current measurements of $\Omega_{DM}h^2 \simeq 0.11$ (see Section 1.1.4), the cross section required for dark matter to be a thermal relic is $\langle v\sigma\rangle \approx 3\times 10^{-26}$ cm^3 s^{-1}.

It is not certain that dark matter is indeed a thermal relic, and there are effects that could lead to a thermal relic dark matter having a higher or lower cross section, so this is by no means a definitive statement of the dark matter cross section. For example, Kaplinghat, Knox and Turner [22] propose a very high cross section, and suggest ways that the dark matter could remain a thermal relic. The first suggestion is that dark matter is produced late, from decays or annihilations of a heavier particle. This places constraints on the lifetime and mass of the heavier particle, to ensure that the decay products do not effect the matter/radiation energy density ratio of the universe. The second proposal is that the mass of dark matter or its annihilation products changes over time, so that if the dark matter were to rise above some threshold, or the mass of the annihilation product were to drop below the threshold, annihilation would move from being impossible to possible, modifying the relic density calculations.

Formulae used throughout this work to determine the DM annihilation signal assume equal abundances of DM and its antiparticle (or alternatively, the existence of Majorana DM, which is its own antiparticle.) However, there are scenarios where this is not the case, for example if a matter-antimatter asymmetry was established in the dark sector in the early universe. Since these models have a large matter-antimatter asymmetry, prospects for indirect detection are greatly reduced.

1.1.6 Large Scale Structure

A standard paradigm for large scale structure formation has emerged in the form of ΛCDM, which incorporates dark energy, cold DM, and inflation. The early structure of the universe appears to be remarkably uniform, based on the isotropy of the CMB down to a level of 10^{-5} [18]. After the radiation-dominated epoch ends and matter density overtakes radiation density, gravity amplifies the small anisotropies in the matter distribution, causing small structures to form. As objects grow, this process accelerates, leading to highly overdense and underdense regions, and causing structure on all scales from planets and solar systems to filaments of clusters of galaxies.

Unfortunately, complete predictions for the evolution of structure cannot currently be tested analytically. Instead, we rely on numerical N-body simulations that use theoretical initial conditions for structure formation and measurements from the CMB (see Section 1.1.4) as input, and simulate the clustering of gravitationally interacting DM over time. For example, the *Millennium-II Simulation* [23] simulates approximately 10^{10} DM particles in a box with sides of length 100 h^{-1} Mpc, and is remarkably consistent with observations by large scale sky surveys.

Conversely, models of Hot Dark Matter (HDM) where the DM is composed of relativistic particles are inconsistent with observations and current models of structure formation. HDM suppresses structures in the early universe which are smaller than the free streaming length $L \sim 40\,\mathrm{Mpc}\,(m_\nu/30\,\mathrm{eV})$, as they quickly move from overdense regions [24]. This is the 'top-down' approach to structure formation, where largest scale structure forms first, eventually fragmenting to greater levels of structure on smaller scales, which is inconsistent with observations of high redshift galaxies.

1.1.7 Within Galaxies

There is still a great deal of uncertainty in the dark matter density profile of galaxies, particularly toward the center. However, one common parameterization has emerged:

$$\rho(r) = \left(\frac{r_s}{r}\right)^{\gamma} \frac{\rho_0}{[1+(r/r_s)^{\alpha}]^{(\beta-\gamma)/\alpha}}. \tag{1.5}$$

The parameters for the commonly adopted Isothermal [25, 26], Kravtsov [27], Navarro Frenk and White (NFW) [28], and Moore [29] profiles are given in Table 1.1. The parameters (α, β, γ) are standard across galaxies, while r_s is given for the Milky Way. The scale radius r_s is the radius at which the slope of the profile changes. The normalization factor ρ_0 is chosen to give the correct local density, $\rho_\odot = \rho(R_{sc})$, where $R_{sc} = 8.5$ kpc is the distance from the solar system to the center of the Milky Way. In Chapters 2 and 3, we adopt the normalisation from Ref. [2], specifically $\rho_\odot = 0.27\,\mathrm{GeV\,cm^{-3}}$ for the Moore profile, $\rho_\odot = 0.3\,\mathrm{GeV\,cm^{-3}}$ for the NFW profile, and $\rho_\odot = 0.37\,\mathrm{GeV\,cm^{-3}}$ for the Kravtsov profile. In all other cases we adopt a universal normalization, $\rho_\odot = 0.39$ GeV cm^{-3} from Ref. [30], but this could be a factor of ~ 2 higher or lower [31, 32, 33]. In addition, the Einasto profile [34, 35]

Profile	α	β	γ	r_s in kpc
Isothermal	2	2	0	5
Kravtsov	2	3	0.4	10
NFW	1	3	1	20
Moore	1.5	3	1.5	28

Table 1.1: Density Profile Parameters for the Milky Way. See text for description.

does not fit Eq. 1.5, and is instead given by

$$\rho_0 \, \mathrm{Exp}\left[\frac{-2}{\alpha}\left(\left(\frac{r}{r_s}\right)^{\alpha}-1\right)\right] \tag{1.6}$$

where $\alpha = 0.17$, and the scale radius is uncertain, but approximately $r_s \simeq 20$ kpc. These five density profiles are plotted in Fig. 1.2.

If there is any ‘canonical’ profile, it is the NFW profile. This profile is based on high-resolution N-body simulations of the formation of galactic structure using the standard cold dark matter model, and goes like $1/r$ towards the galactic center. The Einasto and Moore profiles are also based on N-body simulations. The Moore profile has a much larger central cusp, and the Einasto profile is very similar to the NFW profile at moderate to large radii, whilst flattening out and avoiding the cusp at very small radii. Due to the singularity at the core, we specify a cut-off radius, below which we set density to be constant, $\rho(r \leq r_{\mathrm{cutoff}}) = \rho(r_{\mathrm{cutoff}})$. Our calculations in the following chapters do not focus on very small regions around the galactic center, and are not sensitive to the precise location of the cutoff, which we set at 0.01 pc.

The Kravtsov profile is less commonly adopted. This profile is much shallower towards the galactic center. It is based on observations of the rotation curves of Low Surface Brightness (LSB) and Dwarf galaxies, whose mass is dominated by dark matter ($\sim 85\%$ of total mass is dark). This eliminates assumptions about the mass-to-light ratio and contribution to the rotation curves of luminous matter, as they are able to treat these contributions as negligible. These profiles were then compared to N-body simulations of structure formation, and found to be consistent. The

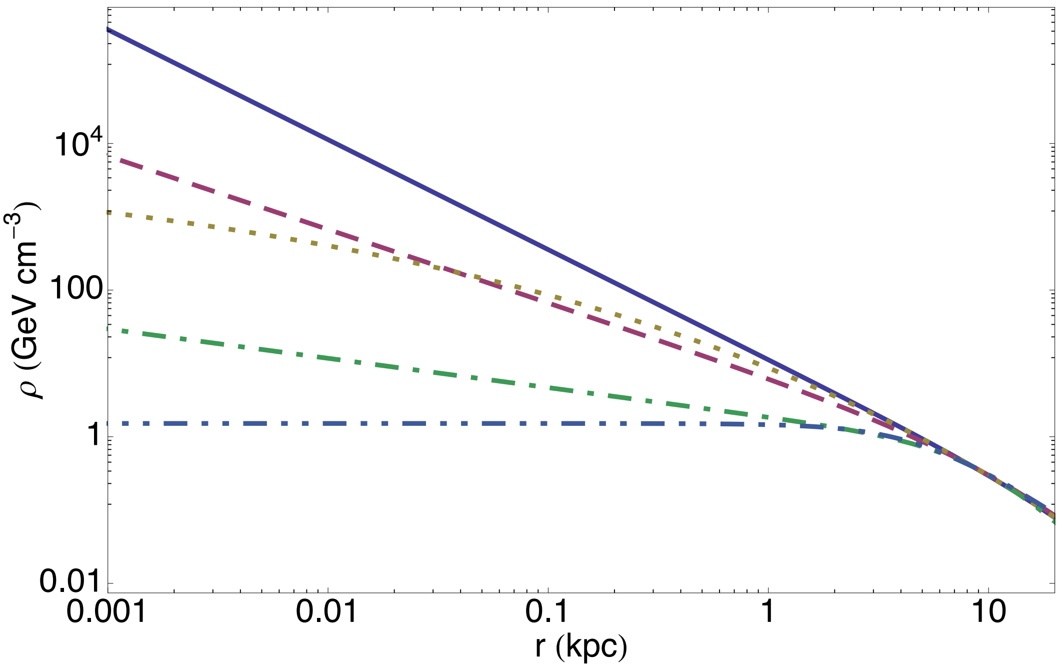

Figure 1.2: The DM density $\rho(r)$ of the Milky Way, showing the Moore (solid), NFW (dashed), Einasto (dotted), Kravtsov (dot-dashed) and Isothermal (dot-dot-dashed) profiles described in the main text.

Isothermal profile is an earlier ‘canonical’ empirical profile based on an isothermal sphere with a flat central core, avoiding a singularity at small radii.

For large radii $r \gtrsim r_s$, all five profiles scale with radius as $1/r^3$ and are normalized such that they coincide closely. However, the profiles diverge at small radii, scaling as $1/r^{0.4}$, $1/r$ and $1/r^{1.5}$ for the Kravtsov, NFW and Moore profiles respectively. The steep Moore profile thus features a greatly enhanced density near the Galactic Center, compared to the relatively flat Kravtsov and Isothermal profiles; the NFW profile falls between the two.

There is an apparent discrepancy between the theory and observation of small-scale power. Simulations such as “Via Lactea" [36] tend to predict large amounts of small-scale structure, finding that dark matter will clump within galaxies, forming mini-halos, galactic satellites and central cusps, while observations show a smoother profile. There are several potential solutions to this problem. For example, warm DM, an intermediate scenario between highly relativistic and non-relativistic DM, can reduce small-scale power; see e.g. Ref [37] and references therin. Late-decaying DM can boost the DM velocity, which can reduce the circular velocity of dwarf haloes, bringing simulated numbers in line observations [38], or heat haloes, reducing cusp size [39]. Alternatively, there may be an astrophysical explanation. For example, tidal forces between luminous and dark matter could reduce the prevalence of substructure [40]. Interestingly, Ref. [41] shows that direct detection constraints (see Section 1.4.1) should be valid in the presence of substructure, even if analyses assume a smooth halo profile.

The observed flux of DM annihilation products is proportional to the integral along the line of sight of the DM density squared, and so it is useful to define such an integral, along the line of sight at an angle ψ from the Galactic Center,

$$\mathcal{J}(\psi) = \mathrm{J}_0 \int_0^{\ell_{max}} \rho^2 \left(\sqrt{R_{\rm sc}^2 - 2\ell R_{\rm sc} \cos\psi + \ell^2} \right) d\ell \,, \tag{1.7}$$

where $\mathrm{J}_0 = 1/[8.5\,\mathrm{kpc} \times (0.3\,\mathrm{GeV\,cm^{-3}})^2]$ is an arbitrary normalization constant used

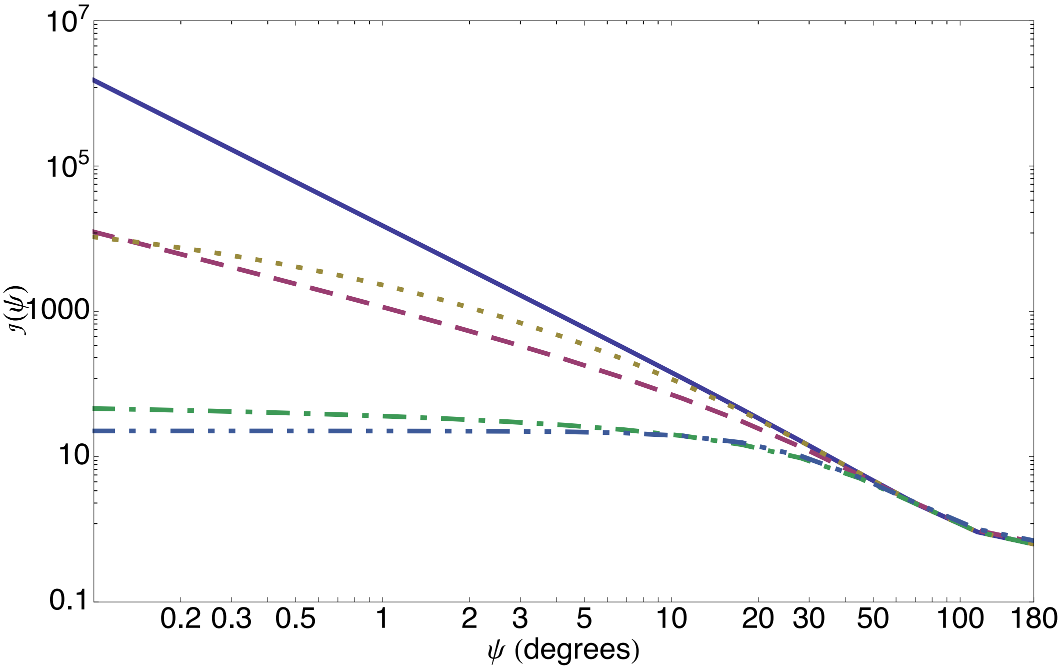

Figure 1.3: The DM density parameter $\mathcal{J}(\psi)$ of the Milky Way, showing the Moore (solid), NFW (dashed), Einasto (dotted), Kravtsov (dot-dashed) and Isothermal (dot-dot-dashed) profiles described in the main text.

to make $\mathcal{J}(\psi)$ dimensionless. The upper limit of the integration is given by

$$l_{max} = \sqrt{(R_{MW}^2 - \sin^2\psi R_{sc}^2)} + R_{sc}\cos\psi, \tag{1.8}$$

where R_{MW} is the radius of the dark matter halo. The density drops away at large radii, so the integral is not sensitive to changes in R_{MW} above 20-30 kpc. We show $\mathcal{J}(\psi)$ for the Milky Way, for the five density profiles listed earlier, in Fig. 1.3. We can also calculate $\mathcal{J}$ for an external galaxy at some distance D from Earth,

$$\mathcal{J}'(\psi) = \mathrm{J}_0 \int_{\ell_{max}}^{\ell_{max}} \rho^2 \left(\sqrt{D^2 - 2\ell D\cos\psi + \ell^2}\right) d\ell\,. \tag{1.9}$$

This is not sensitive to the value of the upper and lower limits of integration as long as they cover most of the galaxy in question. We then define

$$\mathcal{J}_{\Delta\Omega} = \frac{2\pi}{\Delta\Omega}\int_0^{\psi} \mathcal{J}(\psi)\sin\psi\, d\psi, \tag{1.10}$$

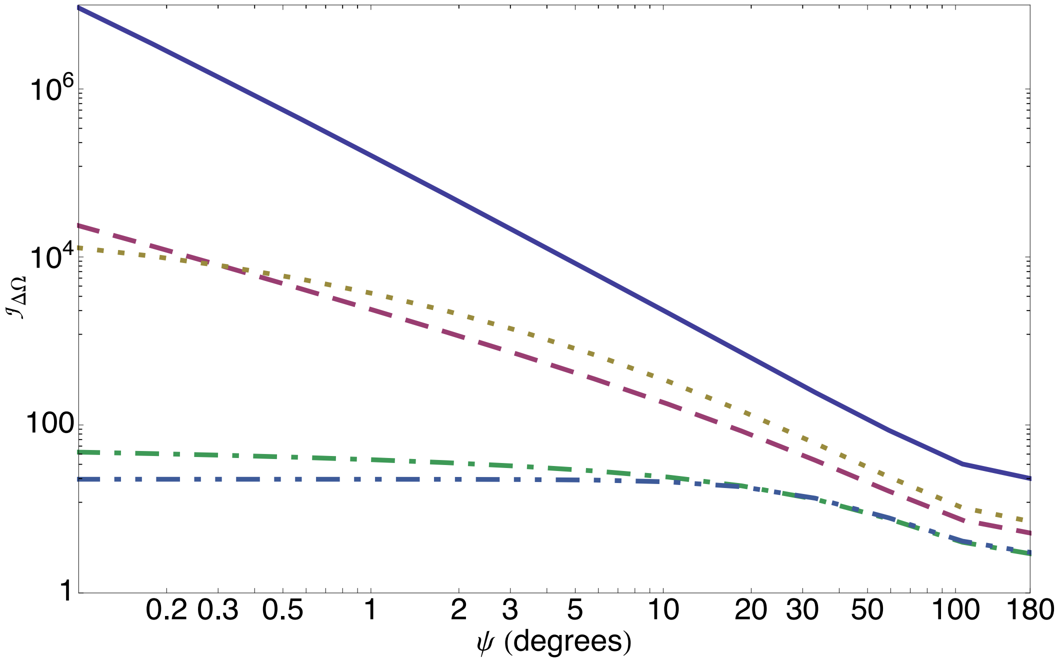

Figure 1.4: The DM density parameter $\mathcal{J}_{\Delta\Omega}$ for the Milky Way, averaged over a cone of solid angle $\Delta\Omega$, as a function of the half-angle ψ of the cone. We show the Moore (solid), NFW (dashed), Einasto (dotted), Kravtsov (dot-dashed) and Isothermal (dot-dot-dashed) profiles described in the main text.

the average of $\mathcal{J}(\psi)$ over a conical observation region of solid angle $\Delta\Omega$, centered on the galactic center. This is shown in Fig. 1.4, again for the five listed density profiles, for the Milky Way.

1.2 Dark Matter Candidates

1.2.1 Neutralino and Gravitino

Supersymmetry (SUSY) is a well-motivated extension of the standard model with a number of attractive features, including a solution to the hierarchy problem, and the unification of gauge couplings. For reviews, see for example, Refs. [20, 42, 43, 44, 45, 46, 47, 48, 49, 50]. Within some SUSY models, several natural DM candidates arise, including possibly the most popular DM candidate, the neutralino. SUSY postulates that each standard model fermion has a bosonic superpartner, and each boson has a fermionic superpartner. SUSY also features an extended Higgs sector, with at least two Higgs doublets. Supersymmetry must by necessity be broken, otherwise we would observe SUSY particles with the same mass as their standard model partners. Many SUSY models feature conservation of R-parity, a multiplicative quantum number defined as $R = (-1)^{3B+L+2s}$ where B is baryon number, L is lepton number and s is spin. Since SM particles have $R = 1$ while SUSY particles have $R = -1$, the lightest supersymmetric particle (LSP) must be stable and can only annihilate into SM particles, and is hence a good DM candidate.

The hierarchy problem is one of the key outstanding issues with the SM. Radiative corrections to the Higgs mass at the one-loop level are proportional to Λ^2, where Λ is the ultra-violet cutoff, the scale at which new physics arises. If this is taken to be near the Planck scale, then these radiative corrections imply a Higgs mass incompatible with constraints suggesting a Higgs mass at the electroweak symmetry breaking scale. Contributions to the radiative corrections from bosons and fermions have opposite signs, such that the divergence terms caused by SM particles and their superpartners will cancel, solving the hierarchy problem.

Supersymmetry also unifies the gauge coupling strengths at the Grand Unified Theory (GUT) scale. Measurements by LEP suggest that without some extension of the standard model, the $SU(3)_C \times SU(2)_L \times U(1)_Y$ couplings do not converge at any energy scale [51]; with the addition of SUSY at the TeV scale, they unify at an energy of around 10^{16} GeV [51]. Such unification of the gauge couplings is a key requirement for the existence of some GUT.

The Minimal Supersymmetric Standard Model (MSSM) (see e.g. Ref. [50]) is a SUSY scenario with the minimal field content required to reproduce the SM. The MSSM pairs each SM particle with a superpartner, and adds a Higgs doublet. Despite its name, the MSSM still has over 100 free parameters. This can be greatly reduced through some well motivated constraints on the soft SUSY breaking parameters, leading to the Constrained MSSM (CMSSM; see e.g. Refs. [52, 49]). In the CMSSM, all scalar quark and lepton masses are constrained to be universal at the cut-off scale, as are the gaugino masses and trilinear couplings. This leaves just four free parameters and one free sign,

$$m_0, \qquad m_{\frac{1}{2}}, \qquad A_0, \qquad \tan\beta, \qquad \mathrm{sign}(\mu), \tag{1.11}$$

where m_0 is the scalar quark and lepton mass, $m_{\frac{1}{2}}$ is the gaugino mass, A_0 is the trilinear soft SUSY breaking term, $\tan\beta$ is the ratio of Higgs field vacuum expectation values, and μ is the superpotential Higgs mass term, which has a fixed magnitude, but is free to be either positive or negative. The CMSSM is often used as a benchmark model, primarily because the reduced parameter space makes constraints on the model feasible. The CMSSM and mSUGRA (minimal SUper GRAvity; see Ref. [53] and references therein) share the same parameters, but mSUGRA breaks SUSY through gravity mediation.

In the MSSM, the Neutralino $\tilde{\chi}^0_1$ is a linear combination of the superpartners of the W_3 and B gauge bosons and the neutral Higgs bosons,

$$\chi = Z_{11}\tilde{W}_3 + Z_{12}\tilde{B} + Z_{13}\tilde{H}_u + Z_{14}\tilde{H}_d, \tag{1.12}$$

and is a spin-$\frac{1}{2}$ Majorana fermion with weak interactions only. Where it appears as the LSP, it can be an attractive DM candidate. In some regions of the parameter space, the neutralino mass is of the order of the weak scale, leading to hope that it may be produced at the LHC [46].

SUSY theories which include gravity also include the superpartner of the graviton, known as the gravitino $\tilde{G}$, another promising DM candidate. Its interaction strength is so weak that it is sometimes labelled a EWIP, or Extremely Weakly Interacting Particle. The mass of the gravitino is only poorly constrained, and can range from eV up to TeV [44].

The CMSSM parameter space has been divided into four allowed regions. Outside of these regions, neutralinos would be overproduced in the early universe, violating WMAP constraints. (i) The *co-annihilation region* is so-called because in this region, the neutralino and stau are near degenerate in mass, and thus underwent co-annihilation in the early universe. This brought the neutralino relic density down to the observed level. (ii) At low values of m_0 and $m_{\frac{1}{2}}$ is the *bulk region* where many supersymmetric particles are relatively light. (iii) In the *A-funnel region*, neutralinos have a large annihilation cross section to $b\bar{b}$ in the s-channel via the A and H resonances. (iv) In the *focus-point region*, the neutralino can have larger masses, and a large higgsino component.

There are other constraints on these parameters, including constraints from BaBar, Belle, the LHC, Tevatron and LEP colliders, (see Section 1.4.2), the requirement that the LSP be electrically neutral, and from direct detection experiments. In particular, the A-funnel, focus point and bulk regions are currently being explored by direct detection experiments, and will be tightly constrained in coming years [54].

1.2.2 Kaluza-Klein Particles

It is plausible that there are hidden extra dimensions in addition to the three spatial and one temporal dimensions we observe. The idea was proposed by Kaluza [55] as a way to unify electromagnetism and Einstein's theory of gravity, and was later developed by Klein [56]. In models with extra dimensions, for each field that propagates in the extra dimensions, called the *bulk*, there will exist a set of states that manifest themselves in the observed $(3 + 1)$ dimensions, called a *brane*, as a 'tower' or stack of particles with definite mass and the same quantum numbers. These are known as Kaluza-Klein particles. In many of these models, standard model particles are confined to the brane. However, models of Universal Extra Dimensions (UED) allow all fields to travel through the bulk [57].

In UED models, the Lightest Kaluza-Klein particle (LKP) can be stable, neutral and colourless, and so is an excellent WIMP candidate. This stability is due to the conservation of *KK-parity*, a consequence of the conservation of momentum in the bulk. Much of the LKP parameter space will be explored at the Large Hadron Collider and next generation direct detection experiments [58, 59] (see also Section 1.4), constraining or hopefully even confirming UED in the near future.

1.2.3 Neutrinos

> *"[Neutrinos have] the undisputed virtue of being known to exist"*
>
> - Lars Bergstrom

Despite their virtuous nature, standard model neutrinos have been ruled out as a leading component of the DM due to their light mass and low abundance. With their extremely small mass and relativistic speeds, neutrinos are an example of hot dark matter, which as we have seen in Section 1.1.6, wipes out small scale perturbations in the early universe, and is incompatible with the formation of large scale structures. Thus WMAP constraints on large scale structure, in combination with data from the SDSS and Hubble telescope, strongly constrains the neutrino abundance. They find $\Omega_\nu < 0.0062$ at the 95% C.L., less than 1/30th of the total DM abundance [18].

There is some evidence for the existence of additional neutrino species that do not interact through the standard model; see e.g. Ref. [60] and refs. therin. These 'sterile' neutrinos are not subject to the abundance constraints mentioned above, and were first proposed as a DM candidate by Ref. [61]. The allowed parameter space is tightly constrained, but sterile neutrinos remain a viable DM candidate [62].

1.2.4 Axions

The axion arrives as a potential solution to a problem in Quantum Chromodynamics (QCD). There is a term in the QCD Lagrangian proportional to a parameter θ, which would lead to charge-parity symmetry violation. A consequence of this is a large electric dipole moment (edm) of the neutron, expected to be of order 10^{-15} e cm. However, measurements show an edm of order 10^{-25} e cm, constraining θ to be remarkably small, $|\theta| \leq 10^{-10}$.

A potential solution to this problem was found through the Peccei-Quinn Mechanism [63], which promotes θ to a field, adds a spontaneously broken symmetry to the standard model, and leads to a vanishingly small value for θ. This introduces a new light pseudoscalar particle, the axion [64, 65]. For a review of the axion, see e.g. Refs. [66, 67].

The axion is limited to a very small mass, $m_A < 10$ meV [66], but its extremely weak interactions mean it may not have been in thermal equilibrium in the early universe, making limits on the relic abundance, analogous to those mentioned above for the neutrino, uncertain. Although the axion is extremely difficult to detect, experimental efforts are underway [68].

1.3 Indirect Detection of Dark Matter

Indirect detection efforts aim to detect dark matter via the observable flux of standard model particles produced in DM self-annihilation or decay both within the Galaxy and throughout the wider Universe. The DM lifetime has been constrained, for example in a model-independent way as described in Section 1.3.2, in a stringent way for a variety of possible final states [69], and from CMB observations which generally require the DM lifetime to be longer than the current age of the Universe [70]. However, we focus here on the annihilation signal.

This annihilation or disappearance rate is governed by the thermally averaged self annihilation cross section, $\langle v\sigma\rangle$ (see Section 1.1.5 for explanation of the thermal average), and the dark matter density, ρ. If DM is a Majorana particle and thus its own antiparticle, or if there is an equal abundance of dark matter and dark antimatter, then the disappearance rate per unit volume is

$$\frac{dn}{dV\,dt} = \frac{1}{2}\frac{\langle v\sigma\rangle \rho^2}{m_\chi^2}, \tag{1.13}$$

where the factor of 1/2 only appears if DM is a Majorana particle.

If DM is the lightest stable beyond-standard-model particle, it will annihilate exclusively to SM particles. In principle, this will lead to an observable flux of SM particles at Earth. This flux will depend on the model-dependent spectrum of SM particles produced per annihilation event. In addition, each species of annihilation product will undergo different interactions with the interstellar medium. Expressions for the flux of gamma rays due to nearby and cosmic annihilations are derived in Sections 2.2.1 and 2.2.2 respectively. Expressions for the flux of electrons/positrons, (anti)protons, and (anti)neutrinos are given in Section 6.5.

Indirect detection techniques can be used to constrain the DM self-annihilation cross section. The observed flux acts as an upper limit on the signal from DM annihilation, and this can be converted into an upper limit on the annihilation cross section, as done in Chapters 2, 3 and 6. It is hoped that indirect detection will one day detect DM through its annihilation signature, manifest as an excess in the observed flux of standard model particles. To qualify as a candidate DM signal, such an excess should have no clear astrophysical explanation, but should be able to be reproduced by annihilation in a specific DM model. Several excesses have been observed, although many are most likely astrophysical in origin, and it is very difficult to conclusively prove that an excess is caused by DM annihilation.

In this section we describe some model-independent constraints on the DM self-annihilation cross section, derived through indirect detection and other techniques. We then introduce two experiments that are important to present-day indirect detection efforts. We also describe a number of excesses that have been proposed as a candidate signal from DM annihilation.

1.3.1 Unitarity

Ref. [71] derives a model-independent constraint on the annihilation cross section based on unitarity considerations. In the low-velocity limit applicable today, this is given by

$$
\begin{aligned}
&\langle v\sigma\rangle \leq \frac{4\pi}{m_\chi^2 v}, \\
\text{or} \qquad &\langle v\sigma\rangle \leq 1.5\times 10^{-13}\mathrm{cm}^3\mathrm{s}^{-1}\left(\frac{\mathrm{GeV}}{m_\chi}\right)^2\left(\frac{300\mathrm{kms}^{-1}}{v}\right).
\end{aligned}
\tag{1.14}
$$

This assumes only unitarity of the scattering matrix $S^\dagger S = 1$, and conservation of energy and momentum, making this a powerful general upper bound on the cross section. This bound is useful as a benchmark with which to compare constraints derived through indirect detection techniques, although it is weaker than the neutrino bounds described below across most of the overlapping mass range. This limit only applies to the $\ell = 0$ contribution to the partial-wave expansion of the cross section, where ℓ is the angular momentum quantum number. In the small velocity limit, the $\ell > 0$ contributions will generally be negligible, but this is not universally true. For example, the $\ell > 0$ contribution may not be negligible if the DM is subject to long range interactions [71]; see also Refs. [71, 72, 73] for other unusual circumstances where this limit can be evaded. In these cases, limits based on unitarity arguments are not avoided altogether, but may be weakened. This limit rules out the thermal relic cross section $\langle v\sigma\rangle \sim 3\times 10^{-26}\mathrm{cm}^3\mathrm{s}^{-1}$ for masses above $\sim$ 1000 TeV. Ref. [72] performs a similar calculation for DM in the early universe.

1.3.2 Neutrino Limits

If we make the reasonable assumption that DM decay or annihilation products must be Standard Model particles (i.e. we assume the dark matter is the lightest stable particle in the beyond-Standard-Model sector) then it is possible to set a conservative upper bound on the *total* DM annihilation rate by looking for the annihilation products which are the hardest to detect, namely, neutrinos [74]. By assuming the branching ratio to neutrinos is 100%, the bound on annihilation to neutrinos becomes a bound on the total annihilation rate. In reality the branching ratio will be less than 100%. However, all other final states will inevitably produce gamma rays, which lead to more stringent limits on the total cross section than are obtained with neutrinos, as shown in Chapter 2. For example, quarks and gluons hadronize, producing pions and thus photons via $\pi^0 \rightarrow \gamma\gamma$; the decays of $\tau^\pm$, $W^\pm$, and Z^0 also produce π^0. Charged particles produce photons via electromagnetic radiative corrections as described in Section 1.5, while energy loss processes for $e^\pm$ such as inverse Compton scattering off the interstellar radiation field, or synchrotron radiation due to the turbulent interstellar magnetic field, also produce photons [75, 76, 77]. Thus by assuming a branching ratio to neutrinos of 100%, one obtains the most conservative and robust upper limits on the total annihilation cross section.

A number of groups have used this technique to constrain the DM annihilation or decay rate. Ref. [74] calculate the cosmic diffuse neutrino flux, produced through DM annihilation to a neutrino-antineutrino pair, considering DM annihilation in all halos throughout the Universe. They compare this with the known diffuse neutrino background to derive robust constraints on the total cross section over a large DM mass range, from 100 MeV up to 100 TeV. This technique was applied to annihilation within our own galaxy by Ref. [2], and used to derive a comparable, and in some cases stronger, limit than that obtained from cosmic annihilations only. Ref. [78] also considered annihilation to neutrinos within our own galaxy, deriving bounds on MeV scale DM, while Ref. [79] included substructure enhancement. These techniques have also been used by Ref. [80] to place bounds on the DM lifetime. Ref. [81] considered how DM decay to neutrinos would affect the cosmic expansion rate, and uses this to place somewhat weaker limits on the decay rate to neutrinos. Since these limits are extremely conservative, they form a good baseline with which to compare subsequent limits on DM annihilation or decay. See Chapter 2 for a comparison between limits from [74], and limits on annihilation to a gamma-ray pair; see Chapter 3 for comparison of these limits with limits on annihilation to charged lepton pairs.

These limits are indeed overly conservative, since DM can never annihilate to a pure neutrino final state. Even in an unrealistic model with annihilation to neutrinos only, Chapter 4 shows that electroweak radiative corrections (emission of a W or Z) will always lead to non-neutrino final states. Depending on the branching ratio for this process, limits based on the non-neutrino annihilation products may be weaker than, comparable to, or stronger than limits from neutrinos [82, 83, 84, 85]. The model proposed by Ref. [86] is an example of a model intended to have a large branching ratio to neutrinos-only final states. In Chapters 5 and 6 we show that Electroweak Radiative corrections play a large role, leading to branching ratios to neutrinos orders of magnitude below 100%.

1.3.3 PAMELA

The PAMELA (Payload for Antimatter Matter Exploration and Light-nuclei Astrophysics) satellite was launched in 2006, with the goal of studying cosmic rays with energies between 100 MeV and several hundred GeV, in particular positrons and antiprotons [87]. PAMELA consists of a number of components including a magnetic spectrometer, time of flight indicator, and electromagnetic calorimeter. The magnetic spectrometer measures the sign of the charge, momentum divided by charge, and path length of the cosmic rays. The path length is combined with data from the time of flight to measure the velocity of incident particles. The electromagnetic calorimeter is used to determine the energy of the electrons and positrons, and to distinguish between electrons/positrons and protons/antiprotons.

In 2008, the PAMELA collaboration released results showing a large excess in the ratio of positrons to electrons, above the astrophysical expectation from standard cosmic ray production and propagation models, without an accompanying excess in the flux of antiprotons. This has widely been interpreted as a potential signal from DM annihilation. This is discussed in detail in the broader context of all available cosmic ray data in Section 1.3.6.

1.3.4 Fermi

The Fermi satellite, formerly known as GLAST [88], was launched in 2008 with the primary purpose of studying high-energy gamma rays. The main instrument is the LAT (Large Area Telescope) [89]. Gamma rays interact with tungsten sheets within the LAT, producing an electron-positron pair, which are tracked to determine the origin of the gamma-ray before entering the calorimeter which determines the gamma-ray energy. An anti-coincidence detector rejects cosmic rays. The LAT has a wide field of view of 2.4 steradians (whole sky $= 4\pi$ sr), and observes gamma rays with energies between 20 MeV and 300 GeV.

Fermi data has been used in a wide range of indirect detection efforts, thanks to the improved energy range, resolution and sensitivity of the LAT compared with older telescopes. For example, a number of DM annihilation channels have recently been constrained using flux limits from nearby dwarf spheroidal galaxies [90, 91, 92, 93]. These are a promising source for indirect detection studies, as they have low gamma-ray backgrounds and a large signal-to-noise ratio due to their small luminous matter component and large ratio of DM to luminous matter In particular, Fermi sets new bounds on the isotropic extragalactic gamma-ray background [94], one of the candidates most likely to have an observable component due to DM annihilation [95]. We make use of this flux data in Section 6.5.1. See also Section 2.4 for a discussion of Fermi limits on the annihilation rate to a gamma-ray pair.

The design of the LAT allows measurement of the flux of electrons and positrons, although this was not its primary purpose. The observed flux exceeds the expected flux from conventional astrophysical processes, and it has been proposed that this excess is due to DM annihilation. This is discussed in detail in Section 1.3.6, and the flux data is used in Section 6.5.2.

1.3.5 Photon Excesses

WMAP Haze

The Wilkinson Microwave Anisotropy Probe (WMAP) [96] shows an apparent excess in the microwave spectrum, extending about 10 degrees and focused on the Galactic center. This has come to be known as the "WMAP haze", and is interpreted as synchrotron emission from a hard electron population of unknown origin [97].

The morphology and spectrum of the haze has been shown to be consistent with the signal expected from certain DM models e.g. [98, 99, 77], and several models are found to be a consistent explanation for both the haze and the positron excess described in Section 1.3.6 e.g. [100].

There are a number of alternative explanations for the excess. For example, the energetic electrons may have been accelerated by a supernova shock [101], or may have been produced by pulsars [102]. Alternatively, using alternative foreground subtraction techniques, it has been claimed that the excess is insignificant within statistical uncertainties [103, 104].

Ref. [105] finds a Fermi gamma-ray counterpart to the WMAP Haze, which again may be consistent with a signal from DM annihilation [106].

511keV Line

The INTEGRAL satellite observes a prominent gamma-ray line at 511 keV [107, 108, 109, 110], evidently produced by the annihilation of electrons and positrons at rest. The morphology consists of a bulge with a 2-dimensional Gaussian shape, focused on the Galactic center. There is no consensus on the source of the positrons required to produce this line, and it is difficult to explain with standard astrophysical sources e.g. [111, 112, 113, 114, 115, 116, 117] and references therin.

DM offers an appealing explanation for this excess, however this possibility is tightly constrained. If the injected positron energy is greater than ~ 20 MeV, photon bremsstrahlung emission (see Section 1.5) would violate observational constraints on gamma-ray emission [111]. If gamma rays from inflight annihilation are also taken into account, the maximum injection energy is reduced to ~ 3 MeV [112]. For models that can explain the excess, see e.g. Ref. [117] and references therin.

Egret excess

As a cautionary tale, it is interesting to note that the EGRET space telescope reported an excess in the diffuse gamma-ray flux between 1 GeV and 10 GeV, above the flux expected from standard astrophysical production mechanisms. At the time, this was interpreted by many as a potential signal from DM annihilation; see e.g. [118]. However, recent data from the Large Area Telescope (LAT) aboard the Fermi satellite shows no such excess [94]. This discrepancy could be due to systematic errors in the determination of the EGRET detector's effective area at high energies [119].

1.3.6 Positron Excess

Until recently, it was believed that the main source of cosmic ray positrons was secondary production, where these particles are produced via the interaction of cosmic ray protons with the interstellar gas. The standard scenario predicts a falling combined flux of electrons plus positrons, and also a falling ratio of positrons to electrons plus positrons, e.g. [120].

There is now clear evidence for an excess in the observed flux of electrons and positrons above that expected from conventional production models. The balloon-borne ATIC (Advanced Thin Ionization Calorimeter) experiment has made several flights over Antarctica, and reports a clear excess in the $e^+ + e^-$ flux in the energy range ~ 300 to 800 GeV [121], while another balloon-borne Antarctic experiment, PPB-BETS, supports this to an extent with a more marginal excess [122]. The H.E.S.S (High Energy Stereoscopic System) array, described in Section 2.3.2, shows a significant steepening in the $e^+ + e^-$ flux above ~ 1 TeV [123, 124], while high-precision data from the Fermi satellite, described in Section 1.3.4, shows an excess between ~ 20 GeV and 1 TeV [125]. Finally, PAMELA, described in Section 1.3.3, reports a clear and dramatic excess in the positron fraction in the 1.5 GeV to 100 GeV energy range [126]. Although these individual data sets are in tension and there is no agreement on the spectral shape or magnitude of the excess, together these experiments build a clear picture of some form of excess above 100 GeV. However, PAMELA reports no anomalies in the fraction of antiprotons to protons [127], a critical consideration when examining the origins of the excess. Identifying a source is complicated by the fact that electrons and positrons will undergo energy loss and diffusion as they propagate from source to detector, such that observed electrons and positrons in this energy range provide no useful directional information, and the source energy spectrum will be different to the observed spectrum. In particular, high energy electrons and positrons will undergo severe energy loss, primarily due to synchrotron emission and inverse Compton scattering. Any source of high energy $e^\pm$ must be within ~ 1 kpc, or the particles must reach us within $\sim 10^5$ years, in order to be observed before losing most of their energy [128]. See Section 6.5.2 for a full description of electron and positron energy loss and diffusion.

There are a number of potential explanations for this excess. Supernova remnants (SNRs) constitute one of the main sources of primary electrons, whilst producing few primary positrons; see e.g. [128, 129]. It has been proposed that a modification of the conventional scenario could lead to a positron fraction consistent with data [130, 131]. For example, if the assumption of a homogeneous distribution of SNRs is relaxed for SNRs within a few kpc, then a lack of nearby high-energy sources can cause the primary electron flux to fall to a level consistent with the PAMELA positron fraction, while the $e^+ + e^-$ excess could be explained by nearby lower-energy sources [130].

Alternatively, the excess could be due to nearby pulsars. Although pulsars are a well-known source of electrons and positrons, the theory governing the production mechanisms within pulsars is not well understood. There are a number of production models with varying predictions (e.g. [132, 133, 134, 135]), and there are large uncertainties in the parameters within these models. However, by fitting the theoretical $e^{\pm}$ flux due to pulsars with the observational data, one can find models and regions of the parameter space where the excess is consistent with production by one or more nearby pulsars, such as Geminga or Vela [136, 137, 138, 135, 139, 140, 141, 142].

Another proposal is that the excess is caused by the acceleration of lower-energy secondary $e^{\pm}$ in conventional cosmic ray sources such as SNRs. Standard models of cosmic ray production only include acceleration of the primary particles produced by the source [128]. If the secondary $e^{\pm}$ are being produced through hadronic interactions within the source, then they will also undergo acceleration, and this can lead to the observed excess [143, 144, 145, 146].

It is also possible that the standard propagation prescription is in error. Refs. [147, 148, 149] describe models of cosmic ray propagation through the Galaxy that can reproduce the observational data without invoking a new source of positrons or electrons.

DM Interpretation

As an alternative to these astrophysical mechanisms, it has also been proposed that the excess e^{+} and e^{-} are produced via dark matter annihilation in the Galactic halo, and a large number of DM models have been proposed with this goal in mind.

Many popular models feature suppressed annihilation to leptons, and are thus unable to reproduce the positron excess without violating constraints on the antiproton fraction. For example, for large regions of the parameter space, annihilation of supersymmetric DM would overproduce antiprotons through the production and decay of massive gauge bosons, and subsequent hadronization of the decay products. Emission of a gamma-ray from one of the final state particles can lift this suppression (see Section 1.5 such that models with suppressed annihilation channels may still be a viable explanation. However, electromagnetic radiative corrections, i.e. emission of a massive gauge boson, must also be taken into account and can drastically alter the phenomenology of a model. Chapter 4 introduces electroweak radiative corrections; Chapter 5 applies this to suppressed models, and discusses suppression in detail; Chapter 6 discusses implications for indirect detection.

This has led to the proposal of a large number of 'leptophilic' models, where DM annihilates predominantly into leptons, such as the model of Arakani-Hamed et al. [150] who propose that the DM annihilates into a new force carrier with light mass, which subsequently decays dominantly into leptons. For an overview of some other models proposed to explain the excess, see e.g. Refs. [151, 152, 153]. Even when annihilation is not suppressed, these models generally need an annihilation rate larger than the $\langle v\sigma\rangle \sim 3 \times 10^{-26}$ cm^3 s^{-1} expected for thermal relic DM in order to reproduce the excess. For most annihilation channels and DM masses, boost factors of order 10^2 to 10^4 are required [154]. Clumpiness of DM due to substructure within halos can enhance the annihilation rate. However, in conventional scenarios, the boost factor is only of order 10 [155]. The so-called Sommerfeld enhancement [156] of the annihilation rate has received much attention. This is an enhancement of the annihilation cross section for non-relativistic particles in the presence of a long-range potential. If there is a new force in the dark sector, the Sommerfeld effect can greatly enhance the annihilation rate at low DM velocities [157, 158, 159, 160, 150, 161]. The enhancement factor is tightly constrained by direct detection results and thermal freezeout calculations, and may not be sufficient to explain the excess, although there may be ways around this [162, 163, 164, 165, 166].

As mentioned in Section 1.1.5, DM may not have been thermally produced, in which case the annihilation cross section is not required to be the thermal relic rate of $\langle v\sigma\rangle \sim 3 \times 10^{-26}$ cm^3 s^{-1}, and no boost factor is necessary.

1.4 Other Searches for Dark Matter

1.4.1 Direct Detection

WIMP dark matter is expected to scatter off ordinary matter, even if the interaction rate is tiny. Direct detection experiments aim to observe these rare events by measuring the recoil energy E_r transferred to the nucleon.

The differential interaction rate dR/dE_r depends on the differential scattering cross section $d\sigma/d|\vec{q}|^2$, the local dark matter density ρ_0 and mass m_χ, and the local dark matter velocity distribution $f(v)$, normalised to $\int f(v)dv = 1$. The rate can be expressed as

$$\frac{dR}{dE_r} = \int_{v_{\text{min}}}^{\infty} \frac{d\sigma}{d|\vec{q}|^2} \frac{2\rho_0}{m_\chi} v f(v) dv, \tag{1.15}$$

where v_{min} is the minimum WIMP speed needed to transfer a recoil energy E_r. Note that $f(v)$ varies with time, to take into account the motion of the Earth around the Sun. It is useful to rewrite the scattering cross section as

$$\frac{d\sigma}{d|\vec{q}|^2} = \frac{\sigma_{\chi-N}}{4m_r^2 v^2} \mathrm{F}(E_r)^2, \tag{1.16}$$

where $m_r = (m_\chi m_N)/(m_\chi + m_N)$, and expressions for the form factor $\mathrm{F}(E_r)$ can be found in e.g. Ref. [43]. This isolates terms in the cross section that depend on the variables v, E_r, m_χ, m_N, and allows constraints to be placed on the WIMP-Nucleus cross section parameter $\sigma_{\chi-N}$, which is the total cross section for a transfer of zero momentum.

There are two contributions to the scattering cross section. Spin dependent scattering occurs when the DM interacts with the target through an axial-vector coupling. In this case scattering strength depends on the spin of the target. Conversely, scalar or vector couplings lead to spin independent scattering. This type of interaction is more sensitive to the number of nucleons in the target, and generally provides a larger signal in modern heavy-atom experiments. The scattering process can be either elastic or inelastic. Elastic scattering is the standard interaction where

DM scatters off a nucleus, transferring some recoil energy. Inelastic scattering occurs when the DM either ionizes the target, or leaves the nucleus or orbital electrons in an excited state. This process leads to emission of a photon shortly after the interaction.

The event rate is expected to be low, less than one event per day per kilogram of detector material, so minimizing and discriminating the background is essential. Detectors are located deep underground to avoid cosmic rays, and shielding is used to avoid background radiation from the environment, although some background from cosmic ray muons and background radiation is inevitable. Signal can be distinguished from background by searching for an annual modulation in the signal due to the Earth's motion around the Sun [167], a directional anisotropy in the signal due to the Earth's motion relative to the Galactic rest frame [167, 168, 169, 170], or by using a detector with complementary detection techniques. For example, the XENON100 experiment measures both the scintillation signal and the ionization of the target when an event takes place. Background events and DM events can be distinguished from the relative strength of these two signals [171].

The DAMA/LIBRA collaboration reports an annual modulation in the observed signal, and claim this as detection of dark matter [172, 173]. This appears to be in tension with the strongest constraints on the scattering cross section, from CDMS-II [174] and XENON100 [175], which report null results, and place upper limits on the WIMP-nucleon cross section. Both the detection and null results may be consistent in certain models or if certain effects such as channeling are taken into account; e.g. [176, 177, 178]. The CoGeNT collaboration reports the hint of a signal consistent with scattering of light dark matter ($m_\chi \sim 5$ to 10 GeV). Intriguingly, this is also consistent with the modulation seen by DAMA/LIBRA [176], but there is not yet sufficient data to call the CoGeNT result a detection [179]. As CoGeNT and other detectors continue to take data, hopefully a clearer picture will emerge in the near future.

1.4.2 Colliders

When searching for DM production at a collider experiment, the main signature is missing energy, since the DM escapes the collider undetected. As of yet there is no evidence for the production of DM at a collider. However, there are many Standard Model (SM) processes that could be affected by the existence of beyond-SM physics. For example, precision measurements of the branching fraction $b \to s\gamma$ by BaBar, CLEO and Belle would be affected by a number of potential beyond-SM processes, and the LEP collider has placed strong constraints on properties of beyond-SM charged particles [180], while the Tevatron, as a $p - \bar{p}$ collider, efficiently constrains properties of beyond-SM colored particles [181, 182]. Together these and other measurements place strong constraints on parameters in SUSY and other models e.g. [183, 184, 185], however these constraints are highly model-dependent, and do not constrain a generic DM particle.

The LHC is currently probing the largest center of mass energy ever reached by a collider, and is already strengthening the constraints on models such as SUSY [186, 187, 188, 189]. The reach of the LHC should be great enough to either find evidence for a beyond-SM theory like SUSY or extra dimensions, or to rule out large regions of the parameter space [183, 184, 185]. In the longer term, the proposed International Linear Collider (ILC) working in combination with the LHC has excellent prospects for the detection and identification of beyond-SM physics [190].

1.5 Bremsstrahlung Processes

Dark matter annihilation to charged particles will always be accompanied by a form of radiative correction called *photon bremsstrahlung* where a gamma-ray is emitted from one of the final state particles at the Feynman diagram level [111, 191, 192, 193, 194], as shown in Figure 1.5. In some models, emission from the propagator is also possible. For emission from the final state particles, the gamma-ray spectrum generally does not depend on the unknown interactions of the DM particle, such that

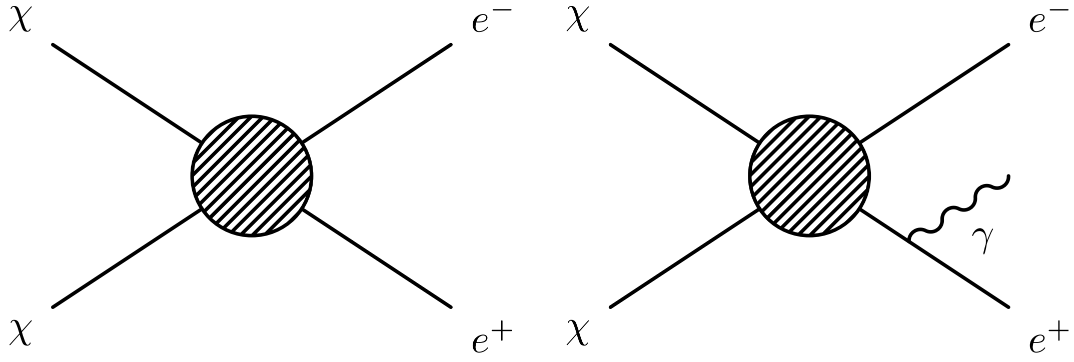

Figure 1.5: The lowest order tree level process $\chi\chi \rightarrow e^+e^-$ (left) is accompanied by photon bremsstrahlung processes (right).

a single gamma-ray spectrum per annihilation to an electron-positron pair is valid across a broad range of models (see Chapter 3 for a full discussion).

This is an important channel to consider, especially in models designed to produce electrons and positrons without overproducing other particles. For example, as mentioned in Section 1.3.5, Ref. [111] found that the cross section to an electron-positron pair required to explain the 511 keV line would generally lead to an overproduction of photons, violating observational constraints on the gamma-ray flux. As mentioned in Section 1.3.6, leptophilic models with large annihilation rates have been proposed as an explanation for the observed positron excess. In light of this, constraints on the annihilation rate to an electron-positron pair are particularly interesting. We calculate such constraints in Chapter 3 using the gamma-ray signal from photon bremsstrahlung.

However, this is only one class of radiative correction. Dark matter annihilation to leptons will also inevitably be accompanied by *electroweak bremsstrahlung* processes where massive $W^{\pm}$ and Z gauge bosons are radiated in place of photons. This channel clearly has important phenomenological consequences, as the decay of the W/Z's will lead to production of photons, hadrons and leptons, regardless of the direct couplings of the DM particle. Even if the dark matter annihilates only into neutrinos at the $2 \rightarrow 2$ level, hadrons and gamma rays are impossible to avoid. In

Chapter 4 we consider such a model, and calculate the ratio of the annihilation rate to electroweak bremsstrahlung final states to the 2 → 2 rate.

Electroweak radiative corrections in the context of DM annihilation or decay have been studied by a number of groups. Ref. [195] calculates the branching ratio for the $Z\nu\bar{\nu}$ final state relative to the $\nu\bar{\nu}$ final state for superheavy DM, and studies the consequences of the subsequent EW cascade. Ref. [82] presents the same ratio for a handful of (smaller) DM masses without assuming superheavy DM, and uses the resulting gamma-rays from Z decay to constrain the annihilation cross section. Ref. [83] updates this work and finds results in agreement with our results presented in Chapter 4. Ref. [83] also constrains the DM annihilation cross section in this model by examining the multi-messenger annihilation signal of both primary annihilation products and secondary $W^{\pm}/Z$ decay products, including an analysis of the proton and antiproton fluxes. Ref. [196] performs a similar calculation of the electroweak bremsstrahlung branching ratio at a higher DM mass scale. Ref. [85] shows that such a neutrinos-only model will inevitably produce primary charged particles via higher-order tree and loop diagrams. Ref. [197] calculates approximately model-independent spectra of stable particles (e^{+}, p, ν and their antiparticles, plus γ) due to EW radiative corrections in DM annihilation or decay. The work in Ref. [198] is complementary to our work, confirming some of the results presented in Chapter 5, and showing the effect of diffusion on the resulting fluxes of W/Z decay products as would be observed at Earth.

In certain cases, photon bremsstrahlung plays an especially important role. Many dark matter models suffer from a heavy *helicity suppression* of the annihilation rate into light fermions. It has long been known that in certain models, photon bremsstrahlung can lift this suppression such that the 2 → 3 annihilation rate to the photon bremsstrahlung final state is much larger than the 2 → 2 annihilation rate [192, 193, 194, 199, 200, 201]. In Chapter 5 we link this idea with electroweak bremsstrahlung, and show that massive gauge bosons can play the same role as photons in lifting helicity suppression.

Electroweak bremsstrahlung is especially important in the context of leptophilic models designed to explain the positron excess since annihilation to antiprotons is severely restricted by the lack of an observed antiproton excess. It is vital to consider all possible avenues of hadron production in these leptophilic models, since even a small branching ratio to hadronic final states has the potential to overproduce antiprotons and rule out an otherwise feasible model as an explanation of the excess. In Chapter 6, this is explored in the context of a typical leptophilic model where helicity suppression can be lifted by electroweak bremsstrahlung.

2

Constraints on Dark Matter Annihilation into Gamma Rays

2.1 Introduction

Here we calculate the constraints that can be placed on the dark matter self annihilation cross section using gamma rays, the most detectable final states, over a wide range of dark matter masses. We first focus on the $\gamma\gamma$ final state, as it would be a very clean signature of dark matter annihilation, with $E_\gamma = m_\chi$, e.g., Refs. [202, 203, 204, 205, 206, 207, 208]. Unfortunately, this is typically small, $Br(\gamma\gamma) \sim 10^{-4} - 10^{-3}$, although it can be much larger, even larger than 0.1 [209, 210, 211, 212]. Since gamma rays will be ubiquitously produced, directly in SM final states, or through radiative corrections and energy-loss processes, we also consider more general outcomes, in which the gamma-ray energies are in a broader range below m_χ.

We consider constraints on the dark matter annihilation cross section over a large mass range of 10^{-5} – 10^{5} GeV. At all but the highest energies, gamma-ray data is available to test the annihilation cross section, provided that we combine constraints defined using the Milky Way halo, the Andromeda halo, and all the halos in the universe. (Modern data, especially those from observations of the Milky Way and

Andromeda, are significantly more constraining than those that were available earlier.) Using our upper limits on the dark matter annihilation cross section to gamma rays, and a conservative assumption about the branching ratio to monoenergetic gamma rays, we define upper limits on the total cross section and compare to other constraints.

Since the dark matter annihilation rate scales with density squared and the density profiles are uncertain, we are mindful of how our constraints on the cross section are affected by astrophysical uncertainties. We are conservative in our input choices and analysis methods, and we show how our results depend on these. In light of these considerations, we do not consider corrections that would affect the results by less than a factor of ~ 2, which also allows some simplifications. Our upper bounds on the annihilation cross section to gamma rays would only be improved by more optimistic assumptions.

2.2 Calculation of Dark Matter Signals

The dark matter annihilation rate depends on the square of the dark matter number density ρ/m_χ, which is written in terms of the unknown mass m_χ and the uncertain dark matter mass density ρ. Not coincidentally, where the density is largest, at the centers of halos, the uncertainties are the largest; these regions contribute relatively little to the gravitationally-measured mass of a halo. To cover as large of an energy range as possible, we have to consider gamma-ray data for the Milky Way, Andromeda, and all of the dark matter halos in the universe. In all cases, though the astrophysical and analysis uncertainties vary in their severity, we make conservative choices for the dark matter density and hence the cross section limits (smaller choices for the density mean larger upper limits on the cross section).

2.2.1 Milky Way and Andromeda Signals

We first consider the signal from DM annihilation in our own galaxy. The flux of gamma rays per steradian, along the line-of-sight l, is

$$\frac{d\Phi_\gamma}{dE} = \int dl \frac{\langle v\sigma \rangle}{8\pi m_\chi^2} \rho(r(l,\psi))^2 \frac{dN_\gamma}{dE}, \tag{2.1}$$

where l is at an angle ψ to the Galactic center, and $\rho(r)$ is the dark matter density. The dark matter density profile of the galaxy is described in detail in Section 1.1.7. It is useful to divide this into a part that depends only on particle physics, and a part labelled $\mathcal{J}$, introduced in Section 1.1.7, that depends only on astrophysics. This allows us to contain all astrophysical uncertainties in a single parameter, which we recall is defined as

$$\mathcal{J}(\psi) = J_0 \int_0^{l_{\max}} \rho^2 \left(\sqrt{R_{sc}^2 - 2lR_{sc}\cos\psi + l^2} \right) dl, \tag{2.2}$$

where R_{sc}, J_0 and ℓ_{max} are given in Section 1.1.7. With these definitions, the annihilation signal per steradian in the direction ψ is

$$\frac{d\Phi_\gamma^\psi}{dE} = \frac{\langle v\sigma \rangle}{8\pi m_\chi^2} \frac{\mathcal{J}(\psi)}{J_0} \frac{dN}{dE} \tag{2.3}$$

We wish to compare this signal with an observed flux averaged over a viewing region of solid angle $\Delta\Omega$. Making use of $\mathcal{J}_{\Delta\Omega}$ defined in Eqn. 1.10, the annihilation signal per steradian averaged over such a region is

$$\frac{d\Phi_\gamma}{dE} = \frac{\langle v\sigma \rangle}{8\pi m_\chi^2} \frac{\mathcal{J}_{\Delta\Omega}}{J_0} \frac{dN}{dE}. \tag{2.4}$$

We also define the total signal for a region of solid angle $\Delta\Omega$ as

$$\frac{d\phi_\gamma}{dE} = \frac{d\Phi_\gamma}{dE}\Delta\Omega = \frac{\langle v\sigma \rangle}{2} \frac{\mathcal{J}_{\Delta\Omega}\Delta\Omega}{\mathrm{J}_0} \frac{1}{4\pi m_\chi^2} \frac{dN_\gamma}{dE}. \tag{2.5}$$

As can be seen in Figure 1.2, there are considerable uncertainties in the dark matter density profile of the galactic halo, particularly in the central region where the density, and hence the annihilation rate, is largest. Uncertainties in the density of the DM halo translate into uncertainties in the DM annihilation signal. In order to minimize these uncertainties, wherever possible we examine the signal from a large angular region around the Galactic center: While the uncertainties scale several orders of magnitude for small angular scales close to the Galactic Center, they are mild for large angular regions of the galaxy, as shown in Figs. 1.3 and 1.4. In order to place conservative upper limits on the DM annihilation cross section, we focus on a profile with a very conservative dark matter density, namely the Kravtsov profile. For the NFW, Einasto and Moore profiles, smaller values of $\langle v\sigma \rangle$ are needed to reproduce the same flux, and hence lead to stronger (less conservative) limits.

This formulation of the annihilation signal is valid for any source with a spherically symmetric DM density profile, if the source is sufficiently close that attenuation and redshift of the annihilation products are negligible. Thus, we also use Eqn. 2.5 to calculate the signal from the nearby M31 Galaxy, also known as Andromeda. To find $\mathcal{J}_{\Delta\Omega}$, we replace R_{sc} in Eqn. 2.2 with $D_{\rm M31} \simeq 700$ Mpc. There does not appear to be a consensus on the values of the halo parameters for Andromeda; for example, compare the NFW profiles in Ref. [213] with Ref. [214], where both ρ_0 and r_s are quite different. Thus we have chosen to model Andromeda using the Milky Way parameters, as an appropriate compromise between competing extremes. For external galaxies, there is little dependence on $l_{\rm max}$ in Eqn. 2.2, as long as we cover most of the galaxy. For extragalactic dark matter sources, the annihilation signals will include a contribution from the dark matter in our own galaxy along the line of sight. However, in the case of an external galaxy like Andromeda, this contribution will be eliminated if there is a subtraction of the background intensity from a region close to the source, as is often done in observational analyses.

DM annihilation rates may be enhanced due to substructure in the halo, e.g., Refs. [36, 215, 216, 217], or mini-spikes around intermediate-mass black holes [218, 219] This can be included either in a modified $\mathcal{J}_{\Delta\Omega}$, or as a 'boost factor' B in Eqn. 2.4. In typical scenarios, substructure can boost the annihilation signal by a factor of order 10 [155]. Including substructure could only strengthen our results; In order to remain conservative, we do not take substructure into account.

Spectrum per annihilation

For annihilation to a pair of monoenergetic gamma rays, the spectrum per annihilation is $dN/dE_\gamma = 2\delta(m_\chi - E_\gamma)$. In reality, the spectrum would be smeared in the detector, since the energy resolution will never be perfect. However, in all cases where this could be an issue, we have integrated the annihilation signal over an energy bin, wide enough to include the smeared spectrum per annihilation. In other words, our energy bins are sufficiently broad that they are not sensitive to the smearing of the annihilation, since we will always capture the two gamma rays in our integration of the signal spectrum.

Although we nominally assume a monoenergetic annihilation spectrum, much of our analysis is effectively valid for any annihilation spectrum where we capture at least two gamma rays in our energy bin. This is discussed in Section 2.4.

2.2.2 Cosmic Diffuse Signal

The calculation of the cosmic diffuse annihilation signal is detailed, for example, in Refs. [220, 221], where the cosmological flux of annihilation products from external galaxies was calculated taking the clustering of dark matter into account. The cosmic diffuse flux, arising from dark matter annihilation in halos throughout the Universe, is

$$\begin{aligned} \frac{d\Phi_\gamma}{dE} &\equiv \frac{dN_\gamma}{dA\, d\Omega\, dt_0\, dE} \\ &= \frac{c}{4\pi} \int dz \frac{e^{-\tau(z,E)}}{H_0\, h(z)} \int dM \frac{dn}{dM}(M,z) \frac{d\mathcal{N}_\gamma}{dE'}(E(1+z), M, z) \end{aligned} \tag{2.6}$$

where $H_0 = 70$ km s^{-1} Mpc^{-1} is the Hubble parameter, dn/dM describes the distribution of bound halos, and $d\mathcal{N}_\gamma/dE$ is the production rate of gamma rays due to dark matter annihilation in a halo at redshift z and of mass M, which we can safely regard as pointlike. We assume a flat universe, with $\Omega_{DM} = 0.3$, $\Omega_\Lambda = 0.7$, $h(z) = [(1+z)^3\Omega_{DM} + \Omega_\Lambda]^{1/2}$.

The optical depth $\tau(z,E)$ takes into account absorption of gamma rays, primarily through electron-positron pair production as they interact with the extragalactic optical and infrared background. Attenuation is a modest effect in the energy and redshift ranges we consider; For sources at redshift $z \simeq 0.1$, absorption becomes important for observed energies above around 1 TeV. There are a number of detailed studies of this effect, involving calculation of the background low-energy photon density through simulations of galaxy formation and comparison with observational data. See, for example, [222, 223, 224, 225]. We follow [220, 221, 222, 224] and use the parameterisation

$$\tau(z,E) = \frac{z}{z_{\max}}, \qquad z_{\max} \simeq 3.3 \left(\frac{E}{10\,\mathrm{GeV}}\right)^{-0.8}. \tag{2.7}$$

Expressions for $d\mathcal{N}_\gamma/dE$ and dn/dM are presented in [220, 221], and lead to a final expression

$$\begin{aligned} \frac{d\Phi_\gamma}{dE} &= \frac{\langle v\sigma\rangle}{2}\frac{c}{4\pi H_0}\frac{\Omega_{DM}^2\rho_{\mathrm{crit}}^2}{m_\chi^2} \\ &\times \int_0^{z_{up}} \frac{f(z)(1+z)^3}{h(z)}\frac{dN_\gamma(E')}{dE'}e^{-\tau(z,E)}dz\,. \end{aligned} \tag{2.8}$$

The factor $f(z)$ in Eq. (2.8) accounts for the average increase in density squared due to the fact that dark matter is clustered into halos rather than uniformly distributed, and the evolution with redshift of the halo number density. This gives an enhancement of the signal relative to that of a homogeneous distribution. (The Δ^2 factor in [74] is equal to $f(z)(1+z)^3$). Redshift dependence of $f(z)$ is well established and has little dependence on uncertain parameters mentioned below. Following [2], we use the parameterization $\log_{10}(f(z)/f_0) = 0.9\,[\exp(-0.9z) - 1] - 0.16z$. However, there is a great deal of uncertainty in the overall normalization factor f_0, which depends on the halo profile and assumptions on the concentration parameter and substructure formation [2, 95, 221, 23, 226, 227, 228]. We follow [2, 228] and adopt

$f_0 \simeq 2\,(5)\ \times 10^4$ for the Kravtsov (NFW) profile. This is a conservative choice for $f(z)$, and inclusion of enhancements due to subhalos would only strengthen our results. For example, our choice of $f(z)$ closely matches the most conservative case described in [95], where the integrand of Eq. 2.8, $\frac{f(z)(1+z)^3}{h(z)}$, can be larger by three orders of magnitude in the most optimistic (high clumping) case. Gamma rays that are produced with energy E' are observed with redshifted energy $E = E'/(1+z)$. For annihilation into monoenergetic gamma rays, the delta function source spectrum is modified by redshift as

$$\frac{dN}{dE'} = 2\ \delta(m_\chi - E') = \frac{2}{E}\ \delta\left(z - (\frac{m_\chi}{E} - 1)\right)\ , \tag{2.9}$$

which shows that the observed flux at an energy E is contributed by sources at redshift $\frac{m_\chi}{E} - 1$.

2.3 Specific Observations and Derived Annihilation Constraints

We have collected gamma-ray flux measurements and limits from a wide variety of experiments, spanning an extensive energy range from 20 keV to 10 TeV. In most of the observations, the energy spectra are given in log-spaced energy intervals. We calculate annihilation gamma-ray fluxes for the Galactic, Andromeda, and cosmic dark matter sources, using the methods outlined in Section 2.2 above. These are integrated over an energy range, conveniently chosen as $10^{-0.4} m_\chi - m_\chi$, that is comparable to or larger than the energy resolution and bin size of the experiments. This is compared with observational data integrated over an energy bin. If only upper limits on the flux are given, we instead compare our predictions directly with these upper limits.

Our constraints on the dark matter annihilation rate are conservatively determined by demanding that the annihilation flux be smaller than 100% of the observed (presumably not produced only by dark matter) gamma-ray background flux at the corresponding energy range. In Fig. 2.1, we show the Galactic center and cosmic diffuse signals from dark matter annihilations which fulfill this criterion, superimposed upon the Galactic and extragalactic spectra, respectively, as measured by COMPTEL and EGRET.

The experiments report their results as either intensity (as in Eq. 2.4), which requires that we calculate $\mathcal{J}_{\Delta\Omega}$, or flux from a given angular region (as in Eq. 2.5), for which we need $\mathcal{J}_{\Delta\Omega}\Delta\Omega$. We present the values of these parameters which correspond to the Kravtsov profile, as this results in conservative upper limits on the annihilation cross section. Our limits on the dark matter annihilation cross section are reported in Fig. 2.2, where we also show how our results would change if the NFW profile were adopted instead. The details of the experiments and our analyses are summarized below for each observation.

2.3.1 COMPTEL and EGRET

COMPTEL [229], the imaging COMPton TELescope aboard the Compton Gamma Ray Observatory (CGRO) satellite, measured gamma rays in the energy range 1–30 MeV. EGRET [230], the Energetic Gamma Ray Experiment Telescope, also aboard the CGRO, measured gamma rays in the energy range 30 MeV to nearly 100 GeV. For both COMPTEL and EGRET, the full sky was studied with an angular resolution of at worst a few degrees (for the large regions we consider, this makes no difference). The energy resolution was modest, and the data were given in a few logarithmically-spaced bins per decade in energy.

Both COMPTEL and EGRET observed the Galactic Center region, and the measured gamma-ray intensity energy spectra are reported in Ref. [231, 232] for the region $-30^\circ < l < 30^\circ$ and $-5^\circ < b < 5^\circ$ (Galactic longitude and latitude, respectively). The disk-like morphology of the emission region makes it clear that nearly all of this emission is due to ordinary astrophysical sources; to be conservative, we do not attempt to define a limit on the small component of this that could be due

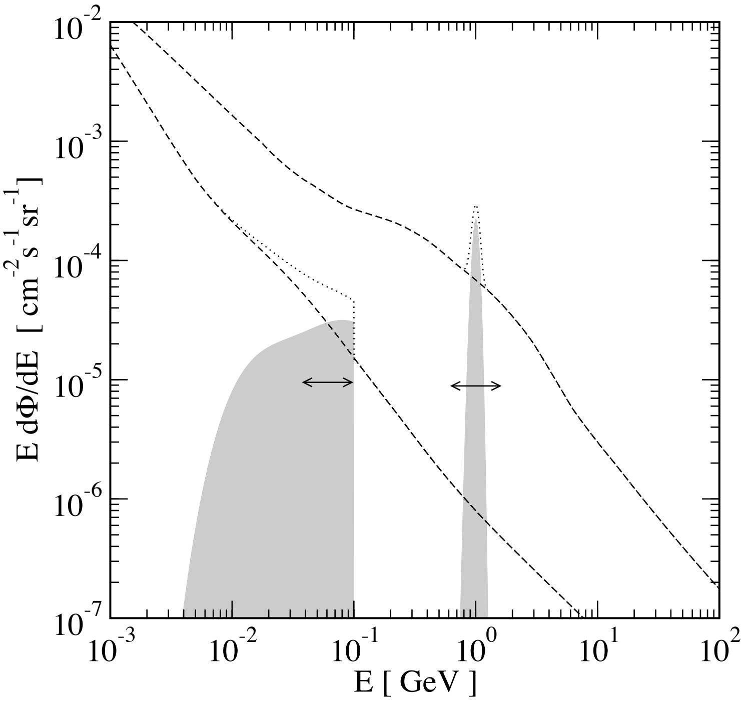

Figure 2.1: Example dark matter annihilation signals, shown superimposed on the Galactic and extragalactic gamma-ray spectra measured by COMPTEL and EGRET. In each case, the cross section is chosen so that the signals are normalized according to our conservative detection criteria, namely, that the signal be 100% of the size of the background when integrated in the energy range chosen (0.4 in $\log_{10} E$, shown by horizontal arrows). The narrow signal on the right is the Galactic Center flux due to annihilation into monoenergetic gamma rays, for $m_\chi = 1$ GeV; the signal is smeared as appropriate for a detection with finite energy resolution. The broad feature on the left is the cosmic diffuse signal for annihilation into monoenergetic gamma rays at $m_\chi = 0.1$ GeV, smeared by redshift.

to centrally-concentrated dark matter, and simply use the total observed intensity to bound any dark matter contribution. Also, we evaluate the dark matter signal as if from a circular region of $\psi = 30^\circ$; accounting for the rectangular shape of the region would lead to a higher value than the $\mathcal{J}_{\Delta\Omega} \simeq 13$ that we adopt. Using a less conservative set of assumptions than we employ, stronger limits on $\langle v\sigma\rangle_{\gamma\gamma}$ were derived from the EGRET data in Ref. [204].

2.3.2 H.E.S.S.

H.E.S.S. (High Energy Stereoscopic System), a system of multiple atmospheric Čerenkov telescopes, is presently in operation in Namibia [233]. H.E.S.S. observed the Galactic Center region in the energy range 0.3–15 TeV. An apparent point source at the Galactic Center was observed, as was an extended source ($\sim 1^\circ$) known as the Galactic Center Ridge [234]. While the origin of the point source is unknown, the Ridge emission is almost certainly astrophysical, and is consistent with being caused by cosmic rays colliding with a gas cloud (again, we do not attempt to account for this, and will simply bound any dark matter contribution by the total observed intensity).

Since the uncertainties in the dark matter profile increase for smaller angular regions around the Galactic Center, it is more robust to define our results using the extended region instead of the point source. The Ridge emission was observed in an angular region $-0.8^\circ < l < 0.8^\circ$ and $-0.3^\circ < b < 0.3^\circ$ in Galactic coordinates, and the resulting flux reported by H.E.S.S. reflected a background subtraction from a nearby region ($-0.8^\circ < l < 0.8^\circ$ and $0.8^\circ < b < 1.5^\circ$) to help account for cosmic rays. Thus, we have to consider not the whole dark matter signal, but just its contrast between the central and adjacent regions by accounting for this subtraction in our analysis. We approximate the intensity from the rectangular region of the Galactic Center Ridge with a circle of radius 0.8°.

Background Subtraction

We must account for the fact that the flux data is for the foreground region, and the subtracted background may have a component from dark matter annihilation. The most conservative way to do this is to assume the entirety of the background flux comes from dark matter annihilation. We also maximise $\mathcal{J}$ for the background, i.e, we assume $\psi = 0.8°$ for the entire background region. Then,

$$d\Phi/dE_{\mathrm{foreground}} = d\Phi/dE_{\mathrm{total}} - d\Phi/dE_{\mathrm{background}} \tag{2.10}$$

simplifies to

$$\mathcal{J}_{\Delta\Omega} = \frac{2\pi}{\Delta\Omega}\int_0^{0.8°} \left(\mathcal{J}(\psi) - \mathcal{J}(0.8°)\right)\sin\psi d\psi \simeq 3\,, \tag{2.11}$$

which is the value of $\mathcal{J}_{\Delta\Omega}$ we use to calculate the foreground annihilation signal, which we compare to the observed foreground flux. Had we not made this subtraction correction, our limits on the cross section would be stronger by about an order of magnitude.

2.3.3 INTEGRAL

The space-borne INTEGRAL (INTErnational Gamma-Ray Astrophysics Laboratory) observatory [235] has searched for gamma-ray emission in the Milky Way over the energy range 20–8000 keV, using the SPectrometer on INTEGRAL (SPI). Teegarden and Watanabe [236] presented results of an INTEGRAL search for gamma-ray line emission from the Galactic Center region (we use their zero-intrinsic-width results, as appropriate for the low dark matter velocities of the halo). Other than the expected positron annihilation [112] and ^{26}Al decay [237] signatures, no evidence of other line emission was found.

To reduce backgrounds and improve the sensitivity of the line search, the measured intensity from large angular radii ($> 30°$) was subtracted from that in the Galactic Center region ($< 13°$), resulting in a 3.5-σ constraint on the flux of very roughly $\lesssim 10^{-4}$ photons cm^{-2} s^{-1} in the energy range 20–8000 keV. Our calculations must reflect this subtraction, which will somewhat weaken the sensitivity to the dark matter signal. A similar correction was used in Ref. [238]. We use the same technique as we used with the H.E.S.S. signal, and implement this as

$$\mathcal{J}_{\Delta\Omega}\Delta\Omega = 2\pi \int_0^{13^\circ} \left(\mathcal{J}(\psi) - \mathcal{J}(> 30^\circ)\right) \sin\psi d\psi \simeq 2\,. \tag{2.12}$$

Due to the decreasing trend of the dark matter profile, the intensity outside the Galactic Center region will be largest at 30°, and accordingly we choose this value to be as conservative as possible (a larger subtraction leads to a weaker upper limit on $\langle v\sigma \rangle$). Had we not made this correction, our limits on the cross section would be stronger by about a factor of 2.

In the case of the INTEGRAL data, we do not need to integrate the calculated signal over an energy bin, since the data set we are comparing with is a gamma-ray line search. This reduces the background, leading to stronger constraints in this energy range.

2.3.4 Andromeda Halo Results

The Andromeda galaxy (M31) has been observed by several gamma-ray experiments, all of which placed upper limits on the flux. EGRET, CELESTE, and HEGRA all observed Andromeda, each encompassing a respectively smaller angular region of that extended object. As the results were reported as flux limits from specified angular regions, we compare to these using $\mathcal{J}_{\Delta\Omega}\Delta\Omega$, which is an input to Eq. (2.5).

EGRET viewed Andromeda with an angular radius of 0.5° and set a 2-σ upper limit on the gamma-ray flux of 1.6×10^{-8} photons cm^{-2} s^{-1} from 0.1 GeV to 2 GeV, since no signal was seen [239]. For the angular region of this observation, the flux will be proportional to

$$\mathcal{J}_{\Delta\Omega}\Delta\Omega = 2\pi \int_0^{0.5^\circ} \mathcal{J}'(\psi) \sin\psi d\psi \simeq 2 \times 10^{-3}\,. \tag{2.13}$$

CELESTE (ČErenkov Low Energy Sampling and Timing Experiment) is an atmospheric Čerenkov telescope in the French Pyrenees, which studies gamma rays with energies greater than 50 GeV [240]. It viewed Andromeda in the energy range of 50–700 GeV, and again no signal was seen [241]. A 2-σ upper limit on the energy-integrated flux from Andromeda was reported as $\lesssim 10^{-10}$ photons $\mathrm{cm}^{-2}\ \mathrm{s}^{-1}$; employing an angular radius of $\theta_{\mathrm{obs}} = 0.29°$ yields $\mathcal{J}_{\Delta\Omega}\Delta\Omega \simeq 1 \times 10^{-3}$.

HEGRA (High Energy Gamma Ray Astronomy experiment) was an atmospheric Čerenkov telescope, located in La Palma in the Canary Islands [242]. It took data in the range 0.5–10 TeV, with better energy resolution than that of CELESTE [243]. It used an even smaller angular radius of $\theta_{\mathrm{obs}} = 0.105°$, which yields $\mathcal{J}_{\Delta\Omega}\Delta\Omega \simeq 2\times10^{-4}$. HEGRA reported 99% C.L. upper limits for the gamma-ray line flux, and these can be used directly.

2.3.5 Cosmic Diffuse Results

INTEGRAL [244], COMPTEL [245] and EGRET [246] have all made measurements of the gamma-ray flux at high latitudes, and these can be used to set a limit on the cosmic dark matter annihilation signal. The INTEGRAL data used here were those collected in broad energy bins, much like those of COMPTEL and EGRET. The cosmic gamma-ray background was also measured by the Gamma-Ray Spectrometer aboard the Solar Maximum Mission (SMM) [247] over the energy range 0.3 – 8 MeV, for a field of view of 135° in the direction of the Sun [248], and we include this data.

For the cosmic diffuse analysis, the framework detailed in Section 2.2.2 can be applied. Note that for simplicity we calculate only the true cosmic diffuse dark matter signal, neglecting any Galactic contribution along the lines of sight. This contribution from the Galactic halo (which would add to the signal and thus make our limits stronger) is significant for NFW or steeper profiles and can even dominate over the true cosmic dark matter signal; see YHBA and Ref. [249].

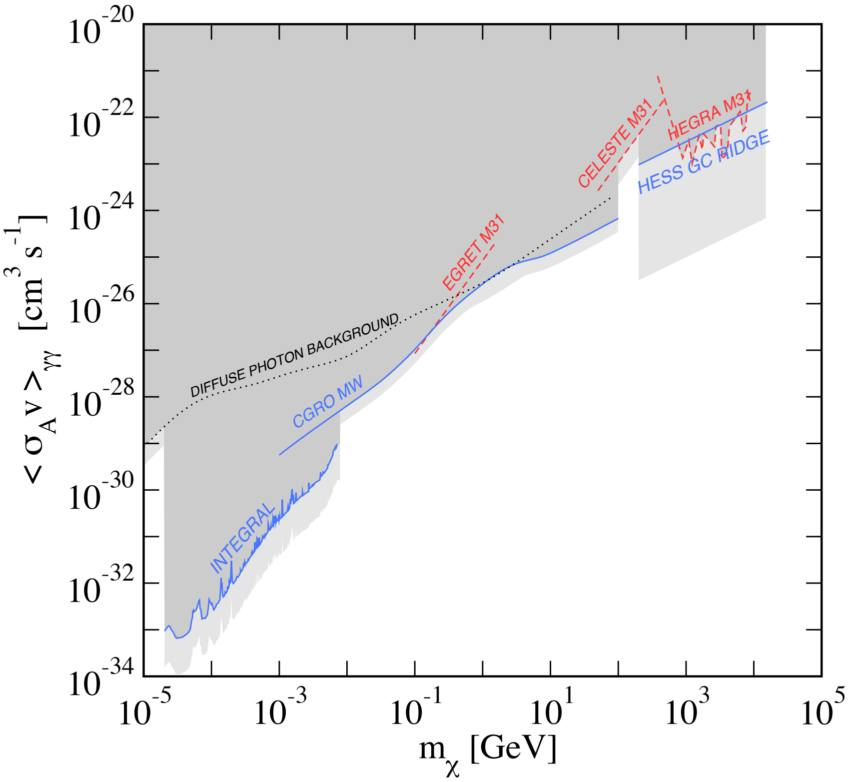

Figure 2.2: The limits on the partial cross section, $\langle v\sigma\rangle_{\gamma\gamma}$, derived from the various gamma-ray data. Our overall limit is shown as the dark shaded exclusion region. For comparison, the light-shaded region shows the corresponding limits for the NFW (rather than the Kravtsov) profile.

2.4 Discussion and Conclusions

2.4.1 Limits on the Cross Section to Gamma Rays

In Fig. 2.2, we combine all of the upper limits on the partial cross section to monoenergetic gamma rays, choosing the strongest limit for each value of the dark matter mass. The shaded exclusion region shows our combined bound. These searches for dark matter signals are limited by astrophysical backgrounds, and the general trend of how the limits vary with mass follows from how these backgrounds vary with energy. We can estimate how the cross section limit should scale with mass, and how it should depend on the assumed spectrum of final-state gamma rays and the choice of density profile.

Recall that we conservatively require the signal to be as large as the full measured background in an energy bin. The gamma-ray number flux of the signal integrated in a logarithmic energy bin $\Delta(\ln E)$ scales as $Ed\Phi/dE\,\Delta(\ln E) \sim \langle v\sigma\rangle/m_\chi^2$, provided that the bin is wide enough to contain the full signal. The gamma-ray number flux of the background integrated in the same logarithmic energy bin scales as $Ed\Phi/dE\,\Delta(\ln E) \sim E/E^\alpha\,\Delta(\ln E)$, for a background spectrum $d\Phi/dE \sim 1/E^\alpha$. For a narrow bin, the evaluation point is $E \sim m_\chi$. We then expect the upper limit on the cross section to scale as $\langle v\sigma\rangle_{limit} \sim m_\chi^{3-\alpha}\,\Delta(\ln E)$. For example, for the EGRET diffuse data, α is slightly greater than 2, and so the cross section limits in this energy range scale slightly less rapidly than as $\langle v\sigma\rangle_{limit} \sim m_\chi$.

Most of these experiments had modest energy resolution. To be conservative, we assume an analysis bin with a logarithmic energy width of 0.4 in $\log_{10} E$ (i.e., $\Delta(\ln E) \sim 1$) for the Galactic and cosmic diffuse analyses; this is at least as wide as the energy bins reported by the experiments. That is, even though we nominally assume two monoenergetic gamma rays at $E_\gamma = m_\chi$, our results have not taken advantage of this fact. In effect, our results are what one would obtain for an annihilation gamma-ray spectrum as wide as 0.4 in $\log_{10} E$. The exception is the INTEGRAL line search, where the excellent energy resolution is what leads to this limit being stronger than expected from the general trend in Fig. 2.2.

Due to radiative corrections [111, 191] (see Section 1.5) or energy-loss processes [75, 76, 77], there should be some gamma rays near the endpoint, and our results can be scaled if the assumed branching ratio is less than the 100% used in Fig. 2.2. For example, for charged-particle final states, the branching ratio to internal bremsstrahlung gamma rays near the endpoint is $Br(\gamma) \sim \alpha \sim 10^{-2}$. See also Chapter 3, where we use these internal bremsstrahlung gamma rays to place constraints on the annihilation rate to charged particles. For neutral final states, there will typically be gamma rays or neutrinos near the endpoint. To be conservative about these details, we chose a nominal minimum branching ratio to gamma rays near the endpoint of 10^{-4}, as outlined in Section 2.4.2.

How would our results change if we considered an even broader annihilation gamma-ray spectrum? We emphasize that the results shown in Fig. 2.2, which are based on direct numerical integration, are already valid for spectra as wide as our analysis bins. First, we should take into account the increase in the logarithmic bin width. Second, to be more precise, the evaluation point for the background spectrum should not be $E = m_\chi$, but rather $E = m_\chi/a$, with $a > 1$. This increases the estimate of the integrated background, and hence the cross section limit, by a factor $\sim a^{\alpha-1}$. Thus, if we took the annihilation gamma-ray spectrum to be as much as one order of magnitude wide, then our limits in Fig. 2.2 would be weakened by at most a factor of several, depending on the background spectrum. (For the INTEGRAL line search, the correction would be much larger.)

Given the large range on the axes in Fig. 2.2, and our intention to define approximate and conservative limits, this shows that our results are much more general than they first appear. Similarly, the results in BBM [74] and YHBA [2] do not have a strong dependence on assumed annihilation neutrino spectrum.

How sensitive are our limits to the choice of density profile? As noted, we chose the rather shallow Kravtsov profile to be conservative. If we were to adopt an NFW profile, which increases much more rapidly toward the Galactic Center (scaling with radius as r^{-1} rather than $r^{-0.4}$) the annihilation rates would be larger and the cross section limits correspondingly stronger. In Fig. 2.2, we show how our results would change if we had used an NFW profile instead of the Kravtsov profile. At most energies, the changes are modest, and illustrative of the potential uncertainties. The only significant change to the combined gamma-ray limit is for the H.E.S.S. Galactic Center Ridge case, which is based on small angular radii. In the NFW case, the steeper profile gives an overall larger intensity and a smaller signal cancelation when

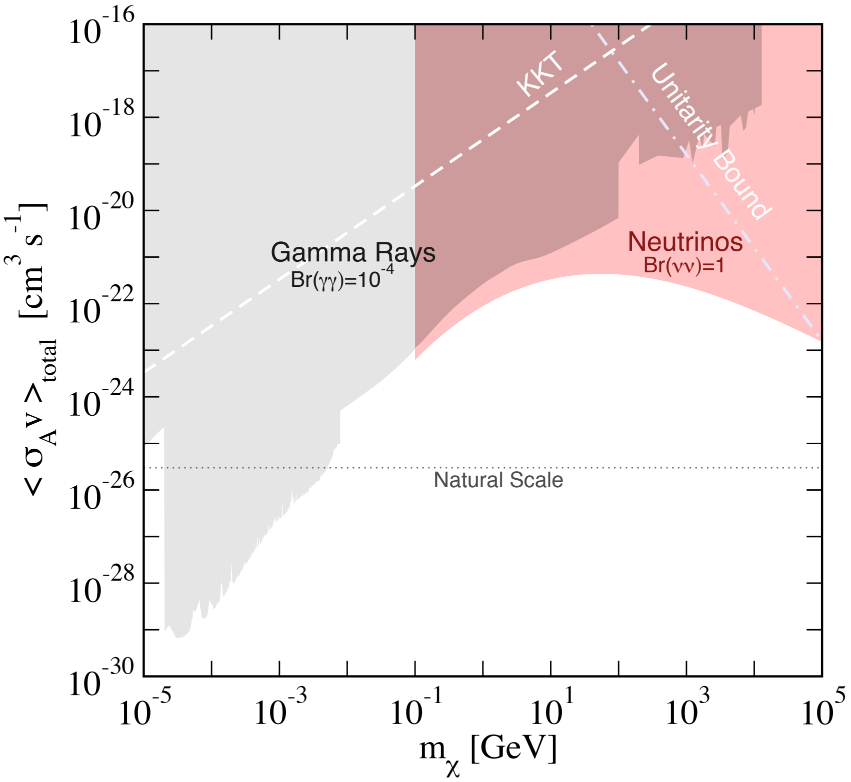

Figure 2.3: The gamma-ray and neutrino limits on the total annihilation cross section, selecting $Br(\gamma\gamma) = 10^{-4}$ as a conservative value. The unitarity and KKT bounds are also shown. The overall bound on the total cross section at a given mass is determined by the strongest of the various upper limits.

the background is subtracted. A fuller discussion of how the annihilation signals depend on the choice of dark matter density profile is given in YHBA.

Subsequent to publication of Ref. [250] which this chapter is based on, Refs. [251, 252] used data from Fermi to perform a gamma-ray line search between 1 and 400 GeV. As expected, the improved sensitivity of Fermi and a dedicated line search analysis of the data leads to strong upper limits over this energy range, although unlike our constraints, the upper limits will not apply to channels with broader annihilation spectra.

2.4.2 Limits on the Total Cross Section

Unsurprisingly, the cross section bounds derived under the assumption of monoenergetic gamma rays are substantially stronger than those defined similarly for final-state neutrinos in Refs. [74, 2]. (At the highest masses, near 10^4 GeV, this is no longer true, first because of how the values of the signal-to-background work out, and then because we do not presently have good gamma-ray data or limits at higher energies.) Indeed, this was an assertion in those two works that we have now justified in more detail than before.

It is unrealistic to have $Br(\gamma\gamma) = 100\%$, of course, if one is trying to set a limit on the *total* cross section. If $Br(\gamma\gamma)$ is known, then a limit on the total cross section can be determined by dividing the limit on the partial cross section to that final state by the branching ratio:

$$\langle v\sigma\rangle_{total} = \frac{\langle v\sigma\rangle_{\gamma\gamma}}{Br(\gamma\gamma)}. \tag{2.14}$$

In typical models, this process occurs via a loop diagram, with a branching ratio of 10^{-3} or smaller [20, 42, 43]. To be conservative, we must just choose a value such that it is implausible that the true branching ratio could be smaller. We therefore assume $Br(\gamma\gamma) = 10^{-4}$, but this choice could be debated. As noted, our analysis uses wide logarithmic energy bins, and so, at the very least, would capture the gamma rays near the endpoint due to internal bremsstrahlung from charged particles [111, 191]. (Similarly, as a general point, limits on the total cross section defined by assuming only W^+W^- final states [253] would have to be corrected by dividing by $Br(W^+W^-)$.)

Figure 2.3 summarizes various limits on the total cross section, including the one just described, the unitarity bound described in Section 1.3.1, and the neutrino bound described in Section 1.3.2 (based on the Milky Way signal and the Kravtsov profile). The constraint labelled 'KKT' comes from the requirement that annihilation does not drastically alter the density profiles of dark matter halos in the Universe today. In the model of Ref. [22], a large self-annihilation cross section was invoked in order to reconcile predicted cuspy density profiles with the flatter ones inferred from observation, requiring

$$\langle \sigma_A v \rangle_{\rm KKT} \simeq \left(3 \times 10^{-19}\ {\rm cm}^3\ {\rm s}^{-1}\right) \left[\frac{m_\chi}{\rm GeV}\right] . \tag{2.15}$$

We re-interpret this result as an approximate upper bound, beyond which halo density profiles would be significantly distorted by dark matter annihilation. Note that this limit is very weak for all but the lightest masses. The standard cross section for a thermal relic is also shown. Note that our limits bound $\langle v\sigma \rangle$ directly, independent of whether σ is s-wave or p-wave dominated. These results, combined with those in our Fig. 2.2, strongly constrain the possibilities for large dark matter annihilation signals, e.g., as assumed in Ref. [254].

When shown in this way, it becomes clear how surprisingly strong the neutrino bound on the *total* cross section is, as it is comparable to the bound obtained using the gamma-ray flux limits and a reasonable assumption about the minimum branching ratio to gamma rays. It is very important to emphasize that while the gamma-ray bound on the partial cross section had to be divided by a realistic $Br(\gamma\gamma)$, this is *not* the case for the neutrino bound, as explained above. If we assume only SM final states, then all final states besides neutrinos lead to appreciable fluxes of gamma rays, and hence are more strongly excluded. Of course, the gamma-ray and neutrino cross section limits can both be weakened by assuming an appreciable branching ratio to new and truly sterile particles.

2.4.3 Conclusions and Prospects

Using gamma-ray data from a variety of experiments, we have calculated upper limits on the dark matter annihilation cross section to gamma rays over a wide range of masses. These limits are conservatively defined, in terms of our analysis criteria, our assumptions about the uncertain dark matter density profiles, and the gamma-ray spectrum. While our results were nominally defined for monoenergetic gamma rays with $E_\gamma = m_\chi$, we have shown that all of our results except the INTEGRAL line flux limit are only weakly dependent on this assumption. The limits obtained for more general gamma-ray spectra would only be somewhat less stringent.

There are good prospects for improved sensitivity with present and upcoming gamma-ray experiments, particularly as Fermi and H.E.S.S. data continues to be released. As shown by Refs. [251, 252], detailed searches and analyses by the experimental collaborations themselves does also lead to improvements. These searches for dark matter signals are already background-limited, which will limit the possible improvements. Future experiments should be able to make reductions in the backgrounds by taking advantage of better energy and angular resolution, and by reducing the residual diffuse emission by subtracting astrophysical components and resolving individual sources.

Using a conservative choice on the branching ratio to gamma rays, namely $Br(\gamma\gamma) \simeq 10^{-4}$, we defined an upper limit on the *total* dark matter annihilation cross section by dividing our limits on the partial cross section to gamma rays by this branching ratio. At intermediate energies, the upper limit on the total cross section defined this way is comparable to previous upper limits defined using neutrinos [74, 2, 78]. The combined limit is considerably stronger than the unitarity bound [71, 72], or the cross section of Ref. [22], which would lead to substantial modifications of dark matter halos. For the relatively large cross sections considered here, the dark matter could not be a thermal relic; additional work is needed to push the sensitivity of these and other techniques down to the expected cross section scale for thermal relics.

3

Photon Bremsstrahlung Constraints on Dark Matter Annihilation into Charged Particles

3.1 Introduction

We focus here on the process $\chi\chi \to e^+e^-$ in which DM annihilates to an electron-positron pair, though we shall also look at the other charged leptons. Although the branching ratio to this particular final state is model-dependent, it is a significant channel in a wide range of models. For example, while annihilation to fermions is often helicity suppressed as described in Chapter 5, Kaluza-Klein DM features large (unsuppressed) annihilation rates to leptons [255, 256, 257], as does the Dirac DM model of Ref. [258]. Due to recent observations of an excess in the positron flux, numerous authors have proposed models in which annihilation to charged leptons is significantly enhanced, as discussed in detail in Section 1.3.6. This recent interest makes upper limits on the cross section to these annihilation products particularly interesting. In addition, various other SM final states, such as W^+W^- and ZZ, produce l^+l^- via their decays and hence a flux of charged leptons is of generic interest in a large variety of DM models.

Several techniques may be used to constrain the production of e^+e^- within galactic halos, many of which rely on the fact the charged particles inevitably produce photons. Signals considered include electrons, positrons, gamma rays, X-rays, microwaves and radio waves. Electrons and positrons undergo diffusion and energy loss processes between production and observation, introducing large uncertainties into the calculation. Photons are produced by the various energy loss processes that charged particles undergo in a galactic halo, examples of which include synchrotron radiation due to the propagation of $e^{\pm}$ in galactic magnetic fields, and inverse Compton scattering of electrons from interstellar radiation fields, e.g., [75, 76, 77, 259, 98, 253, 260, 261, 262, 263]. The drawback of these techniques is a significant dependence on astrophysical inputs, some of which are poorly known. Uncertainties in magnetic field strengths, radiation backgrounds, and electron diffusion scales all enter the calculations in an involved fashion. See Chapter 6 for a detailed discussion of diffusion.

Charged particles also produce photons via electromagnetic radiative corrections, introduced in Section 1.5; see also Refs. [111, 191, 192, 193, 194, 199, 264, 265, 266]. The lowest order dark matter annihilation process $\chi\chi \to e^+e^-$ is necessarily accompanied by the radiative correction $\chi\chi \to e^+e^-\gamma$. This is an *internal bremsstrahlung* (IB) process, also known as *final state radiation* (FSR), meaning that the photon arises at the Feynman diagram level and is not due to interaction of charged particles in a medium. Importantly, for a given annihilation cross section, $\langle v\sigma\rangle_{e^+e^-}$, the accompanying flux of IB photons can be determined without knowledge of the new underlying particle physics which mediates the DM annihilation. Moreover, IB suffers none the drawbacks of the competing inverse Compton and synchrotron techniques outlined above. While inverse Compton and synchrotron fluxes are dependent on conditions of the astrophysical environment, the IB flux is always present and its normalization and spectrum are pre-determined.

In this chapter we use IB emission to derive robust upper limits on the dark matter annihilation cross section to electron-positron pairs, $\langle v\sigma\rangle_{e^+e^-}$, over a wide DM mass range spanning $\sim 10^{-3} - 10^{4}$ GeV. We calculate DM annihilation fluxes produced in the Galactic halo, and compare with the gamma-ray backgrounds reported by COMPTEL, EGRET and H.E.S.S. We also look at data for the M31 (Andromeda) Galaxy, to fill a gap between the energy ranges covered by EGRET and H.E.S.S. We explicitly demonstrate how our limits vary according to the assumed DM halo profile (our one source of uncertainty) and also compare our limit on the annihilation cross section to $e^{+}e^{-}$ with corresponding bounds on the $\gamma\gamma$ and $\bar{\nu}\nu$ final states.

3.2 Internal Bremsstrahlung

If DM annihilates to produce charged particles, the lowest order processes will always be subject to electromagnetic radiative corrections, resulting in the production of real photons. In particular, the annihilation $\chi\chi \to e^{+}e^{-}$ will be accompanied by the internal bremsstrahlung process $\chi\chi \to e^{+}e^{-}\gamma$. A photon may be emitted from either the final state e^{+} or e^{-}, with a cross-section proportional to $\alpha \simeq 1/137$. See Refs. [267, 264, 111, 191] for a detailed discussion. Following Ref. [111], we use the cross section for the process $e^{+}e^{-} \to \mu^{+}\mu^{-}\gamma$, with emission from the final state muons only, as an analog for the similar process $\chi\chi \to e^{+}e^{-}\gamma$, replacing the electron and muon masses with the DM and electron masses respectively. From Refs. [111, 268, 269], the differential cross section for this process is

$$\frac{d\sigma_{\rm IB}}{dE} = \sigma_{\rm tot} \times \frac{\alpha}{E\pi}\left[\ln\left(\frac{s'}{m_e^2}\right) - 1\right]\left[1 + \left(\frac{s'}{s}\right)^2\right], \tag{3.1}$$

where E is the photon energy, $s = 4m_\chi^2$, $s' = 4m_\chi(m_\chi - E)$, and $\sigma_{\rm tot}$ is the tree-level cross section for $\chi\chi \to e^{+}e^{-}$. Note that $\sigma_{\rm tot}$ factors from the IB cross-section. This important feature implies that the IB spectrum is independent of the unknown physics which mediates the lowest order annihilation process [111] (See also Chapter 6 of [267]). The photon spectrum per $\chi\chi \to e^{+}e^{-}$ annihilation is therefore given by

$$\frac{dN_\gamma}{dE} = \frac{1}{\sigma_{\rm tot}}\frac{d\sigma_{\rm IB}}{dE_\gamma}. \tag{3.2}$$

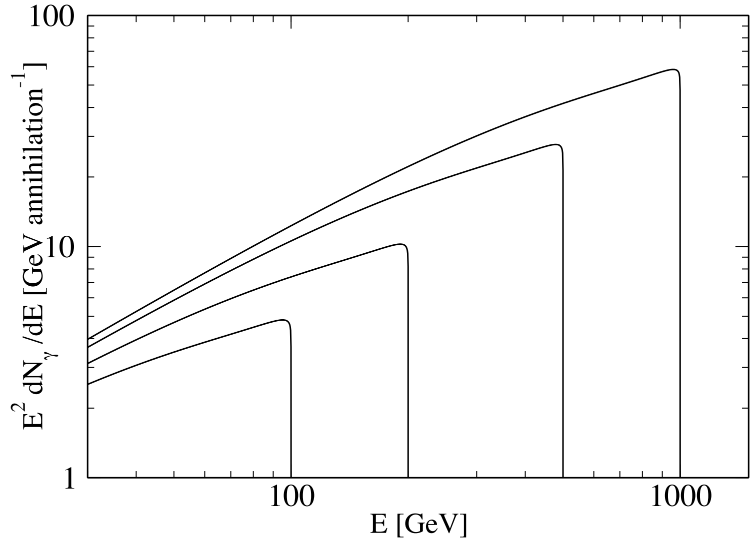

Figure 3.1: Internal bremsstrahlung gamma-ray spectra per $\chi\chi \to e^+e^-$ annihilation, for $m_\chi = 100$ GeV, 200 GeV, 500 GeV, 1000 GeV.

This spectrum is shown in Fig. 3.1 for various choices of the DM mass, where a sharp edge in the spectrum at $E = m_\chi$ is evident.

Note that we consider only radiation from the final state particles, and not from any internal propagators. In some supersymmetric scenarios in which annihilation to fermions is helicity suppressed, bremsstrahlung from internal propagators can be particularly important as it can circumvent this suppression; see Refs. [192, 193, 194, 199] and Chapter 5. We do not consider these model-dependent processes. Note, however, that the presence of such emission would only increase the gamma-ray flux we calculate, and hence strengthen the cross section limits derived.

3.3 Analysis of Annihilation flux

Our analysis technique is similar to that followed in Chapter 2. Recall that the gamma-ray flux per steradian due to DM annihilation in an observation region of angular size $\Delta\Omega$ is

$$\frac{d\Phi_\gamma}{dE} = \frac{\langle v\sigma\rangle}{2}\frac{\mathcal{J}_{\Delta\Omega}}{4\pi m_\chi^2 \mathrm{J}_0}\frac{dN_\gamma}{dE}, \tag{3.3}$$

where dN_γ/dE is the gamma-ray spectrum per annihilation, and all other parameters are defined in Section 2.2.1. For the IB emission associated with annihilation to $e^\pm$, we must replace $\langle v\sigma\rangle$ with $\langle v\sigma\rangle_{e^+e^-} = \langle v\sigma\rangle \times \mathrm{Br}(e^+e^-)$, while dN_γ/dE is given by Eq. 3.2.

In order to ensure our upper limits on the annihilation cross section are robust, we again adopt the conservative Kravtsov profile. We also show how results are strengthened by using the Moore or NFW profiles.

We use Galactic gamma-ray data from COMPTEL [229], EGRET [230] and H.E.S.S. [233], together spanning the broad energy range $10^{-3} - 10^4$ GeV. As there is a small gap between the energy ranges covered by EGRET and H.E.S.S., we use the observations of the M31 (Andromeda) galaxy made by CELESTE [240] to calculate constraints for this energy interval.

The Galactic gamma-ray background measurements reported by COMPTEL, EGRET and H.E.S.S. are given in approximately log-spaced energy intervals, with energy bins of size ranging from from $\Delta \log E \sim 0.2 - 0.6$. We calculate the IB gamma-ray flux for the observation regions viewed by these experiments, using the methods outlined above and in Section 2.2.1, and compare with the observational data. Upper limits on $\langle v\sigma\rangle_{e^+e^-}$ are determined by requiring that the IB flux due to DM annihilation be lower than 100% of the observed gamma-ray background flux in each of the experimental energy bins. Given that a large fraction of the observed gamma-ray background is likely to be astrophysical in origin, and not due to DM annihilation, taking the total background flux to be an upper limit on the DM annihilation signal is an extremely conservative approach.

For each energy bin, we take the DM mass to be equal to the upper energy limit of the bin, and integrate the IB flux over the width of the bin. Fig. 3.2 shows the quantity

$$\int_{E_{\min}}^{m_\chi} \frac{dN_\gamma}{dE} dE = \frac{1}{\sigma_{\mathrm{tot}}} \int_{E_{\min}}^{m_\chi} \frac{d\sigma_{\mathrm{IB}}}{dE} dE, \tag{3.4}$$

which is the number of photons per annihilation as a function of bin size, for IB emission from $e^{\pm}$, and $m_{\chi} = 1000$ GeV. (Since m_{χ} enters Eq. 3.1 via a logarithm, variation with m_{χ} is only very mild.) This indicates how the size of the energy bins affects our results. For comparison, the number of photons per annihilation for the process $\chi\chi \to \gamma\gamma$ (for which $dN_{\gamma}/dE = 2\delta(m_{\chi} - E)$) is also shown. Note that the IB cross section is proportional to $1/E$, so for sufficiently low photon energy the IB probability becomes large and one must account for multiple photon emission. However, we are not working in this regime, and in fact obtain our limits using the flux near the endpoint of the spectrum. Despite the fact that the IB flux is small, we have enough hard gamma rays near the endpoint to result in strong bounds. For typical parameters, the IB flux per annihilation to $e^{\pm}$ is smaller than the photon flux per annihilation for $\chi\chi \to \gamma\gamma$ by a factor of 10^2. This is expected, given that the IB cross section is suppressed by a factor of α with respect to the tree level DM annihilation process.

We compare the flux from COMPTEL, EGRET, H.E.S.S. and CELESTE with the IB signal calculated for an energy bin of size $10^{-0.4}m_{\chi} - m_{\chi}$. This is extremely conservative, as we are constraining the cross section by requiring that the annihilation flux in a small bin be less than or equal to the observed flux in a much larger bin.

3.4 Discussion

In Fig. 3.3 we show the upper limits on $\langle v\sigma \rangle_{e^+e^-}$ as a function of DM mass, using the observational data described above. We give the Galactic Center results for the conservative Kravtsov profile, the more commonly-adopted NFW profile, and the steep Moore profile. For the CELESTE observation of M31, differences between these profiles are expected to have a modest effect on the results, as a large portion of the galaxy is within the field of view; in Fig. 3.3 we show the CELESTE constraint using only the Kravtsov profile. As discussed in Section 2.2.1 and shown in Figure 1.2, while the Kravtsov, NFW and Moore profiles diverge towards the center of the Galaxy,

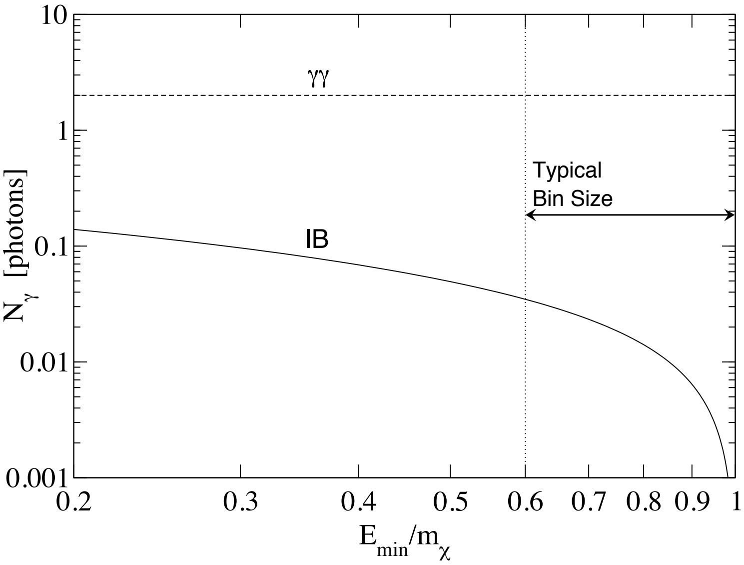

Figure 3.2: Number of gamma rays per DM annihilation ($\int_{E_{\rm min}}^{m_\chi} dE\ dN_\gamma/dE$) as a function of the lower limit of integration, for IB emission from $\chi\chi \to e^+e^-$ (solid). A typical bin size used in the analysis is shown. The DM mass used is 1000 GeV; variation with m_χ is very small. Shown for comparison is the number of photons per annihilation for the process $\chi\chi \to \gamma\gamma$ (dashed) in which the photons are always at the endpoint.

they are similar at large radii. This leads to large variations in $\mathcal{J}_{\Delta\Omega}$ between profiles for small observation regions around the Galactic center, and modest variations for large regions, as shown in Figure 1.4. This is manifest in our results. As the EGRET and COMPTEL observations encompass relatively large angular scales, the density profile changes have a modest effect. On the other hand, the H.E.S.S. constraints correspond to a much smaller angular region toward the Galactic Center, and vary by orders of magnitude depending on the profile adopted. As in Chapter 2, to be conservative, we do not consider the possibility that DM annihilation rates are enhanced due to substructure; such enhanced annihilation signals would result in stronger upper bounds on the cross section.

We can estimate the way that the cross section bounds scale with the DM mass.

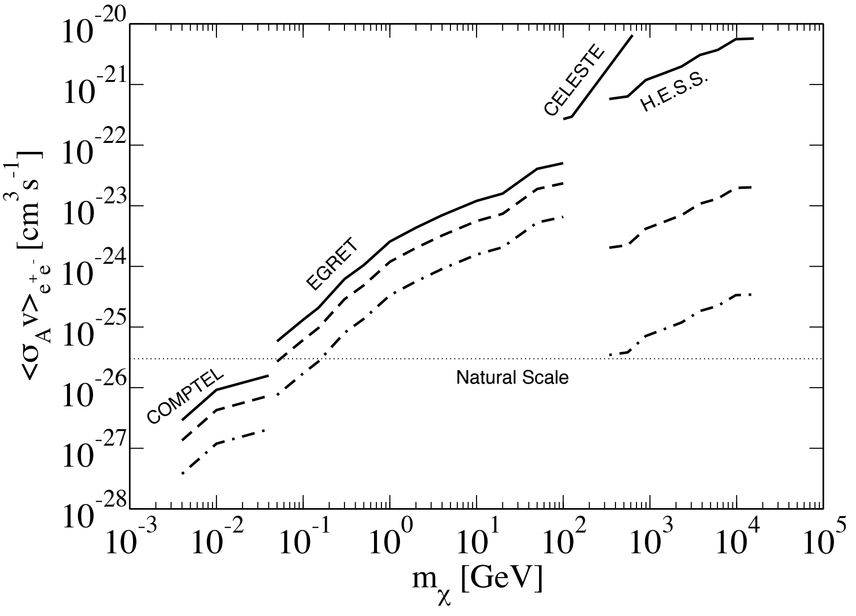

Figure 3.3: Upper limit on $\langle v\sigma\rangle_{e^+e^-}$ as a function of DM mass for the Kravtsov (solid), NFW (dashed) and Moore (dot-dashed) profiles.

The spectrum of the galactic gamma-ray background falls off with energy as $d\Phi/dE \sim E^{-\alpha}$ where, e.g., α is slightly larger than 2 in the EGRET and HESS energy ranges. The IB signal scales approximately as $d\Phi/dE \sim \langle v\sigma\rangle m_\chi^{-2}E^{-1}$ (where accounting the full energy dependence in Eq. 3.1 has only a small effect on this scaling). Given this scaling with E, it is clear that the strongest constraints arise from the endpoint of the spectrum. In addition, small bin size is optimal for obtaining strong constraints. If we integrate the flux over an energy bin of width xm_χ to m_χ, the IB flux within the energy bin is proportional to $\langle v\sigma\rangle m_\chi^{-2}$ (ignoring logarithmic corrections) while the background flux is proportional to $m_\chi^{-\alpha+1}$ (for fixed x). The cross section limits then scale with m_χ as $\langle v\sigma\rangle \sim m_\chi^{3-\alpha}$ and thus rise as m_χ if $\alpha \sim 2$.

In Fig. 3.4 we show the upper bounds on the annihilation cross sections into e^+e^-, $\mu^+\mu^-$, and $\tau^+\tau^-$, based upon the IB emission from each final state (all use the conservative Kravtsov profile). As the mass of the charged lepton increases, the rate of IB emission decreases and thus the upper bounds on the cross sections become

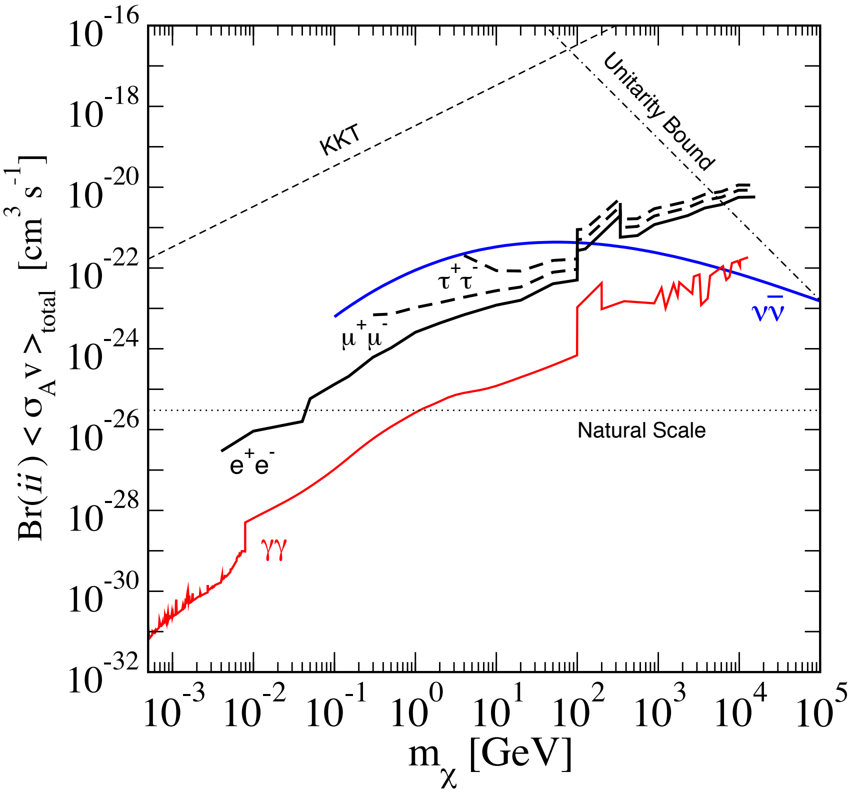

Figure 3.4: Upper limits on the *partial* cross sections $Br(ii) \times \langle v\sigma \rangle_{total}$ for various final states $ii = e^+e^-$ (solid black; labelled), $\mu^+\mu^-$ (thick dashed; labelled), $\tau^+\tau^-$ (thick dashed; labelled), $\gamma\gamma$ (red; labelled), and $\bar{\nu}\nu$ (blue; labelled), using the conservative Kravtsov profile. Each of these partial cross section limits is independent, with no relationship assumed between the branching ratios to particular final states. Also shown are the KKT (thin dashed) and unitarity (thin dot-dashed) limits on the *total* cross section described in the text, and the cross section for thermal relic DM (natural scale). The $\gamma\gamma$ and $\bar{\nu}\nu$ limits are taken from Fig. 2.2 and Ref. [2], respectively.

weaker. However, as the IB spectrum depends only logarithmically on the charged lepton mass, this effect is mild, particularly for large DM mass. We have used Eq. 3.1 to calculate the IB flux over the entire mass range, and present limits which range from high m_χ down to just above threshold. We expect modifications to Eq. 3.1 in the limit that the charged leptons are non-relativistic, but this will only affect a small mass range close to threshold. In the case of annihilation to $\tau^\pm$, we have not considered the gamma rays that arise from hadronic decay modes of the τ leptons (see e.g., Ref. [191]) which form a broad spectrum centered on the pion mass.

Using Fig. 3.4, we may compare the limit on the annihilation cross section into e^+e^- with that for $\gamma\gamma$ from Fig. 2.2. As anticipated, the bound on $\langle v\sigma\rangle_{e^+e^-}$ from IB is weaker than the bound on $\langle v\sigma\rangle_{\gamma\gamma}$ by a factor of $\sim 10^{-2} \sim \alpha$. This difference can be understood by comparing the number of hard gammas near the endpoint, $E_\gamma = m_\chi$. For annihilation to $\gamma\gamma$, there are always two monoenergetic gamma rays at the endpoint. The IB spectrum, integrated over a typical bin width (see Fig. 3.2) results in a flux that is smaller than this by only a factor of less than 100. That IB provides a limit this close to the ideal $\gamma\gamma$ channel illustrates the importance of the IB technique.

We stress that our IB limits apply to the *partial* DM annihilation cross sections, $\langle v\sigma\rangle_{l^+l^-}$, rather than the *total* annihilation cross section, $\langle v\sigma\rangle$. The two are related via $\langle v\sigma\rangle_{l^+l^-} = Br(l^+l^-)\langle v\sigma\rangle$. While the branching ratios are entirely dependent on the choice of DM model, there are many scenarios which feature large branching ratios for direct annihilation to leptons, such as Kaluza-Klein DM, or the models reviewed in e.g. Refs. [151, 152, 153]. Our constraints can be readily applied to any particular model, simply by dividing the $\langle v\sigma\rangle_{l^+l^-}$ bounds by the relevant branching ratios.

Also shown in Fig. 3.4 are a number of upper bounds on the *total* annihilation cross-section: the unitarity limit (see Section 1.3.1), and the KKT limit described in Section 2.4.2. Recall that the limit on annihilation to $\bar{\nu}\nu$ also defines a strong bound on the *total* DM annihilation cross section, as shown in Section 1.3.2. If we assume annihilation to only Standard Model final states, a conservative bound on the total cross section is obtained by assuming the branching ratio to neutrinos (the least detectable final state) is 100%. Any other assumption would lead to appreciable fluxes of gamma rays and hence be more strongly constrained. Dark matter annihilation into neutrinos was examined in Refs. [74] and [2]. The upper bound on $\langle v\sigma \rangle_{\bar{\nu}\nu}$ shown in Fig. 3.4 (taken from [2]) shows that the neutrino constraints are quite strong, particularly for large DM mass. In fact, due to electroweak bremsstrahlung (radiation of W and Z bosons, rather than photons) neutrinos are also inevitably accompanied by photons and other particles; See Chapters 4, 5 and Refs. [82, 83, 84, 85]. The rate of this emission is model-dependent, and the resulting bounds can be weaker or stronger than the bounds from neutrinos, as seen by comparing Chapter 6 with Ref. [83].

If DM annihilates to $e^{\pm}$, photons will be produced not only by IB, but also by energy loss processes including inverse Compton scattering and synchrotron radiation. In particular, radio wavelength signals produced via synchrotron emission have been the focus of much recent attention, e.g., [98, 253, 260, 261, 262]. However, the intensity of synchrotron radiation depends on a number of uncertain astrophysical parameters, such as magnetic field strength, radiation field intensities, and electron diffusion scales. By contrast, IB is free of these astrophysical uncertainties, and has a fixed spectrum and normalization. Another key difference is the energy of the photons. Synchrotron radiation produces generally low energy photons, while IB provides some hard gamma rays near the endpoint. Since the background flux falls off with energy, these hard gamma rays are extremely useful. The sharp edge in the IB spectrum at $E = m_\chi$ can be used to diagnose the DM mass; this is not possible with synchrotron radiation.

Nonetheless, it useful to take the synchrotron based cross section bounds as a reference point to compare with our IB based bounds. Our conservative IB bound on $\langle v\sigma\rangle_{e^+e^-}$ is comparable to conservative bounds on $\langle v\sigma\rangle_{W^+W^-}$ obtained from synchrotron radiation. For example, Ref. [262] obtains $\langle v\sigma\rangle_{W^+W^-} \lesssim 4 \times 10^{-24}\text{cm}^3\text{s}^{-1}$ ($4 \times 10^{-23}\text{cm}^3\text{s}^{-1}$) at 100 GeV (1 TeV) assuming an NFW profile and conservative magnetic field choices (lower panel of Fig. 6 in Ref. [262]). This is to be compared with our IB result of $\langle v\sigma\rangle_{e^+e^-} \lesssim 2 \times 10^{-23}\text{cm}^3\text{s}^{-1}$ ($4 \times 10^{-24}\text{cm}^3\text{s}^{-1}$) at 100 GeV (1 TeV), again assuming an NFW profile. (The results of Ref. [262] are very similar to those of Ref. [260], though weaker than those of Ref. [253], in which less conservative assumptions were made.) Note that these synchrotron studies assume annihilation to W^+W^- (or $\bar{q}q$) which then decay to electrons, rather than direct annihilation to e^+e^-. Therefore, these electrons are not at the DM mass, and have instead a broad distribution of energies centered on the W mass. The synchrotron analyses in [262, 260, 253] thus serve only as an interesting reference point for our work, and not as a direct comparison.

Many groups have recently proposed models in which DM annihilates directly to charged leptons, with cross sections well above that expected for a thermal relic. This may account for anomalies in cosmic ray spectra from Fermi, PAMELA and ATIC, and microwave signals from WMAP, all of which seem to require more electrons and positrons than can be explained otherwise; see Sections 1.3.5 and 1.3.6 for details. Our bounds on $\langle v\sigma\rangle_{l^+l^-}$ directly constrains the allowed parameter space for these types of DM models.

3.5 Conclusions

Dark matter annihilation into charged particles will necessarily be accompanied by gamma rays. Internal bremsstrahlung from final state charged particles can produce hard gamma rays, close to the endpoint defined by $E_\gamma = m_\chi$, with an approximately model independent spectrum. Using Galactic gamma-ray data, we have calculated upper limits on the dark matter annihilation cross section to e^+e^- and other charged leptons. We have made conservative assumptions about the astrophysical inputs, and demonstrated how our derived bounds would be strengthened if the Galactic halo has a steeper density profile than assumed. The upper bound on the annihilation cross section into e^+e^- is weaker than that for the ideal $\gamma\gamma$ final state by only a factor of $\lesssim 10^2$. For a wide range of masses, our upper bound on $\langle v\sigma \rangle_{e^+e^-}$ is stronger than the bound on the total cross section defined by neutrinos, the least detectable final state. Compared with recent constraints on DM annihilation cross sections based upon synchrotron radiation, the internal bremsstrahlung constraints on $\langle v\sigma \rangle_{e^+e^-}$ are broadly comparable in strength. However, synchrotron emission depends strongly on poorly known astrophysical inputs, such as Galactic magnetic field strengths. In comparison, the normalization and spectrum of IB radiation is fixed, independent of any astrophysical inputs, and is thus an extremely clean technique.

4

Electroweak Bremsstrahlung in Dark Matter Annihilation into Neutrinos

4.1 Introduction

In Chapter 3 we have shown that dark matter annihilation to charged particles will always be accompanied by gamma rays due to photon bremsstrahlung. In addition, electroweak bremsstrahlung of massive $W^{\pm}$ and Z gauge bosons, introduced in Section 1.5, is important to consider. The decay of the W/Z's will inevitably lead to production of photons, hadrons and leptons, even if the dark matter annihilates only into neutrinos at the $2 \rightarrow 2$ level. In this Chapter we consider such a model.

The general upper bound on the *total* DM annihilation cross section defined via the limit on $\chi\chi \rightarrow \bar{\nu}\nu$, described in Section 1.3.2, is surprisingly strong. (See Chapter 2 for a comparison between photon-based and neutrino-based limits.) However, as we have hinted, a scenario in which neutrinos alone are produced in the final state is technically impossible. Even leaving aside the theoretical issue that a direct coupling of DM to only neutrinos violates the $SU(2)$-invariance of the weak interaction, electroweak radiative corrections imply indirect couplings to states other than neutrinos. For example, for energies above $m_{W,Z}$, electroweak bremsstrahlung of W

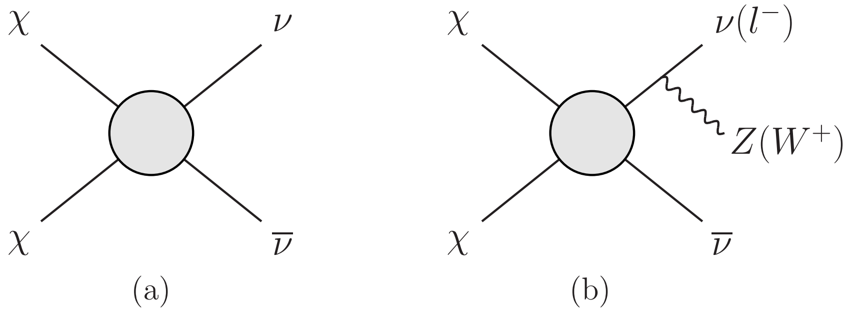

Figure 4.1: The lowest order tree level process $\chi\chi \rightarrow \bar{\nu}\nu$ (left) is accompanied by electroweak bremsstrahlung processes (right).

or Z bosons can occur at sizeable rates [82, 83, 85, 195, 196, 197, 198] (see Fig. 4.1). The hadronic decays of these gauge bosons produce neutral pions, which decay to gamma rays. Even for energies below m_W, processes involving virtual electroweak gauge bosons will lead to particles with electromagnetic interactions, though the rate for such processes is suppressed at low energy.

Kachelriess and Serpico have estimated the constraints on the cross section for $\chi\chi \rightarrow \bar{\nu}\nu$ (and hence on total DM annihilation cross section) by considering gamma rays produced via the accompanying process $\chi\chi \rightarrow \bar{\nu}\nu Z$ [82]. This was updated in [83]. We present here an explicit calculation of the branching ratios for the electroweak bremsstrahlung processes $\chi\chi \rightarrow \bar{\nu}\nu Z$ and $\chi\chi \rightarrow \bar{\nu}eW$.

4.2 W-strahlung

We shall first consider DM annihilation to four body final states via W-strahlung, an example of which is the $\chi\chi \rightarrow e^+e^-\bar{\nu}\nu$ process shown in Fig. 4.2, and calculate the ratio of the cross section for this process, to that for the lowest order tree level process $\chi\chi \rightarrow \bar{\nu}\nu$. For simplicity, we will assume that the coupling between the DM-current and the neutrino-current is mediated by a scalar boson "B". Given this scalar coupling, the terms in the matrix element involving the initial state (χ) particles will factorize from the full matrix element. It is thus useful to consider the

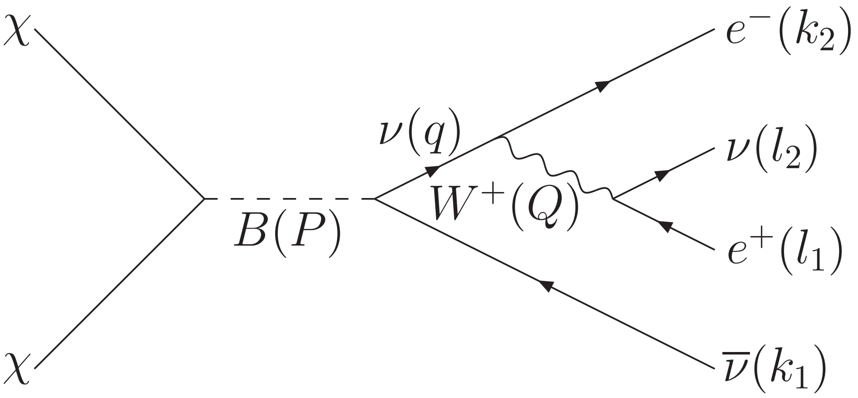

Figure 4.2: Feynman diagram for the W-strahlung process $\chi\chi \rightarrow e^-\bar{\nu}W^{+*} \rightarrow e^+e^-\bar{\nu}\nu$

matrix element for the decay of the virtual B^*.

We will first discuss the phase space calculation, and begin by noting that it is useful to treat the process shown in Fig. 4.2 as a sequence of three $1 \rightarrow 2$ particle decays of a virtual particle, viz., $B^*(P) \rightarrow \nu^*(q) + \bar{\nu}(k_1)$, followed by $\nu^*(q) \rightarrow W^{*+}(Q) + e^-(k_2)$, followed by $W^{*+}(Q) \rightarrow \nu(l_2) + e^+(l_1)$. The four-body final state Lorentz-Invariant Phase Space (LIPS) is given by

$$\begin{aligned} LIPS^{(4)} &= (2\pi)^4 \int dk_2 \int dk_1 \int dl_2 \int dl_1 \\ &\times \delta^4(P - l_1 - l_2 - k_1 - k_2)\,, \end{aligned} \tag{4.1}$$

where $dk \equiv (2\pi)^{-3}\, d^3\vec{k}/2k_0$, etc. We integrate over the momenta of the virtual particles by inserting

$$d^4q\, d^4Q\, \delta^4(q - k_2 - Q)\, \delta^4(Q - l_1 - l_2), \tag{4.2}$$

which ensures momentum conservation for the virtual processes. The phase space then factorizes into a product of three separate two-body phase space factors convolved over the two virtual particle momenta:

$$\begin{aligned}LIPS^{(4)} &= \int\frac{dq^2}{2\pi}\int\frac{dQ^2}{2\pi}\left(\int(2\pi)^4\delta^4(P-q-k_1)\,dq\,dk_1\right)\\ &\quad\times\left(\int(2\pi)^4\delta^4(q-Q-k_2)\,dQ\,dk_2\right)\left(\int(2\pi)^4\delta^4(Q-l_1-l_2)\,dl_1\,dl_2\right)\\ &= \int\frac{dq^2}{2\pi}\int\frac{dQ^2}{2\pi}\int dLIPS^{(2)}(P^2,q^2,k_1^2)\\ &\quad\times\int dLIPS^{(2)}(q^2,Q^2,k_2^2)\int dLIPS^{(2)}(Q^2,l_2^2,l_1^2)\,.\end{aligned}\tag{4.3}$$

Each two-body differential phase space factor is easily evaluated in the respective two-body center of momentum (CoM) frame, using the expression

$$dLIPS^{(2)}(x,y,z)=\frac{1}{8\pi}\frac{\sqrt{\lambda(x,y,z)}}{x}\left(\frac{d\Omega}{4\pi}\right)\,,\tag{4.4}$$

which we derive as follows. We begin with

$$dLIPS^{(2)}(E_{\mathrm{CM}}^2,p_1^2,p_2^2)=\frac{2|\vec{p}|}{E_{\mathrm{CM}}}\frac{1}{8\pi}\left(\frac{d\overline{\Omega}}{4\pi}\right)\,,\tag{4.5}$$

from A.58 of [267], where $d\overline{\Omega}$ is the CoM solid angle, and $|\vec{p}|=|\vec{p}_1^{\,\mathrm{CM}}|=|\vec{p}_2^{\,\mathrm{CM}}|$. We can evaluate $|\vec{p}|$ in terms of the total energy of the system and the final state particle four-momenta squared, p_1^2, p_2^2 (which for an on-shell particle is the mass squared),

$$\begin{aligned}|\vec{p}|^2 &= E_1^2-p_1^2=E_2^2-p_2^2\\ \rightarrow E_2^2 &= E_1^2-p_1^2+p_2^2.\end{aligned}\tag{4.6}$$

Eliminating E_2 from 4.6 using $E_{\mathrm{CM}}=E_1+E_2$,

$$\begin{aligned}E_{\mathrm{CM}}^2-2E_{\mathrm{CM}}E_1+E_1^2 &= E_1^2-p_1^2+p_2^2\\ E_1 &= \frac{E_{\mathrm{CM}}^2+p_1^2-p_2^2}{2E_{\mathrm{CM}}},\end{aligned}\tag{4.7}$$

we find

$$\begin{aligned}\frac{2|\vec{p}|}{E_{\mathrm{CM}}} &= \frac{2\sqrt{E_1^2-p_1^2}}{E_{\mathrm{CM}}}=\frac{2\sqrt{\left(\frac{E_{\mathrm{CM}}^2+p_1^2-p_2^2}{2E_{\mathrm{CM}}}\right)^2-p_1^2}}{E_{\mathrm{CM}}}\\ &= \frac{\sqrt{\lambda(E_{\mathrm{CM}}^2,p_1^2,p_2^2)}}{E_{\mathrm{CM}}^2}\end{aligned}\tag{4.8}$$

where $\lambda(x,y,z)$ is the triangle function given by

$$\lambda(x,y,z) = x^2 + y^2 + z^2 - 2xy - 2xz - 2yz\,. \tag{4.9}$$

We can then write the phase space in a form useful for our calculation,

$$\begin{aligned} LIPS^{(4)} &= \frac{1}{16}\frac{1}{(2\pi)^4}\int_0^{P^2} dq^2 \int_0^{q^2} dQ^2\, \frac{\sqrt{P^4+q^4-2P^2q^2}}{P^2}\left(\frac{d\overline{\Omega}_P}{4\pi}\right) \\ &\quad \times \frac{\sqrt{q^4+Q^4-2q^2Q^2}}{q^2}\left(\frac{d\overline{\Omega}_q}{4\pi}\right) \\ &= \frac{1}{16}\frac{1}{(2\pi)^4}\int_0^{P^2} dq^2 \int_0^{q^2} dQ^2\, \frac{(P^2-q^2)(q^2-Q^2)}{P^2\,q^2} \\ &\quad \times \left(\frac{d\overline{\Omega}_P}{4\pi}\right)\left(\frac{d\overline{\Omega}_q}{4\pi}\right)\int dLIPS^{(2)}(Q^2,0,0)\,. \end{aligned} \tag{4.10}$$

Here and throughout, we neglect the masses of the leptons, hence $k_1^2 = k_2^2 = l_1^2 = l_2^2 = 0$. We next calculate the matrix element for $B^* \to \bar{\nu}_e\, e^- W^{+*} \to \bar{\nu}_e\, e^- \nu_e\, e^+$, which is given by

$$\begin{aligned} \mathcal{M}_W = g_B \frac{g^2}{2}\left[\bar{u}(k_2)\gamma_\mu P_L \frac{\not{q}+m_\nu}{q^2-m_\nu^2} v(k_1)\right] \\ \times \left[\bar{u}(l_2)\gamma_\nu P_L\, v(l_1)\right]\left(-g^{\mu\nu} + \frac{Q^\mu Q^\nu}{m_W^2}\right)\left(\frac{1}{Q^2-m_W^2+im_W\Gamma_W}\right), \end{aligned} \tag{4.11}$$

where we use the projection operator $P_L = \frac{1-\gamma^5}{2}$, and the (non-standard) $B\nu\bar{\nu}$ and (standard) $W\nu e$ couplings are g_B and $g/\sqrt{2} = e/\sqrt{2}\sin\theta_w$, respectively. We have expressed the matrix element in Eq. (4.11) in Unitary gauge, where we do not need to include diagrams with unphysical Goldstone bosons. After squaring and summing over spins, we find

$$\begin{aligned} \sum_{\text{spins}} |\mathcal{M}_W|^2 &= \frac{g_B^2\, g^4}{4q^4[(Q^2-m_W^2)^2+(m_W\Gamma_W)^2]^2}\,\mathrm{Tr}\left[\not{k}_1\gamma_\mu\not{q}\not{k}_1\not{q}\gamma_\lambda P_L\right] \\ &\times \quad \mathrm{Tr}\left[\gamma_\beta\gamma_\nu\gamma_\alpha\gamma_\rho P_L\right]\ell^\alpha\ell^\beta\left(-g^{\mu\nu}+\frac{Q^\mu Q^\nu}{m_W^2}\right)\left(-g^{\lambda\rho}+\frac{Q^\lambda Q^\rho}{m_W^2}\right) \end{aligned} \tag{4.12}$$

The gauge boson momentum $Q = l_1 + l_2$, and so when contracted with the traces, the $\frac{Q^\mu Q^\nu}{m_W^2}$ and $\frac{Q^\lambda Q^\rho}{m_W^2}$ terms are each proportional to $l_{1,2}^2/m_W^2$. Recall that we neglect the mass of the $l_{1,2}$ particles, and so we consider the $g^{\mu\nu}g^{\lambda\rho}$ term only. We then evaluate the traces and perform the integration over the momenta l_1 and l_2 to obtain

$$\begin{aligned}\int dLIPS^{(2)}(Q^2,0,0)\sum_{\text{spins}}|\mathcal{M}_W|^2 &= \frac{1}{3\cdot 2^4\,(2\pi)}\,\frac{g_B^2\,g^4}{q^4\,[(Q^2-m_W^2)^2+(m_W\Gamma_W)^2]} \\ &+\Big[8s\,(Q\cdot k_2)(Q\cdot q)+4s\,Q^2\,(k_2\cdot q)-8q^2\,(Q\cdot k_2)(Q\cdot P)-4Q^2\,q^2\,(k_2\cdot P)\Big] \\ &= \frac{1}{3\cdot 2^4\,(2\pi)}\,\frac{g_B^2\,g^4}{q^4\,[(Q^2-m_W^2)^2+(m_W\Gamma_W)^2]}(s-q^2)(q^2-Q^2)(q^2+2Q^2)\end{aligned} \tag{4.13}$$

where $s\equiv P^2$ is the center of mass energy squared, and we have made use of the identity

$$\int dLIPS^{(2)}(Q^2,0,0)\;l_1^\alpha l_2^\beta=\frac{1}{96\pi}\,[2Q^\alpha Q^\beta+Q^2 g^{\alpha\beta}]\,. \tag{4.14}$$

and the scalar products

$$\begin{aligned} k_1\cdot k_2 &= \frac{(q^2-Q^2)(P^2-q^2)}{4\,q^2} \\ q\cdot k_2 &= \frac{q^2-Q^2}{2} \\ q\cdot Q &= \frac{q^2+Q^2}{2} \\ q\cdot k_1 &= \frac{P^2-q^2}{2}. \end{aligned} \tag{4.15}$$

We now multiply this partial result by the remaining part of the phase space in Eq. (4.10), and perform the integrations over $d\overline{\Omega}_P$, $d\overline{\Omega}_q$, and q^2, to obtain

$$\begin{aligned}\int dLIPS^{(4)}\sum_{\text{spins}}|\mathcal{M}_W|^2 &= \frac{g_B^2\,g^4}{3\cdot 2^8(2\pi)^5 s}\int_0^s dQ^2\frac{1}{(Q^2-m_W^2)^2+(m_W\Gamma_W)^2} \\ &\times\int_s^{Q^2} dq^2\frac{(s-q^2)^2\,(q^2-Q^2)^2\,(q^2+2Q^2)}{q^6}\left(\frac{d\overline{\Omega}_P}{4\pi}\right)\left(\frac{d\overline{\Omega}_q}{4\pi}\right) \\ &= \frac{g_B^2\,g^4}{9\cdot 2^8(2\pi)^5 s}\int_0^s dQ^2\frac{1}{(Q^2-m_W^2)^2+(m_W\Gamma_W)^2} \\ &\times\left(-s^3+9\,Q^2\,s^2+9\,Q^4\,s-17\,Q^6+6\,Q^4(Q^2+3\,s)\,\ln\left[\frac{Q^2}{s}\right]\right) \\ &= \frac{g_B^2\,g^4}{9\cdot 2^8(2\pi)^5}\int_0^1 dy\frac{x_W^2\,s}{(y\,x_W-1)^2+\left(\frac{\Gamma_W}{m_W}\right)^2} \\ &\times\left(1+17\,y^3-9\,y^2-9\,y-(6\,y^3+18\,y^2)\,\ln(y)\right),\end{aligned} \tag{4.16}$$

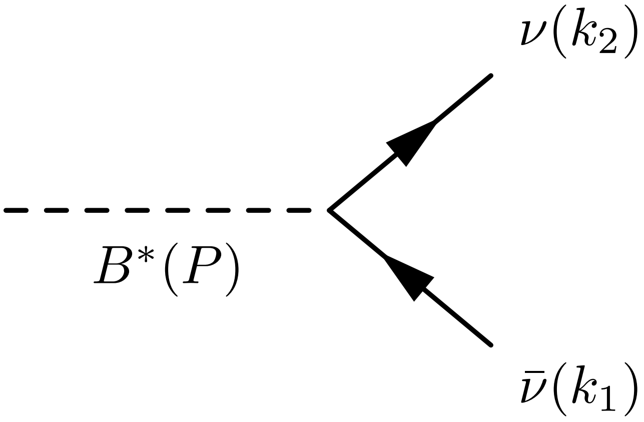

Figure 4.3: Feynman diagram for the process $B^* \to \nu\bar{\nu}$

expressed in terms of dimensionless scaling variables $y \equiv Q^2/s$ and $x_W \equiv s/m_W^2$. We wish to compare this rate with that for the $B^* \to \nu_e\bar{\nu}_e$, shown in Fig. 4.3. The matrix element for this process is

$$\mathcal{M}_{\nu\bar{\nu}} = \bar{u}(k_2)\, g_B\, v(k_1), \tag{4.17}$$

where k_1, k_2 are the momenta of the final state neutrinos. Evaluating in the CoM frame, we find

$$\begin{aligned} \int dLIPS^{(2)} \sum_{\text{spins}} |\mathcal{M}_{\nu\bar{\nu}}|^2 &= \int \frac{g_B^2}{4\pi^2}\,(k_1 \cdot k_2)\,\delta^4(P - k_1 - k_2)\,\frac{d^3\vec{k_1}\,d^3\vec{k_2}}{E_1\,E_2} \\ &= \frac{g_B^2\,s}{4\pi} \end{aligned} \tag{4.18}$$

The resulting expression for the ratio of rates for these two processes is

$$\begin{aligned} \frac{\int dLIPS^{(4)} \sum_{\text{spins}} |\mathcal{M}_W|^2}{\int dLIPS^{(2)} \sum_{\text{spins}} |\mathcal{M}_{\nu\bar{\nu}}|^2} &= \frac{\Gamma(\to \bar{\nu}_e e^- W^{*+} \to \nu_e\bar{\nu}_e e^+ e^-)}{\Gamma(\to \nu_e\bar{\nu}_e)} \\ = \frac{g^4}{3^2\,2^7\,(2\pi)^4}\,x_W^2 &\int_0^1 dy\,\frac{1 + 17y^3 - 9y^2 - 9y - (6y^3 + 18y^2)\ln(y)}{(y\,x_W - 1)^2 + \left(\frac{\Gamma_W}{m_W}\right)^2}. \end{aligned} \tag{4.19}$$

In Fig. 4.4 we plot the integrand of Eq. (4.19) versus $y = Q^2/s$, for the values $x_W \equiv s/m_W^2 = 0.9$, 1.0. 1.1, 1.5, 2.0, and 5.0. The figure reveals that, for $x_W \gtrsim 1.5$, i.e, for $m_\chi \sim \sqrt{s}/2 \gtrsim 0.6 m_W$, the rate $\Gamma(\to \nu_e\bar{\nu}_e e^+ e^-)$ is dominated by the on-shell W-resonance. (Apparently, the q^{-4} pole in Eq. (4.13) is effectively negated by the

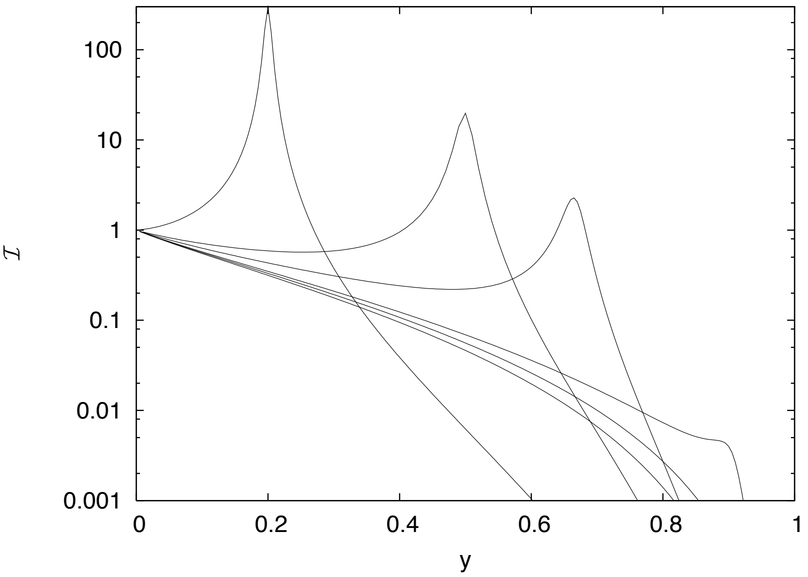

Figure 4.4: Integrand of Eq. 4.19 versus $y = Q^2/s$; in ascending order of the curves, the values of $x_W = s/m_W^2$ are 0.9, 1.0, 1.1, 1.5, 2.0, and 5.0.

vanishing of massless three-body phase space for $\nu\, e^+e^-$ at $q^2 = 0$.) Thus, we are justified in using the narrow width approximation (NWA) for the W-propagator

$$\frac{1}{(Q^2 - M^2) + (M\Gamma)^2} \to \frac{\pi}{M\Gamma}\, \delta(Q^2 - M^2). \tag{4.20}$$

With this approximation, the cross section factorizes into the on-shell production and subsequent decay of the W boson, and the contribution from virtual (off-shell) W bosons is neglected. Using the NWA approximation, the integral in Eq. (4.19) is easily evaluated. The resulting ratio of widths becomes

$$\begin{aligned} R_W &\equiv \frac{\Gamma(\to \overset{(-)}{\nu}\, l^{\pm} W^{\mp} \to \text{All})}{\Gamma(\to \nu\bar{\nu})} \\ &= (2 \times 9) \times \frac{g^4}{3^2\, 2^8\, (2\pi)^3} \frac{m_W}{\Gamma_W} x_W \\ &\times \left[1 + \frac{17}{x_W^3} - \frac{9}{x_W^2} - \frac{9}{x_W} + \left(\frac{6}{x_W^3} + \frac{18}{x_W^2} \right) \ln(x_W) \right]. \end{aligned} \tag{4.21}$$

Here we have dropped the flavor subscript on the (anti)neutrinos since this ratio remains the same when flavors are summed, and multiplied by a prefactor of 2 × 9, which we now explain. The "2" comes from adding the W^--strahlung channel to the W^+ channel. Note that the two amplitudes do not interfere since the charges of the produced W's, and therefore of the pairs they produce with invariant mass $M \sim m_W$, are distinguishable. The "9" comes from summing over all decay channels available to the decaying W. We have three leptonic channels, and two quark flavor channels, the latter multiplied by three for color channels.

We may also evaluate the W-width. At the level of our calculation, we have for this quantity

$$\Gamma_W = (9) \times \frac{g^2}{48\pi} m_W \, . \tag{4.22}$$

The "9" here is the same final state count that appeared in Eq. (4.21). Inputting this width into Eq. (4.21) and using $g^2 = 4\pi\alpha/\sin^2\theta_w$, we arrive at our final expression,

$$\begin{aligned} R_W &= \left(\frac{\alpha}{4\pi\sin^2\theta_w}\right)\left(\frac{x_W}{12}\right) \\ &\times \left[1 + \frac{17}{x_W^3} - \frac{9}{x_W^2} - \frac{9}{x_W} + \left(\frac{6}{x_W^3} + \frac{18}{x_W^2}\right)\ln(x_W)\right] . \end{aligned} \tag{4.23}$$

We note that this expression may also be obtained by directly computing the production of real (on-shell) gauge bosons.

For our numerical work, we will take $\sin^2\theta_w = 0.231$ ($\sin^{-2}\theta_w = 4.33$), and $\alpha = 1/128$ as appropriate for physics at the electroweak scale. This latter choice is especially appropriate in light of the accuracy of the NWA; q^2 of the virtual neutrino will itself have a value near the threshold for on-shell W production, i.e., at $\sim m_W^2$.

4.3 Z-strahlung

The cross section for the Z-strahlung process, $\chi\chi \to \bar{\nu}\nu Z^* \to$ All, may be calculated similarly to that for W-strahlung. For a scalar coupling as assumed in Fig. 4.2, there is no interference between diagrams in which the Z is radiated by the ν and $\bar{\nu}$. Thus the cross section for the Z channel is simply obtained from that for the W channel given in Eq. (4.23) by dividing by a factor of $2\cos^2\theta_W \sim 1.54$, and replacing x_W with $x_Z \equiv s/m_Z^2$, viz.

$$R_Z(x_Z) = \frac{1}{2\cos^2\theta_W} R_W(x_Z) \, . \tag{4.24}$$

Note that the e^+e^-Z coupling differs from the $\bar{\nu}\nu Z$ coupling, such that there is interference between the two contributing diagrams. Here we are interested in a toy model with annihilation to a neutrino pair only at the two-body level, so we do not calculate these interference terms.

4.4 Discussion

Figure 4.5 shows the ratios R_W and R_Z as functions of m_χ. We choose to plot rates versus m_χ rather than x_W and x_Z to make the presentation more physical, and to better illustrate the difference between the W and Z rates. To convert from the scaling variables to m_χ, we have used the expressions $x_G = s/m_G^2 \approx 4\,(m_\chi^2/m_G^2)$, $G = W, Z$, appropriate for non-relativistic dark matter. The curve for R_Z may be directly compared to the points from [82], which we show. Qualitative but not quantitative agreement is evident. Our results agree with the later results from [83].

Let us discuss some general features of R_G, $G = W, Z$. At large $s \gg m_G^2$, we expect a leading term linear in the dimensionless variable $x_G = s/m_G^2$. The factor of s arises from the ratio of 3-body to 2-body phase space, while the numerator is provided by the only other dimensionful quantity in the process. From Fig. 4.5, we see that the leading linear term indeed dominates above $x_G \sim 10$, which corresponds to $m_\chi \gtrsim 1.5\,m_G$. Thus, we may write a very simple expression for the width ratio at $x_G \gtrsim 10$. It is

$$R_W = \left(\frac{\alpha}{4\pi \sin^2\theta_w}\right)\left(\frac{x_W}{12}\right), \quad \text{for } x_W \gtrsim 10\,, \tag{4.25}$$

and likewise times $(2\cos^2\theta_W)^{-1}$ for R_Z. It is unsurprising that the inequality $s \gtrsim 10\,m_G^2 \Leftrightarrow m_\chi \gtrsim 1.5\,m_G$ has appeared twice, earlier to put the W or Z on-shell, and here to impose the dominance of the leading term in the expression for W- or Z-strahlung process.

In the very large s (or equivalently, the very large m_χ) limit, the branching ratio for multi W/Z production will become sizeable. We may estimate the onset of

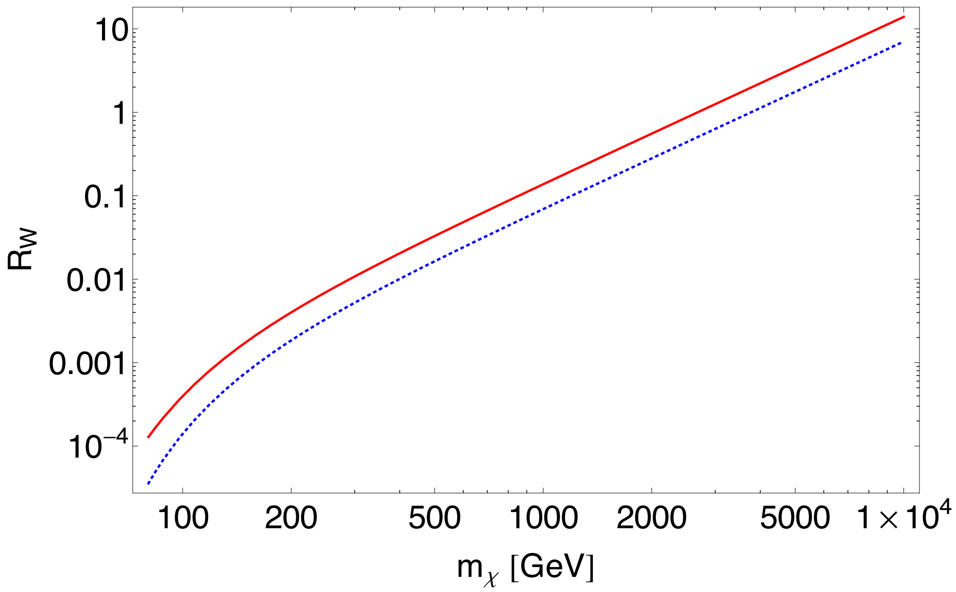

Figure 4.5: The ratios of rates for W-strahlung (solid red) and Z-strahlung (dotted blue) to $\nu\bar{\nu}$ production are plotted versus the dark matter mass m_χ. Evident is the the dominance of the leading linear term in Eq. 4.21 above $x_G \sim 10$. Extrapolations beyond $m_\chi \sim$ TeV hold some uncertainty due to multiple bremsstrahlung, to possible yet unknown new physics, and eventually to re-summation of infrared near-singularities.

double-W/Z production. The general formula for n-body massless phase space is

$$LIPS^{(n)} = \frac{1}{8\pi}\left(\frac{s}{16\pi^2}\right)^{n-2}\frac{1}{(n-1)!\,(n-2)!}\,. \tag{4.26}$$

Neglecting combinatoric factors, the perturbative expansion parameter for additional W/Z bosons is then $(\frac{g}{\sqrt{2}})^2\,\frac{x_G}{16\pi^2} \sim \alpha\, m_\chi^2/m_G^2$. Thus, perturbation theory becomes unreliable and multiple W/Z production occurs when $x_G \sim 2\pi/\alpha$, or $m_\chi \sim \alpha^{-1/2}\, m_G \sim$ TeV. Resummations in the very large s regime, involving ordered $\ln^2(x_G)$ terms from emission of (nearly) massless or collinear W/Z's, are discussed in [195]. Co-emission of a hard photon will also occur, at a rate comparable to double W/Z emission [1].

---

[1] While unitarity of the DM annihilation cross-section does not directly impact the results in this

Finally, we note that our results are easily applied to the DM decay process $\chi \to \nu\bar{\nu}$, where χ is now a boson, with $x_G = s/m_G^2 \to m_\chi^2/m_G^2$. Indeed, similar expressions will hold for any neutrino production mechanism in which the invariant mass of the $\bar{\nu}\nu$ exceeds m_W.

4.5 Conclusions

The decay of W and Z bosons produced via electroweak bremsstrahlung will lead to neutral pions and thus photons. One may constrain this DM annihilation signal by considering its contribution to the Galactic or extragalactic diffuse gamma ray background. This was considered in Refs. [82, 83], where it was shown that the contribution of the process $\sigma(\chi\chi \to \bar{\nu}\nu Z)$ to the galactic gamma ray background imposed limits on the lowest order process, $\sigma(\chi\chi \to \bar{\nu}\nu)$, comparable to those obtained directly with neutrinos. The branching ratio expressions we have derived differ quantitatively, through not qualitatively, from the cross-section estimates in Ref. [82], and agree with those in Ref. [83]. Thus, our results lead to similar bounds. Future analysis of Galactic gamma ray observations, such as those made by Fermi, have the potential to somewhat reduce the diffuse backgrounds through better point source identification, and to measure the background more precisely. In turn, this will strengthen the electromagnetic constraint on DM annihilation, and increase the utility of the quantitative results we have presented herein.

---

paper, we remind the reader of the unitarity constraints presented in Section 1.3.1. In terms of the spinless B exchange model assumed in this work, the unitarity constraint becomes (for $m_B^2 \gg m_\chi^2$) $\left(\frac{m_\chi}{M_B}\right)^2 \left(\frac{\Gamma(B\to\chi\chi)}{M_B}\right) \left(\frac{\Gamma(B\to\mathrm{SM})}{M_B}\right) \leq 1$, where SM refers to Standard Model final states. There is no unitarity constraint on a decay width, a remark relevant for the case where DM decay dominates DM annihilation.

5

Electroweak Bremsstrahlung and the Lifting of Helicity Suppression

5.1 Introduction

The dark matter annihilation cross section is often parametrized as $\langle v\sigma\rangle = a + bv^2 + \mathcal{O}(v^4)$, where $\langle v\sigma\rangle$ is the thermally-averaged annihilation cross section. The constant a comes from s-wave annihilation, while the velocity suppressed bv^2 term receives both s-wave and p-wave contributions; the L^{th} partial wave contribution to the annihilation rate is suppressed as v^{2L}. Given that $v \sim 10^{-3}c$ in galactic halos, even the p-wave contribution is highly suppressed and thus only the s-wave contribution is expected to be significant in the Universe today. However, in many DM models the s-wave annihilation into a fermion pair $\chi\chi \to \bar{f}f$ is helicity suppressed by a factor $(m_f/m_\chi)^2$ (only $\to \bar{t}t$ modes remain of interest, and then only for a certain range of χ mass).

When computing DM annihilation signals, it is normally assumed that only the lowest order tree-level processes make a significant contribution. However, there are important exceptions to this statement. As we have seen in Chapter 3, dark matter annihilation into charged particles, $\chi\chi \to \bar{f}f$, is necessarily accompanied by the internal bremsstrahlung process $\chi\chi \to \bar{f} f \gamma$, where the photon may be radiated from one of the external particle legs (final state radiation, FSR) or, possibly, from a virtual propagator (virtual internal bremsstrahlung, VIB). On the face of it, the radiative rate is down by the usual QED coupling factor of $\alpha/\pi \sim 500$. However, and significantly, photon bremsstrahlung can lift the helicity suppression of the s-wave process [192, 193, 194, 199, 200, 201] (see also Section 1.5), which more than compensates for the extra coupling factor. Such a striking enhancement can arise when a symmetry of the initial state $\chi\chi$ is satisfied by the three body final state $\bar{f} f \gamma$, but not by the two body final state $\bar{f} f$.

In this Chapter we again examine electroweak bremsstrahlung of Z or $W^{\pm}$ gauge bosons to produce $\bar{f} f Z$ and $\bar{\ell}\nu W$ final states, and show that this can also lift suppression (see also [198]). In these scenarios for which the helicity suppression is removed, the dominant annihilation channels are the set of bremsstrahlung processes, namely γ, W and Z bremsstrahlung. (If the dark matter annihilates to colored fermions, radiation of gluons would also contribute). The phenomenology of W and Z bremsstrahlung is richer than that for photon bremsstrahlung alone. This is because the W and Z bosons decay dominantly to hadronic final states, including antiprotons, offering correlated “multi-messenger” signals. This is an important result for future DM searches.

DM annihilation to charged leptons has been the subject of much recent attention, due to recently measured cosmic ray anomalies which point to an excess of cosmic ray positrons above those that may be attributed to conventional astrophysical processes. The positron excess and possible interpretations are discussed in detail in Section 1.3.6. To recap, PAMELA has observed a sharp excess in the $e^+/(e^- + e^+)$ fraction at energies beyond approximately 10 GeV [126], without a corresponding excess in the antiproton/proton data [127, 270], while Fermi and HESS have reported more modest excesses in the $(e^- + e^+)$ flux at energies of order 1 TeV [125]. These signals have led to a re-examination of positron production in nearby pulsars [136, 137, 138, 135, 139, 140, 146, 141, 142], emission from supernova remnants [130, 131], acceleration of e^+e^- in cosmic ray sources [143, 144, 145], and propagation in conventional cosmic ray models [147, 148, 149]. As an alternative to these astrophysical mechanisms, it has also been proposed that the excess e^+ and e^- are produced via dark matter annihilation in the Galactic halo, with an abundance of DM models proposed to accomplish this end. An overview of $e^\pm$-excess data and possible interpretations is available in [152].

However, some of the most popular models suffer from helicity or v^2-suppression. A prototypical example of suppressed production of Standard Model (SM) fermion pairs is provided by supersymmetry: Majorana neutralinos annihilate into a pair of SM fermions via t- and u-channel exchange of $SU(2)$-doublet sfermions. To overcome the suppression, proponents of these models have invoked large "boost" factors. These boost factors may be astrophysical in origin, as with postulated local over-densities of dark matter, or they may arise from particle physics, as with the Sommerfeld enhancement that arises from light scalar exchange between dark matter particles. Although not ruled out, these factors do seem to be a contrivance designed to overcome the innate suppression.

A further problem with suppressed models is the overproduction of antiprotons from unsuppressed W/Z bremsstrahlung. Given that hadronic decay modes of the W and Z bosons will lead to significant numbers of both antiprotons and gamma rays, this will impact the viability of models that might otherwise have explained the observed positron excess. Even in models which do not feature a suppression, bremsstrahlung has important phenomenological consequences, as the primary gamma rays and decay products of the gauge bosons make a pure leptonic e^+e^- signal impossible [83].

In Section 5.2 we discuss the circumstances under which dark matter annihilation may be suppressed. In Section 5.3 we consider a representative model, and explicitly calculate the cross sections for both the lowest order annihilation process, and for the

W/Z bremsstrahlung process. We discuss implications of these results in Section 5.4.

5.2 Understanding Suppression using Fierz Transformations

5.2.1 Utility of Fierz Transformations

Fierz transformations are a valuable tool that allow us to assess the rate of the $2 \to 2$ process $\chi\chi \to e^+e^-$ on general grounds. Given a model with t/u channel annihilation, the Fierz matrix transforms the amplitude into an s-channel-like sum of *initial state currents* times *final state currents*. In general,

$$(\Gamma_1)_a^b(\Gamma_2)_c^d = \frac{1}{4}\sum_A \Delta_A(\gamma_A)_c^b(\Gamma_1\gamma_A\Gamma_2)_a^d, \tag{5.1}$$

where γ_A are the 16 basis Dirac gamma matrices listed in Table 5.1, and Γ_1, Γ_2 are some combination of Dirac gamma matrices. Multiplying by spinors $\bar{l}^a$, χ_b, $\overline{\chi}^c$, l_d, we can see how a t- or u-channel current for DM annihilation to a lepton pair can be expressed as a sum of s-channel currents,

$$(\bar{l}\Gamma_1\chi)(\overline{\chi}\Gamma_2 l) = \frac{1}{4}\Sigma_A\Delta_A(\overline{\chi}\gamma_A\chi)(\bar{l}\Gamma_1\gamma_A\Gamma_2 l), \tag{5.2}$$

where Δ_A is a constant, given in Table 5.1 for all possible values of A. A full derivation and explanation of the Fierz transformation is given in Appendix B. There we re-derive the standard Fierz transformation matrix, and then derive a Fierz transformation matrix for chiral fields. In addition, and importantly, we present "higher-order" formulas for Fierz transforming fermion currents which radiate bosons.

Helicity projection operators are essential in chiral gauge theories, so it is worth considering the reformulation of Fierz transformations in the chiral basis [271]. (A discussion of standard Fierz transformations may be found in, e.g. Ref. [272].) We place hats above the generalized Dirac matrices constituting the chiral basis. These

Table 5.1: Gamma Matrices

A	γ_A	Δ_A
1	$\mathbb{1}$	+1
2,3,4,5	$\gamma_{0,1,2,3}$	+1,-1,-1,-1
6,7,8,9,10,11	$\sigma_{10,20,30,12,23,31}$	+1,+1,+1,-1,-1,-1
12,13,14,15	$\gamma^5\gamma_{0,1,2,3}$	-1,+1,+1,+1
16	γ^5	+1

matrices are

$$\begin{aligned}\{\hat{\Gamma}^B\} &= \{P_R,\, P_L,\, P_R\gamma^\mu,\, P_L\gamma^\mu,\, \frac{1}{2}\sigma^{\mu\nu}\}\,, \quad \text{and}\\ \{\hat{\Gamma}_B\} &= \{P_R,\, P_L,\, P_L\gamma_\mu,\, P_R\gamma_\mu,\, \frac{1}{2}\,\sigma_{\mu\nu}\}\,,\end{aligned} \tag{5.3}$$

where $P_R \equiv \frac{1}{2}(1+\gamma_5)$ and $P_L \equiv \frac{1}{2}(1-\gamma_5)$ are the usual helicity projectors. Notice that the dual of $P_R\gamma^\mu$ is $P_L\gamma_\mu$, and the dual of $P_L\gamma^\mu$ is $P_R\gamma_\mu$. The tensor matrices in this basis contain factors of $\frac{1}{2}$: $\hat{\Gamma}^T = \frac{1}{2}\sigma^{\mu\nu}$ and $\hat{\Gamma}_T = \frac{1}{2}\sigma_{\mu\nu}$. These facts result from the orthogonality and normalization properties of the chiral basis and its dual, as explained in detail in Appendix B.

Using completeness of the basis (see Appendix B), one arrives at a master formula which expands the outer product of two chiral matrices in terms of their Fierzed forms:

$$(\hat{\Gamma}^D)\,[\hat{\Gamma}_E] = \frac{1}{4}\,Tr\,[\hat{\Gamma}^D\,\hat{\Gamma}^C\,\hat{\Gamma}_E\,\hat{\Gamma}_B]\;(\hat{\Gamma}^B]\;[\hat{\Gamma}_C)\,, \tag{5.4}$$

where the parentheses symbols are a convenient shorthand for matrix indices [273] (see Appendix B for details). Evaluating the trace in Eq. 5.4 leads to the Fierz transformation matrix in the chiral-basis:

$$\begin{pmatrix} (P_R)\,[P_R] \\ (P_L)\,[P_L] \\ (\hat{T})\,[\hat{T}] \\ (\gamma_5\,\hat{T})\,[\hat{T}] \\ (P_R)\,[P_L] \\ (P_R\gamma^\mu)\,[P_L\gamma_\mu] \\ (P_L)\,[P_R] \\ (P_L\gamma^\mu)\,[P_R\gamma_\mu] \\ (P_R\gamma^\mu)\,[P_R\gamma_\mu] \\ (P_L\gamma^\mu)\,[P_L\gamma_\mu] \end{pmatrix} = \frac{1}{4} \left(\begin{array}{cccc|cc|cc|c|c} 2 & 0 & 1 & 1 & & & & & & \\ 0 & 2 & 1 & -1 & & & & & & \\ 6 & 6 & -2 & 0 & & & & & & \\ 6 & -6 & 0 & 2 & & & & & & \\ \hline & & & & 0 & 2 & & & & \\ & & & & 8 & 0 & & & & \\ \hline & & & & & & 0 & 2 & & \\ & & & & & & 8 & 0 & & \\ \hline & & & & & & & & -4 & 0 \\ \hline & & & & & & & & 0 & -4 \end{array}\right) \begin{pmatrix} (P_R]\,[P_R) \\ (P_L]\,[P_L) \\ (\hat{T}]\,[\hat{T}) \\ (\gamma_5\,\hat{T}]\,[\hat{T}) \\ (P_R]\,[P_L) \\ (P_R\gamma^\mu]\,[P_L\gamma_\mu) \\ (P_L]\,[P_R) \\ (P_L\gamma^\mu]\,[P_R\gamma_\mu) \\ (P_R\gamma^\mu]\,[P_R\gamma_\mu) \\ (P_L\gamma^\mu]\,[P_L\gamma_\mu) \end{pmatrix} . \tag{5.5}$$

Non-explicit matrix elements in Eq. 5.5 are zero, and we have introduced a shorthand $\hat{T}$ for either $\hat{\Gamma}^T = \frac{1}{2}\sigma^{\mu\nu}$ or $\hat{\Gamma}_T = \frac{1}{2}\sigma_{\mu\nu}$.

The importance of this transformation for us is that it converts t-channel and u-channel exchange graphs into s-channel form, for which it is straightforward to evaluate the partial waves. The block-diagonal structures, delineated with horizontal and vertical lines, show that "mixing" occurs only within the subsets $\{P_R \otimes P_R,\ P_L \otimes P_L,\ \hat{T} \otimes \hat{T},\ \gamma_5\,\hat{T} \otimes \hat{T}\}$, and $\{P_R \otimes P_L,\ P_R\gamma^\mu \otimes P_L\gamma_\mu\}$. The Fierz transform matrix is idempotent, meaning its square is equal to the identity matrix. This follows from the fact that two Fierz rearrangements return the process to its initial ordering. A consequence of the block-diagonal form is that each sub-block is itself idempotent.

In Eq. 5.5 we have included one non-member of the basis set, namely $\gamma_5\,\hat{T}$; it is connected to $\hat{T}$ via the relation

$$\gamma_5\,\sigma^{\mu\nu} = \frac{i}{2}\epsilon^{\mu\nu\alpha\beta}\sigma_{\alpha\beta}\,. \tag{5.6}$$

Explicit use of $\gamma_5\,\hat{T}$ in Eq. 5.5 is an efficient way to express the chiral Fierz transformation.

5.2.2 Origin of Suppression

One can use partial wave decomposition (see. e.g., the textbooks [267, 274, 275], or the convenient summary in the Appendix of [84]) to expand the scattering amplitudes as a sum of angular momentum components. Partial waves do not interfere, and the L^{th} partial wave contribution to the total cross section $v\sigma$ is proportional to v^{2L}. The annihilating χ particles are very non-relativistic today, so an unsuppressed s-wave ($L = 0$), if present, will dominate the annihilation cross section. The DM virial velocity within our Galaxy is about 10^{-3} (in units of c), leading to a suppression of $v^2 \sim 10^{-6}$ for p-wave processes.

On the other hand, the SM fermions produced in the $2 \to 2$ annihilation are highly relativistic (except possibly for $t\bar{t}$ production). For many annihilation channels the spin state of the fermion pair gives rise to a helicity suppression by a factor of $(m_l/m_\chi)^2$, where m_l is the fermion mass.

Unfortunately, many popular models for annihilation of Majorana dark matter to charged leptons are subject to one or more of these two suppressions, the v^2 and/or $(m_\ell/m_\chi)^2$ suppressions. This includes some of the models proposed to accommodate the positron and e^+e^- excesses observed in PAMELA, Fermi-LAT, and HESS data. In Section 5.3, we show that in the class of models which have suppressed rates for $\chi\chi \to \ell^+\ell^-$, the $2 \to 3$ graph obtained by adding a radiative $W^\pm$ or Z to the final state particles of the $2 \to 2$ graph can become unsuppressed, just as with emission of a photon. The radiated W's and Z's will decay to, among other particles, antiprotons. The consequences of this are discussed in Chapter 6.

5.2.3 Models with v^2 and Helicity Suppression

Consider products of s-channel bilinears of the form $(\overline{\chi}\ \Gamma_1\chi)(\bar{l}\ \Gamma_2 l)$. To further address the question of which products of currents are suppressed and which are not, we may set v^2 to zero in the χ-current (appropriate for annihilation of non-relativistic DM), and m_ℓ^2 to zero in the lepton current (appropriate for the production of highly relativistic fermions), and ask whether the product of currents is suppressed. If the product of currents is non-zero in this limit, the corresponding amplitude is unsuppressed. In Table 5.2 we give the results for the product of all standard Dirac

s-channel bilinear $\bar{\Psi}\,\Gamma_D\,\Psi$		$v = 0$ limit		$M = 0$ limit	
		parallel spinors	antiparallel spinors	parallel spinors	antiparallel spinors
scalar	$\bar{\Psi}\,\Psi$	0	0	$\sqrt{s}$	0
pseudo-scalar	$\bar{\Psi}\,i\gamma_5\,\Psi$	$-2iM$	0	$-i\sqrt{s}$	0
axial-vector	$\bar{\Psi}\,\gamma_5\,\gamma^0\,\Psi$	$2M$	0	0	0
	$\bar{\Psi}\,\gamma_5\,\gamma^j\,\Psi$	0	0	0	$\sqrt{s}\,(\pm\delta_{j1} - i\delta_{j2})$
vector	$\bar{\Psi}\,\gamma^0\,\Psi$	0	0	0	0
	$\bar{\Psi}\,\gamma^j\,\Psi$	$\mp 2M\,\delta_{j3}$	$-2M\,(\delta_{j1} \mp i\delta_{j2})$	0	$-\sqrt{s}\,(\delta_{j1} \mp i\delta_{j2})$
tensor	$\bar{\Psi}\,\sigma^{0j}\,\Psi$	$\mp 2iM\,\delta_{j3}$	$-2iM\,(\delta_{j1} \pm \delta_{j2})$	$-i\sqrt{s}\,\delta_{j3}$	0
	$\bar{\Psi}\,\sigma^{jk}\,\Psi$	0	0	$\pm\sqrt{s}\,\delta_{j1}\delta_{k2}$	0
pseudo-tensor	$\bar{\Psi}\,\gamma_5\,\sigma^{0j}\,\Psi$	0	0	$\pm i\sqrt{s}\,\delta_{j3}$	0
	$\bar{\Psi}\,\gamma_5\,\sigma^{jk}\,\Psi$	$\mp 2M\,\delta_{j1}\delta_{k2}$	$-2M\,(\delta_{j2}\delta_{k3} \mp i\delta_{j3}\delta_{k1})$	$-\sqrt{s}\,\delta_{j1}\delta_{k2}$	0

Table 5.2: Extreme non-relativistic and extreme relativistic limits for s-channel bilinears. In order for a term with an initial-state DM bilinear and a final-state lepton bilinear to remain unsuppressed, the DM bilinear must have a non-zero entry in the appropriate cell of the "$v = 0$ limit" columns, and the lepton bilinear must have a non-zero term in the appropriate cell of the "$M = 0$ limit" columns. Otherwise, the term is suppressed. (The tensor and pseudo-tensor are not independent, but rather are related by $\gamma_5\,\sigma^{\mu\nu} = \frac{i}{2}\epsilon^{\mu\nu\alpha\beta}\,\sigma_{\alpha\beta}$.) We recall that antiparallel spinors correspond to parallel particle spins (and antiparallel particle helicities for the $M = 0$ current), and vice versa. Amplitudes are shown for $\overline{u}\,\Gamma_D\,v = [\overline{v}\,\Gamma_D\,u]^*$. The two-fold ± ambiguities reflect the two-fold spin assignments for parallel spins, and separately for antiparallel spins.

bilinears. (The derivation of these results is outlined in Appendix C.) Suppressed bilinears enter this table as zeroes. [1]

One can read across rows of this table to discover that the only unsuppressed s-channel products of bilinears for the $2 \rightarrow 2$ process are those of the pseudo-scalar, vector, and tensor. (For completeness, we also show results for the pseudo-tensor bilinears, although the pseudo-tensor is not independent of the tensor, as a result of Eq. 5.6.) As a test of these results, we have calculated the cross sections for s-channel scalar, pseudo-scalar and axial-vector annihilation processes in Appendix D, and find they are consistent with the results in Table 5.2.

For t-channel and u-channel annihilation processes, one may simply use a Fierz transform to convert the amplitudes to s-channel form, and then apply logic similar to that given above. Any t-channel or u-channel diagram that Fierz's to an s-channel form containing a pseudoscalar coupling will have an unsuppressed $L = 0$ s-wave amplitude. From the matrix in Eqn. 5.5, one deduces that such will be the case for any t- or u-channel current product on the left side which finds a contribution in the 1^{st}, 2^{nd}, 5^{th}, or 7^{th} columns of the right side. This constitutes the t- or u-channel tensor, same-chirality scalar, and opposite chirality vector products (rows 1 through 4, and 6 and 8 on the left). On the other hand, the t- or u-channel opposite chirality scalars or same-chirality vectors (rows 5, 7, 9, and 10 on the left) do *not* contain a pseudoscalar coupling after Fierzing to s-channel form. Rather, it is the suppressed axial-vector and vector that appears.

For Majorana dark matter, the vector and tensor bilinears are disallowed by charge-conjugation arguments (See Appendix A). The proscription is absolute in the four-Fermi limit where u- and t-channel propagators are identical. More generally,

---

[1] It is seen that the only bilinears in the table without velocity-suppression are those of the pseudo-scalar, the three-vector part of the vector, the zero$^{\text{th}}$ component of the axial vector, and the time-space part of the tensor (or equivalently, the space-space part of the pseudotensor). It is also seen that the only bilinears without fermion mass-suppression are the scalar, pseudoscalar, three-vector parts of the vector and axial vector, and the tensor.

when u and t are not negligible compared to the mass of the exchanged particle, the cancellation between u- and t- channel graphs is incomplete, and the vector and tensor couplings are suppressed but not forbidden.

Interestingly, a class of the most popular models for fermionic dark matter annihilation to charged leptons, fall into this latter, suppressed, category. It is precisely the opposite-chirality t- or u-channel scalar exchange that appears in these models, an explicit example of which will be discussed below. Thus it is rows 5 and 7 in Eqn. 5.5 that categorize the model we will analyze. After Fierzing to s-channel form, it is seen that the Dirac bilinears are opposite-chirality vectors (i.e., V or A). Dropping the vector term from the χ-current we see that the $2 \to 2$ process couples an axial vector χ-current to a relativistic SM fermion-current which is an equal mixture of A and V. Accordingly, this model has an s-wave amplitude occurring only in the $L = 0$, $J = 1$, $S = 1$ channel, with the spin flip from $S = 0$ to $S = 1$ (or equivalently, the mismatch between zero net chirality and one unit of helicity) costing a fermion mass-insertion and a $(m_f/m_\chi)^2$ suppression in the rate.

Let us pause to explain why this t- or u-channel scalar exchange with opposite fermion chiralities at the vertices is so common. It follows from a single popular assumption, namely that the dark matter is a gauge-singlet Majorana fermion. As a consequence of this assumption, annihilation to SM fermions, which are $SU(2)$ doublets or singlets, requires either an s-channel singlet boson or a t- or u-channel singlet or doublet scalar that couples to χ-f. In the first instance, there is no symmetry to forbid a new force between SM fermions, a disfavored possibility. In the second instance, unitarity fixes the second vertex as the hermitian adjoint of the first. Since the fermions of the SM are left-chiral doublets and right-chiral singlets, one gets chiral-opposites for the two vertices of the t- or u-channel.

Supersymmetry provides an analog of such a model. In this case the dark matter consists of Majorana neutralinos, which annihilate to SM fermions via the exchange of (“right”- and “left”-handed) $SU(2)$-doublet slepton fields. In fact, the implementation in 1983 of supersymmetric photinos as dark matter provided the first explicit calculation of s-wave suppressed Majorana dark matter [276, 277].[2] However, the class of models described above is more general than the class of supersymmetric models.

5.2.4 Example of suppressed annihilation

To illustrate our arguments, we choose a simple example of the class of model under discussion. This is provided by the leptophilic model proposed in Ref. [86] by Cao, Ma and Shaughnessy. Here the DM consists of a gauge-singlet Majorana fermion χ which annihilates to leptons via the $SU(2)$-invariant interaction term

$$f\left(\nu\,\ell^-\right)_L\,\varepsilon\begin{pmatrix}\eta^+\\ \eta^0\end{pmatrix}\chi + h.c. = f(\nu_L\eta^0 - \ell_L\eta^+)\chi + h.c. \tag{5.7}$$

where f is a coupling constant, ε is the 2×2 antisymmetric matrix, and $(\eta^+,\,\eta^0)$ form the new $SU(2)$ doublet scalar. In this model, DM annihilation to fermions is mediated by t and u channel exchange of the η fields. (This model was originally discussed in Ref. [279], and an expanded discussion of its cosmology may be found in Ref. [280].)

An identical coupling occurs in supersymmetry if we identify χ with a neutralino and η with a sfermion doublet. Therefore, much of what we discuss below is also relevant for neutralino annihilation to fermions via the exchange of sfermions. However, the class of models for which the $2 \to 2$ annihilation is helicity suppressed is more general than the class of supersymmetric models.

As discussed above, the u- and t-channel amplitudes for DM annihilation to leptons, of the form $(\overline{\chi}P_L l)\,(\bar{l}P_R\chi)$, become pure $(\overline{\chi}P_L\gamma^\mu\chi)\,(\bar{l}P_R\gamma_\mu l)$ under the chiral Fierz transformation. The product of the Majorana and fermion bilinears then leads

---

[2] A detailed calculation of the related amplitude $e^+e^- \to \tilde{\gamma}\tilde{\gamma}$ involving two identical Majorana particles is available in App. E (as well as a lucid and complete presentation of Feynman rules for Majorana fermions in App. D) of Ref. [278]. Another lucid listing of Feynman rules for Majorana fermions is available in Chapter 49 of Ref. [275].

to an AA term and an AV term. However, reference to Table 5.2 shows that neither of these terms leads to an unsuppressed amplitude: in all cases, either the lepton bilinear is suppressed by m_ℓ, the DM bilinear by v, or both are suppressed.

The cross section for the $2 \to 2$ process $\chi\chi \to e^+e^-$ or $\nu\bar{\nu}$ is given by

$$v\,\sigma = \frac{f^4 v^2}{24\pi\, m_\chi^2}\,\frac{1+\mu^2}{(1+\mu)^4}\,, \tag{5.8}$$

where $m_l \simeq 0$ and $m_{\eta^\pm} = m_{\eta^0}$ have been assumed, and $\mu = m_\eta^2/m_\chi^2$. The suppressions discussed above are apparent in Eqn. 5.8. The helicity suppressed s-wave term is absent in the $m_l = 0$ limit, and thus only the v^2-suppressed term remains.

5.3 Lifting the suppression with electroweak bremsstrahlung

Allowing the lepton bilinear to radiate a W or Z boson (as shown in Fig. 5.1) can yield an unsuppressed amplitude, similar to the way in which emission of a photon lifts suppression. In the rate, there will be the usual radiative suppression factor of $\frac{\alpha_2}{4\pi} \sim 10^{-3}$. But, this will be partially compensated by a 3-body phase space factor $\sim (m_\chi/m_W)^2/8\pi^2$ relative to 2-body massless phase space, which exceeds unity for dark matter masses exceeding ~TeV.

More importantly, the v^2 suppression for Majorana annihilation to 2-body final states will be lifted by the 3-body W-bremsstrahlung process. In this section we show, by explicit calculation, that the $2 \to 3$ radiative process that leads to antiprotons dominates when the DM and scalar propagator are near degenerate in mass, for any m_χ that allows the W to be produced on-shell, i.e., $2m_\chi > m_W$.

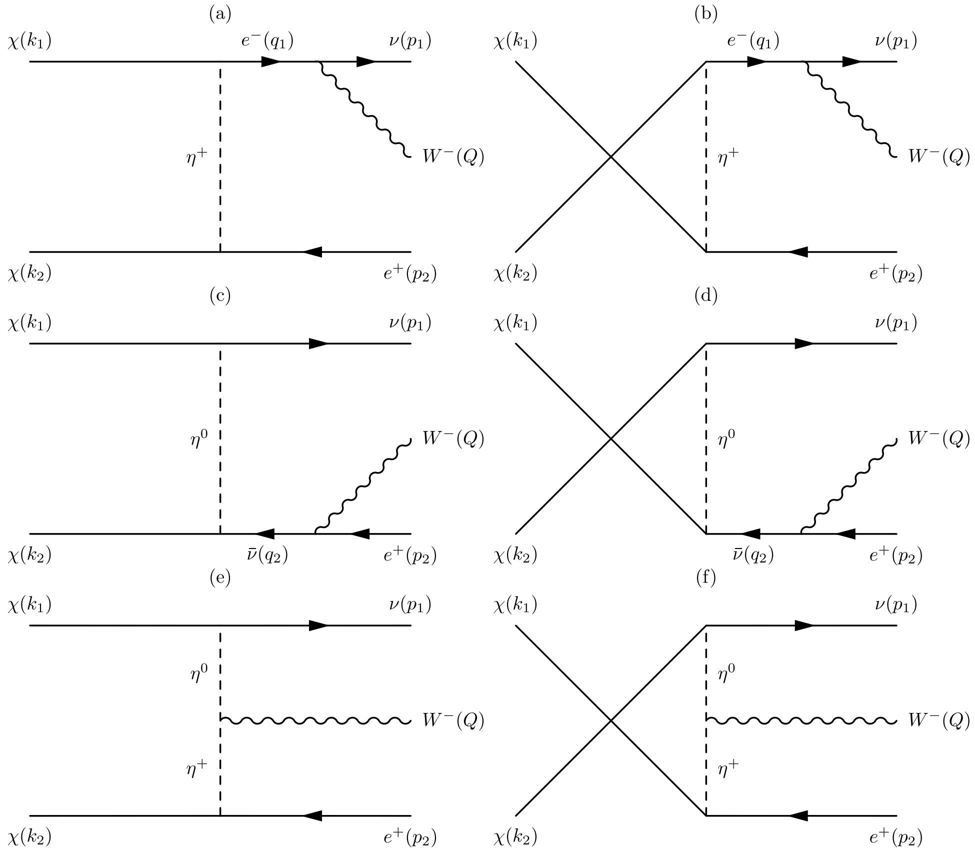

Figure 5.1: The t-channel ((a),(c), and (e)) and u-channel ((b), (d) and (f)) Feynman diagrams for $\chi\chi \to e^+\nu W^-$. Note that t- and u-channel amplitudes are simply related by the $k_1 \leftrightarrow k_2$ interchange symmetry. All fermion momenta in the diagrams flow with the arrow except p_2 and q_2, with $q_1 = p_1 + Q$, $q_2 = p_2 + Q$.

5.3.1 W-strahlung Matrix Elements

We shall take the limit $m_l \simeq 0$ and assume that $m_{\eta^\pm} = m_{\eta^0}$. The matrix elements for the six diagrams of Fig. 5.1 are given by

$$\begin{aligned}\mathcal{M}_a &= i\frac{f^2 g}{\sqrt{2}}\frac{1}{q_1^2}\frac{1}{t_1 - m_\eta^2} \\ &\quad \times(\bar{v}(k_2)P_L v(p_2))(\bar{u}(p_1)\gamma^\mu P_L \not{q}_1 u(k_1))\epsilon_\mu^Q, \qquad (5.9)\\ \mathcal{M}_b &= i\frac{f^2 g}{\sqrt{2}}\frac{1}{q_1^2}\frac{1}{u_1 - m_\eta^2} \\ &\quad \times(\bar{v}(k_1)P_L v(p_2))(\bar{u}(p_1)\gamma^\mu P_L \not{q}_1 u(k_2))\epsilon_\mu^Q, \qquad (5.10)\end{aligned}$$

$$\begin{aligned}
\mathcal{M}_c &= -i\frac{f^2 g}{\sqrt{2}}\frac{1}{q_2^2}\frac{1}{t_2 - m_\eta^2} \\
&\quad \times(\bar{v}(k_2)P_L\not{q}_2\gamma^\mu v(p_2))(\bar{u}(p_1)P_R u(k_1))\epsilon_\mu^Q, \qquad (5.11)\\
\mathcal{M}_d &= -i\frac{f^2 g}{\sqrt{2}}\frac{1}{q_2^2}\frac{1}{u_2 - m_\eta^2} \\
&\quad \times(\bar{v}(k_1)P_L\not{q}_2\gamma^\mu v(p_2))(\bar{u}(p_1)P_R u(k_2))\epsilon_\mu^Q, \qquad (5.12)\\
\mathcal{M}_e &= -i\frac{f^2 g}{\sqrt{2}}\frac{1}{t_1 - m_\eta^2}\frac{1}{t_2 - m_\eta^2} \\
&\quad \times(\bar{v}(k_2)P_L v(p_2))(\bar{u}(p_1)P_R u(k_1)) \\
&\quad \times((k_1 - p_1) + (k_1 - p_1 - Q))^\mu\epsilon_\mu^Q, \qquad (5.13)\\
\mathcal{M}_f &= -i\frac{f^2 g}{\sqrt{2}}\frac{1}{u_1 - m_\eta^2}\frac{1}{u_2 - m_\eta^2} \\
&\quad \times(\bar{v}(k_1)P_L v(p_2))(\bar{u}(p_1)P_R u(k_2)) \\
&\quad \times((k_2 - p_1) + (k_2 - p_1 - Q))^\mu\epsilon_\mu^Q, \qquad (5.14)
\end{aligned}$$

where we define the usual helicity projectors $P_{R/L} \equiv \frac{1}{2}(1 \pm \gamma_5)$, and the Mandelstam variables

$$\begin{aligned}
t_1 &= (k_1 - q_1)^2, \\
t_2 &= (k_1 - p_1)^2, \\
u_1 &= (k_2 - q_1)^2, \\
u_2 &= (k_2 - p_1)^2,
\end{aligned}$$

The vertex factors used in the matrix elements are as follows: the $l\nu W$ vertex has an $\frac{ig}{\sqrt{2}}\gamma^\mu P_L\epsilon_\mu^Q$, the $\chi\eta l$ vertex is ifP_L, and the coupling between the W^- and the $\eta^+ - \eta^0$ is taken to be of the form $-ig(p+p')/\sqrt{2}$ from Fig.72b on p. 221 of Ref. [278].

We have explicitly checked the gauge invariance of our set of Feynman diagrams. Writing the matrix element as

$$\mathcal{M} = \mathcal{M}^\mu\epsilon_\mu^Q, \tag{5.15}$$

the Ward identity

$$Q_\mu\mathcal{M}^\mu = 0, \tag{5.16}$$

is satisfied for the sum of the diagrams. The Ward identity takes the same form as for photon bremsstrahlung provided we take the lepton masses to be zero, since the axial vector current is conserved in this limit. Note that diagrams (a)+(c)+(e) form a gauge invariant subset, as do (b)+(d)+(f). The full amplitude is the sum of the partial amplitudes, properly weighted by a minus sign when two fermions are interchanged. Thus we have $\mathcal{M} = (\mathcal{M}_a + \mathcal{M}_c + \mathcal{M}_e) - (\mathcal{M}_b + \mathcal{M}_d + \mathcal{M}_f)$.

In performing the sum over spins and polarizations, we note the standard polarization sum,

$$\sum_{\text{pol.}} \epsilon^Q_\mu \epsilon^Q_\nu = -\left(g_{\mu\nu} - \frac{Q_\mu Q_\nu}{m_W^2} \right) , \tag{5.17}$$

can be replaced with $-g_{\mu\nu}$ alone. The Ward identity of Eqn. 5.16 ensures the second term in Eqn. 5.17 does not contribute once the contributions from all diagrams are summed (and squared).

In addition, we find that the longitudinal polarization of the W also does not contribute to the s-wave amplitude, i.e.

$$\mathcal{M}^\mu \epsilon^Q_{L\,\mu} = 0\,. \tag{5.18}$$

The W boson behaves as a massive transverse photon, with just two transverse polarizations contributing. As a consequence, our calculation of W bremsstrahlung must reduce to the known results for photon bremsstrahlung in the $m_W \to 0$ limit, modulo coupling constants. Below we will show that this happens.

5.3.2 Fierz transformed matrix elements

Upon applying Eqn. 5.1 to Fierz transform the matrix elements of Eqns. 5.9–5.14 we find

$$\begin{aligned}
\mathcal{M}_a &= \frac{igf^2}{\sqrt{2}q_1^2}\frac{1}{t_1-m_\eta^2}\frac{1}{2}\Big(\bar{v}(k_2)\gamma_\alpha P_R u(k_1)\Big) \\
&\quad \times\Big(\bar{u}(p_1)\gamma^\mu \not{q}_1\gamma^\alpha P_L v(p_2)\Big)\epsilon_\mu^Q, \qquad (5.19)\\
\mathcal{M}_b &= \frac{igf^2}{\sqrt{2}q_1^2}\frac{1}{u_1-m_\eta^2}\frac{1}{2}\Big(\bar{v}(k_2)\gamma_\alpha P_L u(k_1)\Big) \\
&\quad \times\Big(\bar{u}(p_1)\gamma^\mu \not{q}_1\gamma^\alpha P_L v(p_2)\Big)\epsilon_\mu^Q, \qquad (5.20)\\
\mathcal{M}_c &= \frac{-igf^2}{\sqrt{2}q_2^2}\frac{1}{t_2-m_\eta^2}\frac{1}{2}\Big(\bar{v}(k_2)\gamma_\alpha P_R u(k_1)\Big) \\
&\quad \times\Big(\bar{u}(p_1)\gamma^\alpha \not{q}_2\gamma^\mu P_L v(p_2)\Big)\epsilon_\mu^Q, \qquad (5.21)\\
\mathcal{M}_d &= \frac{-igf^2}{\sqrt{2}q_2^2}\frac{1}{u_2-m_\eta^2}\frac{1}{2}\Big(\bar{v}(k_2)\gamma_\alpha P_L u(k_1)\Big) \\
&\quad \times\Big(\bar{u}(p_1)\gamma^\alpha \not{q}_2\gamma^\mu P_L v(p_2)\Big)\epsilon_\mu^Q, \qquad (5.22)\\
\mathcal{M}_e &= \frac{-igf^2}{2\sqrt{2}}\frac{(2k_1-2p_1-Q)^\mu}{(t_1-m_\eta^2)(t_2-m_\eta^2)}\left(\bar{v}(k_2)\gamma_\alpha P_R u(k_1)\right) \\
&\quad \times\left(\bar{u}(p_1)\gamma^\alpha P_L v(p_2)\right)\epsilon_\mu^Q, \qquad (5.23)\\
\mathcal{M}_f &= \frac{-igf^2}{2\sqrt{2}}\frac{(2k_2-2p_1-Q)^\mu}{(u_1-m_\eta^2)(u_2-m_\eta^2)}\left(\bar{v}(k_2)\gamma_\alpha P_L u(k_1)\right) \\
&\quad \times\left(\bar{u}(p_1)\gamma^\alpha P_L v(p_2)\right)\epsilon_\mu^Q. \qquad (5.24)
\end{aligned}$$

We indeed confirm that Eqns. 5.19–5.24 lead to Eqn. 5.58, the same amplitude squared as we found using the non-Fierzed matrix elements, Eqns. 5.9–5.14. Alternatively, we may apply Eqn. B.20 to transform Eqns. 5.9-5.14. After a bit of algebra we get a pleasant factorized form for the bilinear currents. We show details for the first one, and then summarize the results for current products of the other matrix elements.

The current product in amplitude $\mathcal{M}_a$ of Eqn. 5.9 is

$$\left(\bar{v}(k_2)P_L v(p_2)\right)\Big(\bar{u}(p_1)\not{\epsilon}^Q P_L \not{q}_1 u(k_1)\Big)\,. \tag{5.25}$$

We write this current product in Takahashi notation and then use Eqn. B.20 to get

$$\begin{aligned}[P_L]\,(\not{\epsilon}^Q P_L \not{q}_1) &= \frac{1}{4}\,Tr[P_L \Gamma^C \not{\epsilon}^Q P_L \not{q}_1 \Gamma_B\,]\,(\Gamma^B]\,[\Gamma_C\,) \\ &= \frac{1}{4}\,Tr[P_L \gamma^\alpha \not{\epsilon}^Q P_L \not{q}_1 \gamma_\beta\;(P_R\gamma^\beta]\,[P_L\gamma_\alpha\,)\,.\end{aligned} \tag{5.26}$$

In going from the first equality to the second, we insert the only values for Γ^C and Γ_B allowed by the helicity projectors in the string of gamma matrices. Finally, we may invert the sequence in the trace, and remove the Takahashi notation to write the result as

$$\begin{aligned}\frac{1}{4}\qquad & Tr[P_R \not{\epsilon}^Q P_L \not{q}_1 \gamma_\beta \gamma^\alpha\,]\times \\ & \Big(\bar{u}(p_1) P_R \gamma^\beta v(p_2)\Big)\,(\bar{v}(k_2) P_L \gamma_\alpha u(k_1))\ .\end{aligned} \tag{5.27}$$

Amplitude $\mathcal{M}_b$ is computed in a similar way. In addition, it is useful to use the identity for a Majorana current

$$(\bar{v}(k_1) P_L \gamma_\alpha u(k_2)) = (\bar{v}(k_2) P_R \gamma_\alpha u(k_1)) \quad [\text{Majorana}\,] \tag{5.28}$$

to put the final result in a form similar to that for amplitude $\mathcal{M}_a$.

The other current products are reduced in a similar fashion. The final result for the product of currents after Fierzing is

$$\begin{aligned}\tfrac{1}{4}\quad & (\bar{v}(k_2) P \gamma^\alpha u(k_1))\,\Big(\bar{u}(p_1) P_R \gamma^\beta v(p_2)\Big) \\ \times & \begin{cases} Tr[P_R \not{\epsilon}^Q \not{q}_1 \gamma_\beta \gamma_\alpha\,]\,, & \text{for } \mathcal{M}_a,\ \mathcal{M}_b \\ Tr[P_L \not{\epsilon}^Q \not{q}_2 \gamma_\beta \gamma_\alpha\,]\,, & \text{for } \mathcal{M}_c,\ \mathcal{M}_d \\ 2\,g_{\alpha\beta}\,, & \text{for } \mathcal{M}_e,\ \mathcal{M}_f\,. \end{cases}\end{aligned} \tag{5.29}$$

In addition, the unspecified projector P in the first common factor is P_L for amplitudes $\mathcal{M}_a$, $\mathcal{M}_c$, $\mathcal{M}_e$, and P_R for the amplitudes $\mathcal{M}_b$, $\mathcal{M}_d$, $\mathcal{M}_f$ derived from the crossed graphs.

What can we learn from this exercise? For graphs $\mathcal{M}_e$ and $\mathcal{M}_f$ the Fierzed currents are the same as in the 2 → 2 case. This fact is not surprising since in these graphs the internal W emission does not perturb the form of the currents and their product. However, for the other four graphs with W emission occurring on a fermion leg, the form of the current product is quite different from the $2 \to 2$ case. With $2 \to 3$ scattering, the Lorentz index of each current need not contract directly with the other. Referring to Table 1, one sees that unsuppressed Majorana annihilation amplitudes become possible for the axial vector combination $(\gamma_5\gamma^0\,]\,[\gamma_5\vec{\gamma}_T\,)$, and for the vector combination $(\gamma^3\,]\,[\vec{\gamma}_T\,)$, providing the trace post-factors in Eqn. 5.29 do not vanish. These combinations are at the heart of the unsuppression which we have presented in this paper.

Also, for $m_\eta^2 \gg t$, u, the non-current factors in amplitudes $\mathcal{M}_a$ and $\mathcal{M}_b$ are the same, as are the non-current factors in amplitudes $\mathcal{M}_c$ and $\mathcal{M}_d$. Then the subtraction of one from the other leads to a pure axial vector coupling in the Majorana current. This in term leads to an effectively pure axial vector coupling in the final state lepton current. For values of t and u which are non-negligible when compared to m_η^2, there is some residual vector coupling.

5.3.3 W-strahlung Cross Section

The cross section is given by

$$v\,d\sigma = \frac{1}{2s}\int \frac{1}{4}\sum_{\text{spin, pol.}} |\mathcal{M}|^2\, dLips^3 \tag{5.30}$$

where the $\frac{1}{4}$ arises from averaging over the spins of the initial χ pair, and $v = \sqrt{1-\frac{4m_\chi^2}{s}}$ is the mean dark matter single-particle velocity in the center of mass frame, which is equal to half the relative velocity, $v \equiv \frac{1}{2}v_{\text{rel}}$. (Note that some authors define $v \equiv v_{\text{rel}}$.) Informative discussions of the meaning of v are given in [281], and, including thermal averaging, in Section 1.1.5.

The three-body Lorentz Invariant Phase Space is

$$dLips^3 = (2\pi)^4 \frac{d^3\vec{p}_1}{2E_1}\frac{d^3\vec{p}_2}{2E_2}\frac{d^3\vec{Q}}{2E_W}\frac{\delta^4(P-p_1-p_2-Q)}{(2\pi)^9} \tag{5.31}$$

and $P = k_1 + k_2$. This factorizes into the product of two two-body phase space integrals, convolved with an integral over the fermion propagator momentum,

$$\begin{aligned} dLips^3 &= \int_{m_W^2}^{s} \frac{dq_1^2}{2\pi} \left(\frac{d^3\vec{q}_1}{2E_{q_1}} \frac{d^3\vec{p}_2}{2E_2} \frac{\delta^4(P - q_1 - p_2)}{(2\pi)^2} \right) \\ &\quad \times \left(\frac{d^3\vec{p}_1}{2E_1} \frac{d^3\vec{Q}}{2E_W} \frac{\delta^4(q_1 - Q - p_1)}{(2\pi)^2} \right) \\ &= \int_{m_W^2}^{s} \frac{dq_1^2}{2\pi}\, dLips^2(P^2, q_1^2, p_2^2)\, dLips^2(q_1^2, Q^2, p_1^2). \end{aligned} \tag{5.32}$$

Evaluating the two-body phase space factors in their respective center of momentum frames, and using $p_1^2 = p_2^2 = 0$, we have

$$dLips^2(x^2, y^2, 0) = \frac{x^2 - y^2}{8\pi x^2} \frac{d\bar{\Omega}}{4\pi}, \tag{5.33}$$

as shown in Section 4.2. This allows us to write the three-body phase space as

$$\begin{aligned} dLips^3 &= \frac{1}{2^6 (2\pi)^4} \int_{m_W^2}^{s} dq_1^2 \\ &\quad \times \frac{(s - q_1^2)(q_1^2 - Q^2)}{s q_1^2}\, d\phi\, d\cos\theta_P\, d\cos\theta_q, \end{aligned} \tag{5.34}$$

where ϕ is the angle of intersection of the plane defined by $\chi\chi \to e e^*$ with that defined by $e\nu W$, and θ_P and θ_q are defined in P (CoM) and q_1 rest frames, as

$$\vec{k}_1 \overset{P}{=} \frac{\sqrt{s}}{2} |\vec{v}| (\sin\theta_P \cos\phi, \sin\theta_P \sin\phi, \cos\theta_P), \tag{5.35}$$

$$\vec{k}_2 \overset{P}{=} -\frac{\sqrt{s}}{2} |\vec{v}| (\sin\theta_P \cos\phi, \sin\theta_P \sin\phi, \cos\theta_P), \tag{5.36}$$

$$\vec{q}_1 \overset{P}{=} (0, 0, E_2^P), \tag{5.37}$$

$$\vec{p}_2 \overset{P}{=} (0, 0, -E_2^P), \tag{5.38}$$

$$\vec{p}_1 \overset{q_1}{=} E_1^{q_1} (\sin\theta_q, 0, \cos\theta_q), \tag{5.39}$$

$$\vec{Q}_1 \overset{q_1}{=} -E_1^{q_1} (\sin\theta_q, 0, \cos\theta_q), \tag{5.40}$$

where $\overset{P}{=}, \overset{q_1}{=}$ denote evaluation in the lab and q_1 rest frames respectively. We evaluate the scalar products that arise in the amplitude squared in terms of the invariants q_1^2,

$Q^2 = m_W^2$, $s = 4m_\chi^2/(1-v^2)$ and the angles θ_P, θ_q, and ϕ,

$$2k_1\cdot k_2 = s - 2m_\chi^2 \tag{5.41}$$

$$2q\cdot p_2 = s - q_1^2 \tag{5.42}$$

$$2k_1\cdot q_1 = -t_1 + m_\chi^2 + q_1^2 \tag{5.43}$$

$$2k_2\cdot p_2 = -t_1 + m + \chi^2 \tag{5.44}$$

$$2k_1\cdot p_2 = -u_1 + m_\chi^2 \tag{5.45}$$

$$2k_2\cdot q_1 = -u_1 + m_\chi^2 + q_1^2 \tag{5.46}$$

$$2p_1\cdot Q = q_1^2 - Q^2 \tag{5.47}$$

$$2q_1\cdot Q = q_1^2 + Q^2 \tag{5.48}$$

$$2q_1\cdot p_1 = q_1^2 - Q^2 \tag{5.49}$$

$$\begin{aligned} k_1\cdot Q &= \frac{1}{8q_1^2}\left[(s+q_1^2)(q_1^2+Q^2) - (s-q_1^2)(q_1^2-Q^2)\cos\theta_q\right] \\ &+ \frac{|\vec{v}_\chi|}{8q_1^2}\Big[2\sqrt{s}\sqrt{q_1^2}(q_1^2-Q^2)\sin\theta_P\sin\theta_q\cos\phi \\ &\quad -(s-q_1^2)(q_1^2+Q^2)\cos\theta_P + (s+q_1^2)(q_1^2-Q^2)\cos\theta_q\cos\theta_P\Big] \end{aligned} \tag{5.50}$$

$$\begin{aligned} k_2\cdot Q &= \frac{1}{8q_1^2}\left[(s+q_1^2)(q_1^2+Q^2) - (s-q_1^2)(q_1^2-Q^2)\cos\theta_q\right] \\ &- \frac{|\vec{v}_\chi|}{8q_1^2}\Big[2\sqrt{s}\sqrt{q_1^2}(q_1^2-Q^2)\sin\theta_P\sin\theta_q\cos\phi \\ &\quad -(s-q_1^2)(q_1^2+Q^2)\cos\theta_P + (s+q_1^2)(q_1^2-Q^2)\cos\theta_q\cos\theta_P\Big] \end{aligned} \tag{5.51}$$

$$\begin{aligned} p_2\cdot Q &= \frac{s-q_1^2}{8sq_1^2}\left[(s+q_1^2)(q_1^2+Q^2) - (s-q_1^2)(q_1^2-Q^2)\cos\theta_q\right] \\ &+ \frac{s-q_1^2}{8sq_1^2}\left[(s-q_1^2)(q_1^2+Q^2) - (s+q_1^2)(q_1^2-Q^2)\cos\theta_q\right] \end{aligned} \tag{5.52}$$

$$k_1\cdot p_1 = k_1\cdot q_1 - k_1\cdot Q \tag{5.53}$$

$$k_2\cdot p_1 = k_2\cdot q_1 - k_2\cdot Q \tag{5.54}$$

$$p_2\cdot p_1 = p_2\cdot q_1 - p_2\cdot Q, \tag{5.55}$$

where

$$\begin{aligned}
t_1 &= (k_1 - q_1)^2 = (k_2 - p_2)^2 = k_2^2 + p_2^2 - 2k_2 \cdot p_2 \\
&= m_\chi^2 - \frac{1}{2}(s - q_1^2)(1 - v\cos\theta_P), \qquad (5.56)\\
u_1 &= (k_1 - p_2)^2 = (k_2 - q_1)^2 = m_\chi^2 + p_2^2 - 2k_1 \cdot p_2 \\
&= m_\chi^2 - \frac{1}{2}(s - q_1^2)(1 + v\cos\theta_P). \qquad (5.57)
\end{aligned}$$

Expanding in powers of the DM velocity v and keeping only the leading order (v^0) contribution, we find the amplitude squared to be

$$\begin{aligned}
|\mathcal{M}|^2 = \quad & (\cos\theta_q + 1)(q_1^2 - 4m_\chi^2)(m_W^2 - q_1^2) \\
& \times \Big[q_1^4 \left(q_1^4 \,(\cos\theta_q^2 - 2\cos\theta_q + 5) + 16\, m_\chi^4 \,(\cos\theta_q - 1)^2 - 8\, m_\chi^2\, q_1^2 \,(\cos\theta_q - 1)^2 \right) \\
& -2\, m_W^2\, q_1^2 \left(16\, m_\chi^4 \,(\cos^2\theta_q - 1) + 8\, m_\chi^2\, q_1^2 \,(\cos\theta_q - \cos^2\theta_q + 2) + q_1^4 \,(\cos\theta_q - 1)^2 \right) \\
& + m_W^4 \left(4m_\chi^2 \,(\cos\theta_q + 1) - \cos\theta_q\, q_1^2 + q_1^2 \right)^2 \Big] \Big/ \\
& \Big(q_1^2 \,(q_1^2 - 2m_\eta^2 - 2m_\chi^2)^2 \Big(q_1^2 \,(4\cos\theta_q\, m_\chi^2 - \cos\theta_q\, q_1^2 + 4m_\eta^2 + q_1^2) \\
& - m_W^2 \,(4m_\chi^2 \,(\cos\theta_q + 1) - \cos\theta_q\, q_1^2 + q_1^2) \Big)^2 \Big) \qquad (5.58)
\end{aligned}$$

Finally, we calculate the cross section for W emission following the procedure outlined above. As expected, we have an unsuppressed cross section given by

$$\begin{aligned} v\sigma \simeq\ & \frac{\alpha_W f^4}{256\pi^2 m_\chi^2} \Bigg\{ (\mu+1)\left[\frac{\pi^2}{6} - \ln^2\left(\frac{2m_\chi^2(\mu+1)}{4m_\chi^2\mu - m_W^2}\right) - 2\mathrm{Li}_2\left(\frac{2m_\chi^2(\mu+1) - m_W^2}{4m_\chi^2\mu - m_W^2}\right)\right. \\ & +2\mathrm{Li}_2\left(\frac{m_W^2}{2m_\chi^2(\mu+1)}\right) - \mathrm{Li}_2\left(\frac{m_W^2}{m_\chi^2(\mu+1)^2}\right) - 2\mathrm{Li}_2\left(\frac{m_W^2(\mu-1)}{2(m_\chi^2(\mu+1)^2 - m_W^2)}\right) \\ & +2\ln\left(\frac{4m_\chi^2\mu - m_W^2}{2m_\chi^2(\mu-1)}\right)\ln\left(1 - \frac{m_W^2}{2m_\chi^2(\mu+1)}\right) \\ & \left. +\ln\left(\frac{m_W^2(\mu-1)^2}{4(m_\chi^2(\mu+1)^2 - m_W^2)}\right)\ln\left(1 - \frac{m_W^2}{m_\chi^2(\mu+1)^2}\right)\right] \\ & +\frac{(4\mu+3)}{(\mu+1)} - \frac{m_W^2\left(4m_\chi^2(\mu+1)(4\mu+3) - (m_W^2 - 4m_\chi^2)(\mu-3)\right)}{16m_\chi^4(\mu+1)^2} \\ & +\frac{m_W^2\left(4m_\chi^4(\mu+1)^4 - 2m_W^2m_\chi^2(\mu+1)(\mu+3) - m_W^4(\mu-1)\right)}{4m_\chi^4(\mu+1)^3\left(m_\chi^2(\mu+1)^2 - m_W^2\right)}\ln\left(\frac{m_W^2}{4m_\chi^2}\right) \\ & +\ln\left(\frac{2m_\chi^2(\mu-1)}{2m_\chi^2(\mu+1) - m_W^2}\right)\frac{(\mu-1)\left(2m_\chi^2(\mu+1) - m_W^2\right)}{4m_\chi^4(\mu+1)^3(4m_\chi^2\mu - m_W^2)\left(m_\chi^2(\mu+1)^2 - m_W^2\right)} \\ & \times(4m_\chi^6(\mu+1)^4(4\mu+1) - m_\chi^4m_W^2(\mu+1)^2\left(3\mu(\mu+6)+7\right) \\ & +2m_\chi^2m_W^4\left(\mu(\mu+4)+1\right) - m_W^6)\Bigg\} \end{aligned} \tag{5.59}$$

where $\alpha_W \equiv g^2/(4\pi)$. The Spence function (or "dilogarithm") is defined as $\mathrm{Li}_2(z) \equiv -\int_0^z \frac{d\zeta}{\zeta}\ln|1-\zeta| = \sum_{k=1}^{\infty}\frac{z^k}{k^2}$.

If we take the limit $m_W \to 0$ and replace α_W with $2\alpha_{\rm em}$, then Eqn. 5.59 reproduces the cross section for bremsstrahlung of photons in this model, namely[3]

$$\begin{aligned} v\sigma \simeq \frac{\alpha_{\rm em} f^4}{128\pi^2 m_\chi^2} \quad & \left\{ (\mu+1)\left[\frac{\pi^2}{6} - \ln^2\left(\frac{\mu+1}{2\mu}\right) - 2\mathrm{Li}_2\left(\frac{\mu+1}{2\mu}\right)\right]\right. \\ & \left. +\frac{4\mu+3}{\mu+1} + \frac{4\mu^2 - 3\mu - 1}{2\mu}\ln\left(\frac{\mu-1}{\mu+1}\right)\right\}. \end{aligned} \tag{5.60}$$

The successful recovery of the photon bremsstrahlung result in the massless W limit provides a check on the rather complicated expression for massive W bremsstrahlung given above in Eqn. 5.59.

Since we are working in the limits $v = 0$ and $m_f = 0$, the nonzero results in Eqns. 5.59 and 5.60 imply that the leading terms are neither helicity nor velocity

---

[3] Note that Eqn. 2 of Ref. [199] is larger by an overall factor of two, and also has the opposite sign for the $(1+\mu)[...]$ term, while Eqn. 1 of Ref. [199] is consistent with our results.

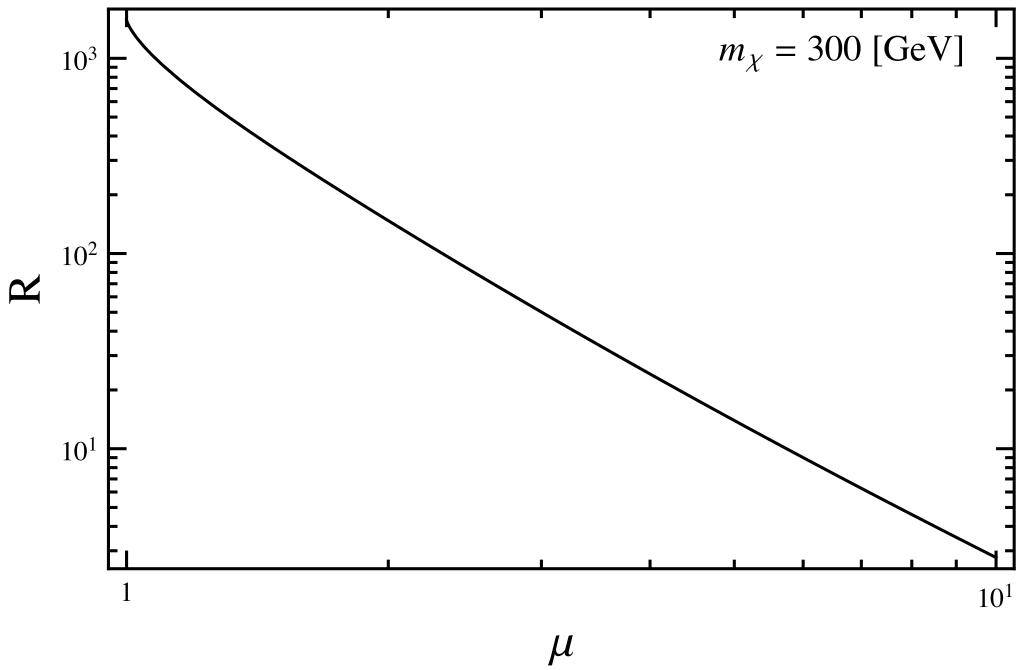

Figure 5.2: The ratio $R = v\,\sigma(\chi\chi \to e^+\nu W^-)/v\,\sigma(\chi\chi \to e^+e^-)$ as a function of $\mu = (m_\eta/m_\chi)^2$, for $m_\chi = 300$ GeV. We have used $v = 10^{-3}c$, appropriate for the Galactic halo.

suppressed. Not clear from the mathematical expressions is the sensible fact that the cross sections fall monotonically with increasing m_η (or μ). This monotonic fall is shown in Fig. 5.2, where we plot the ratio of the W-strahlung cross section to that of the lowest order process, $R = v\,\sigma(\chi\chi \to e^+\nu W^-)/v\,\sigma(\chi\chi \to e^+e^-)$. The lowest order process itself falls as μ^{-2}, so the W-strahlung process falls as μ^{-4}. This latter dependence is expected for processes with two propagators each off-shell by $1/\mu$.

Importantly, the effectiveness of the W-strahlung processes in lifting suppression of the annihilation rate is evident in Fig. 5.2. The ratio is maximized for μ close to 1, where m_χ and m_η are nearly degenerate. However, the W-strahlung process dominates over the tree level annihilation even if a mild hierarchy between m_χ and m_η is assumed. The ratio exceeds 100 for $\mu \lesssim 2$.

Fig. 5.3 illustrates that the ratio R is insensitive to the DM mass, except for

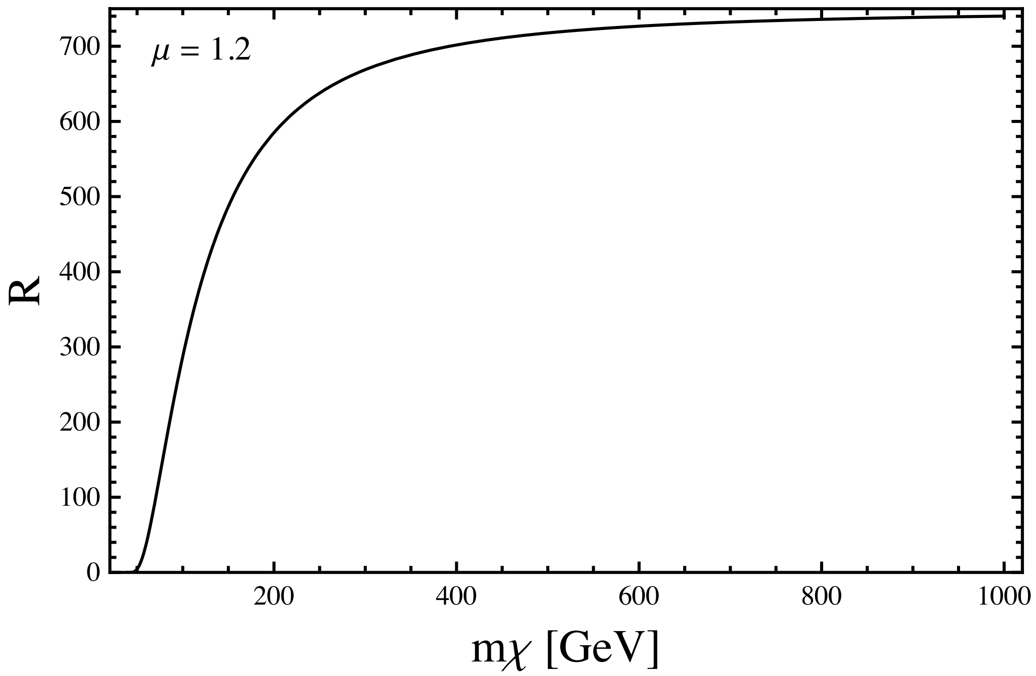

Figure 5.3: The ratio $R = v\,\sigma(\chi\chi \to e^+\nu W^-)/v\,\sigma(\chi\chi \to e^+e^-)$ as a function of the DM mass m_χ, for $\mu = 1.2$ GeV. We have used $v = 10^{-3}c$, appropriate for the Galactic halo.

low m_χ where the W mass significantly impacts phase space. From the figure one gleans that for $m_\chi \gtrsim 3\,m_W$, the ratio R is already near to its asymptotic value. Incidentally, the asymptotic value may be obtained analytically by dividing Eqn. 5.60 with Eqn. 5.8 and rescaling α_{em} with $\alpha_W/2$.

In Fig. 5.4 we compare the W-strahlung cross section with that for photon bremsstrahlung in this model. (Note that this is for a model where bremsstrahlung lifts helicity suppression. This cross section differs from the general photon bremsstrahlung cross section used in Chapter 3). For high dark matter masses where the W mass is negligible, the two cross sections are identical except for the overall normalization, which is higher by a factor of $1/(2\sin^2\theta_W) = 2.17$ for W-strahlung. For lower DM mass, the available phase space is reduced due to W mass effects, and thus the W-strahlung cross section falls below that for photons. This can be seen in

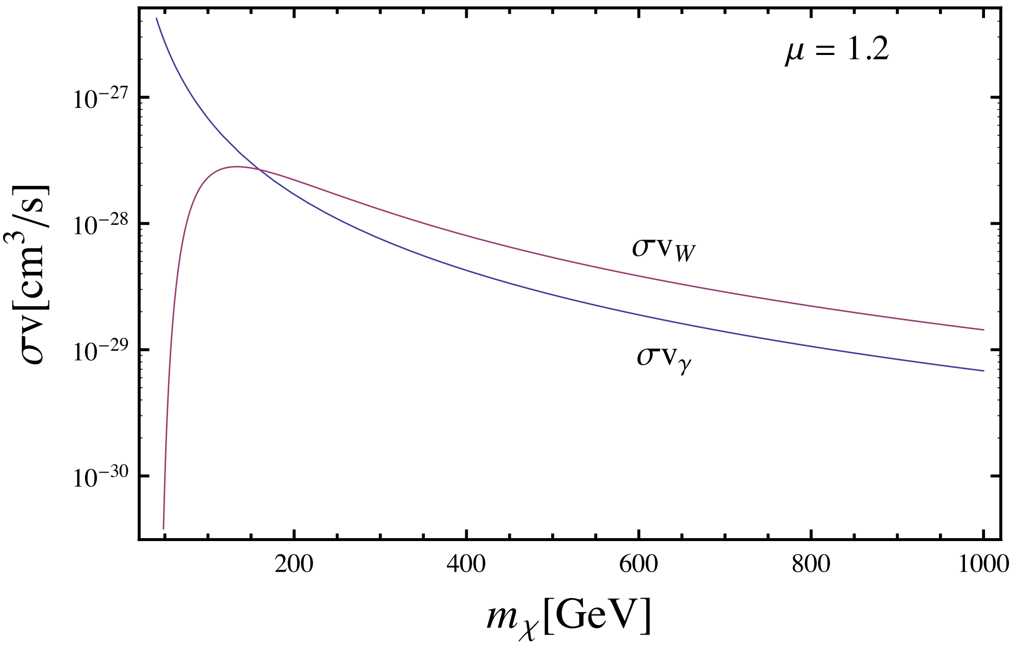

Figure 5.4: The cross sections for $\chi\chi \to e^+\nu W^-$ (red) and $\chi\chi \to e^+e^-\gamma$ (blue), for $\mu = 1.2$ and coupling $f = 1$. For large DM mass, the cross sections differ by a factor of $1/(2\sin^2\theta_W) = 2.17$ while for m_χ comparable to m_W the W bremsstrahlung cross section is suppressed by phase space effects.

Fig. 5.4 for $m_\chi \lesssim 150$ GeV (this number is fairly insensitive to μ). Another factor of two is gained for W-strahlung when the W^+ mode is added to the W^- mode shown here.

Nominally, the correct dark matter energy fraction is obtained for early-Universe thermal decoupling with an annihilation cross section of $3 \times 10^{-26}\mathrm{cm}^3/\mathrm{s}$. It is seen in Fig. 5.4 that the W-strahlung mode falls 2-3 orders of magnitude below this value. Note that at the time of dark matter freeze-out in the early Universe, the velocity suppression of the p-wave contribution is not as severe as it is for late-Universe annihilation. Hence, radiative W-strahlung with its natural suppression factor $\alpha_W/4\pi$ is probably not the dominant annihilation mode responsible for early-Universe decoupling of Majorana dark matter.

5.3.4 W and Lepton Spectra

To obtain the energy spectrum of the W, we need an expression for E_W in terms of the current integration variables. In the q_1 rest frame, the momenta $\vec{p}_1^{\,q_1}$ and $\vec{Q}^{q_1}$ are related via

$$\begin{aligned} |\vec{p}_1^{\,q_1}| &= |\vec{Q}^{q_1}| \\ E_{p_1}^{q_1} &= \sqrt{(E_W^{q_1})^2 - m_W^2}, \end{aligned} \tag{5.61}$$

and by conservation of energy,

$$\begin{aligned} \sqrt{q_1^2} &= E_W^{q_1} + E_{p_1}^{q_1} = E_W^{q_1} + \sqrt{(E_W^{q_1})^2 - m_W^2} \\ E_W &= \frac{q_1^2 + m_W^2}{2\sqrt{q_1^2}}. \end{aligned} \tag{5.62}$$

Performing a Lorentz boost, we find the W energy in the lab frame,

$$E_W = \frac{1}{4\sqrt{s q_1^2}} \left((s + q_1^2)(q_1^2 + m_W^2) - (s - q_1^2)(q_1^2 - m_W^2)\cos\theta_q \right), \tag{5.63}$$

which allows us to make the transformation

$$d\cos(\theta_q) \rightarrow \frac{-4\sqrt{s q_1^2}}{(s - q_1^2)(q_1^2 - m_W^2)} dE_W. \tag{5.64}$$

Using $q_1^{\mathrm{min,max}} = E_W \sqrt{s}(1 \pm \sqrt{1 - m_W^2/E_W^2})$, we find

$$\begin{aligned} v\frac{d\sigma}{dx_W} = \; & \frac{\alpha_W f^4}{128\pi^2 m_\chi^2} \left((1 - x_W) + \frac{m_W^2}{4m_\chi^2} \right) \\ & \left\{ \sqrt{x_W^2 - \frac{m_W^2}{m_\chi^2}} \left[\frac{2}{\left((\mu+1)(\mu+1-2x_W) + \frac{m_W^2}{m_\chi^2} \right)} - \frac{1}{(\mu+1-x_W)^2} \right] \right. \\ & \left. - \frac{\left((\mu+1)(\mu+1-2x_W) + \frac{m_W^2}{m_\chi^2} \right)}{2(\mu+1-x_W)^3} \ln \left(\frac{\mu+1-x_W+\sqrt{x_W^2 - m_W^2/m_\chi^2}}{\mu+1-x_W-\sqrt{x_W^2 - m_W^2/m_\chi^2}} \right) \right\}. \end{aligned} \tag{5.65}$$

The energy spectrum of the the primary leptons is calculated in similar fashion. We find

$$\begin{aligned} v\frac{d\sigma}{dx_l} = \quad & \frac{\alpha_W f^4}{512\pi^2 m_\chi^2}\frac{1}{(\mu-1+2x_l)^2} \\ & \Bigg\{\left(4(1-x_l)^2-4x_l(\mu+1)+3(\mu+1)^2-\frac{m_W^2}{m_\chi^2}(\mu+3)\right) \\ & \times\ln\left(\frac{2m_\chi^2(\mu+1)(1-x_l)-m_W^2}{\left(2m_\chi^2(\mu+1-2x_l)-m_W^2\right)(1-x_l)}\right) \\ & -\frac{x_l\left(4m_\chi^2(1-x_l)-m_W^2\right)}{\left(2m_\chi^2(1-x_l)(\mu+1)-m_W^2\right)(1-x_l)^2} \\ & \times\left[(1-x_l)^2\left(4(1-x_l)^2-x_l(\mu+1)+3(\mu+1)^2\right)\right. \\ & \left.+\frac{m_W^2}{4m_\chi^2}(1-x_l)\left(x_l(\mu+11)-4(\mu+3)\right)-x_l\frac{m_W^4}{8m_\chi^4}\right]\Bigg\}. \end{aligned} \tag{5.66}$$

The W spectrum per $\chi\chi\rightarrow e\nu W$ event is given in Fig. 5.5. We use the scaling variable $x_W \equiv E_W/m_\chi$, and plot $dN/dx_W \equiv (\frac{1}{\sigma_{e^+\nu W^-}})\frac{d\sigma_{e^+\nu W^-}}{dx_W}$. The kinematic range of x_W is $[\frac{m_W}{m_\chi},\, (1+\frac{m_W^2}{4m_\chi^2})]$, with the lower limit corresponding to a W produced at rest, and the upper limit corresponding to parallel lepton momenta balancing the opposite W momentum. As evident in Fig. 5.5, the W boson spectrum has a broad energy distribution, including a significant high energy component.

For the lepton energy spectrum, the range of the scaling variable $x_\ell \equiv E_\ell/m_\chi$ is $[\,0,\, 1-\frac{m_W^2}{4m_\chi^2}]$. Both limits arise when one lepton has zero energy and the other is produced back-to-back with the W. The lepton spectrum is shown in Fig. 5.6. Note that this spectrum is valid for either the e^+ or the ν from the annihilation $\chi\chi\rightarrow e^+\nu W^-$, and for either e^- or $\bar\nu$ from the annihilation $\chi\chi\rightarrow e^-\bar\nu W^+$.

5.3.5 Z Emission

Consider the process producing the $\bar\nu\nu Z$ final state. The cross sections for the Z-strahlung processes are related to those for W-strahlung in a simple way: The amplitudes producing $\bar\nu\nu Z$ arise from the same six graphs of Fig. 5.1, where e, W and

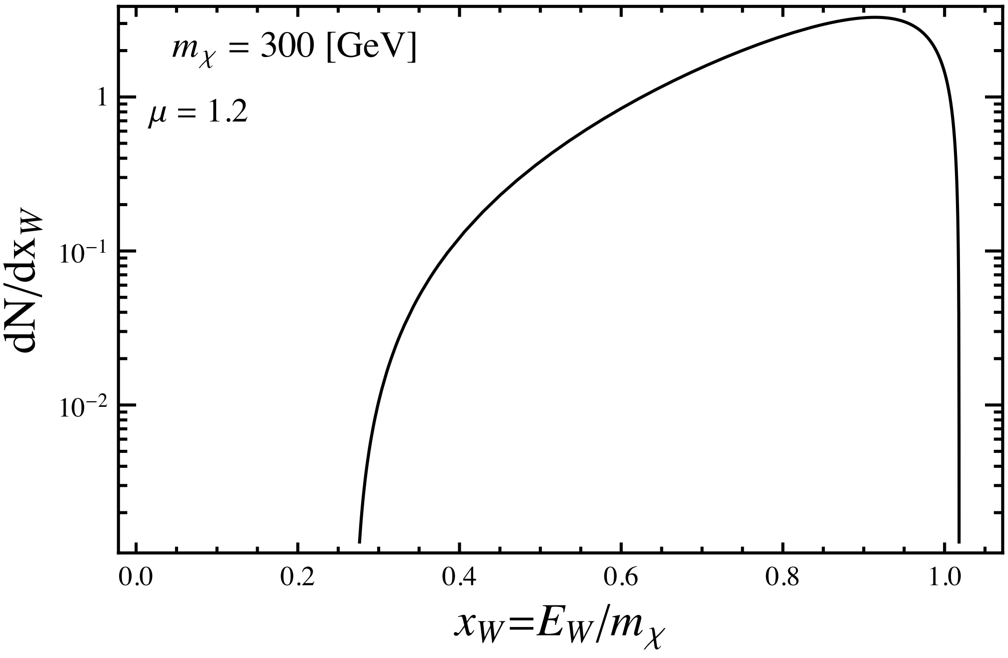

Figure 5.5: The W spectrum per $\chi\chi \to e\nu W$ annihilation for $m_\chi = 300$ GeV and $\mu = 1.2$.

η^+ are replaced everywhere by ν and Z and η_0, respectively. The calculation of the amplitudes, and their interferences, proceeds in an identical fashion. After making the replacement $m_W \to m_Z$, the cross section for the annihilation process $\chi\chi \to \nu\bar{\nu}Z$ differs from that for $\chi\chi \to e^+\nu W^-$ by only an overall normalization factor,

$$\begin{aligned} v\,\sigma_{\nu\bar{\nu}Z} &= \frac{1}{(2\cos^2\theta_W)} \times v\,\sigma_{e^+\nu W^-}\Big|_{m_W \to m_Z} \\ &\simeq 0.65 \times v\,\sigma_{e^+\nu W^-}\Big|_{m_W \to m_Z}. \end{aligned} \tag{5.67}$$

Consider now the e^+e^-Z final state. Again, the amplitudes arise from the same six basic graphs of Fig. 5.1. Since only the left-handed leptons couple to the dark matter via the SU(2) doublet η, only the left handed component of e^- participates in the interaction with the Z. Therefore, the couplings of the charged leptons to Z

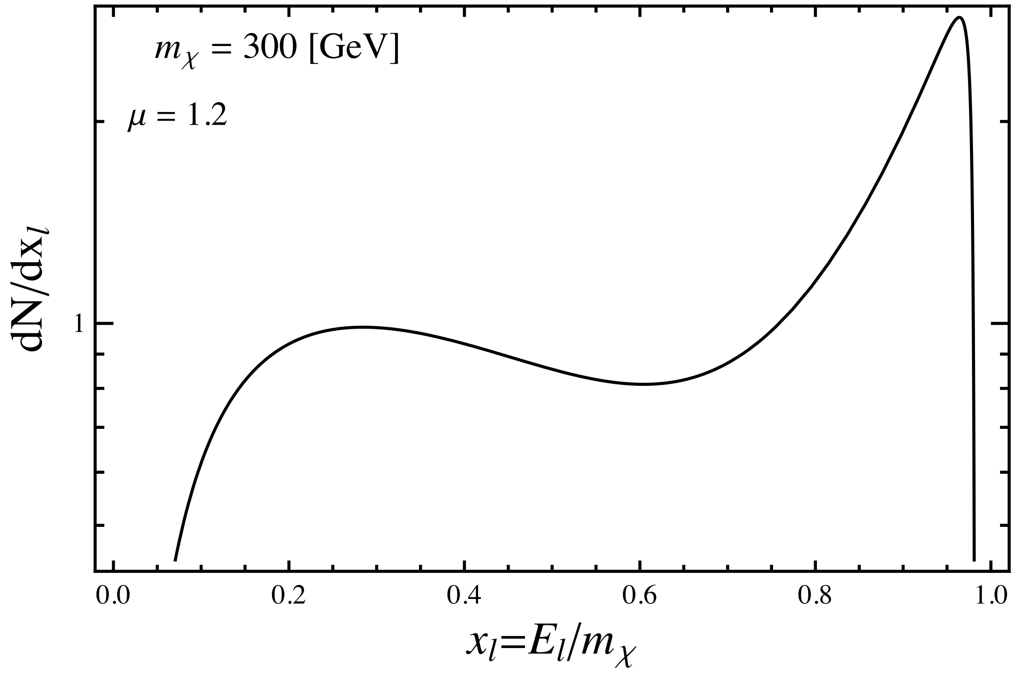

Figure 5.6: The primary lepton spectrum per $\chi\chi \to e\nu W$ annihilation, for $m_\chi = 300$ GeV and $\mu = 1.2$.

and W take the same form, up to a normalization constant. We thus find

$$\begin{aligned} v\,\sigma_{e^+e^-Z} &= \frac{2\left(\sin^2\theta_W - \frac{1}{2}\right)^2}{\cos^2\theta_W} \times v\,\sigma_{e^+\nu W^-}\Big|_{m_W\to m_Z} \\ &\simeq 0.19 \times \; v\,\sigma_{e^+\nu W^-}\Big|_{m_W\to m_Z} . \end{aligned} \tag{5.68}$$

Adding the four contributions to W/Zstrahlung, we find

$$v\,\sigma_{W/Z-\mathrm{strahlung}} = 2.84 \times v\,\sigma_{e^+\nu W^-} . \tag{5.69}$$

5.4 Discussion and Conclusions

In an attempt to explain recent anomalies in cosmic ray data in a dark matter framework, various non-standard properties have been invoked such as dominant annihilation to leptons in so-called leptophilic models. When the dark matter is Majorana in nature, such annihilations invariably are confronted by suppressions of such processes via either p-wave velocity suppression or helicity suppression. With the aid of Fierz transformation technology, which we have presented in some detail, we have elucidated the general circumstances where suppressions may be encountered.

It has been known for some time that photon bremsstrahlung may have a dramatic effect on such suppressions. We have shown that once one considers the inclusion of three body final states due to electroweak bremsstrahlung, one may also lift these suppressions.

There are clear advantages and disadvantages of seeking photon- versus W/Z-bremsstrahlung as an indirect signature of dark matter. With photon bremsstrahlung, the photon itself is easily detected. Its energy spectrum may then be readily compared to model predictions. With W-strahlung, it is the decay products of the W decay which must be sought. Their spectra are less attributable to the model of dark matter annihilation. However, the total rate for W/Z-strahlung exceeds that of photon-strahlung. Photons couple with strength e, W's couple with strength $g/\sqrt{2} = e/(\sqrt{2}\sin\theta_W)$, and Z's couple to neutrinos with strength $g/(2\cos\theta_W) = e/(2\cos\theta_W\sin\theta_W)$. Therefore in the high energy limit where the W and Z masses can be neglected, we expect

$$\sigma_{e^+\nu W^-} = \frac{1}{2\sin^2\theta_W}\sigma_{e^+e^-\gamma} = 2.17\sigma_{e^+e^-\gamma}. \tag{5.70}$$

So, in the high energy limit where $m_\chi \gtrsim 300\text{GeV} \gg m_W$, the total cross section becomes

$$\begin{aligned}\sigma_{\text{brem, total}} &= \sigma_{e^+\nu W^-} + \sigma_{\bar{\nu}e^-W^+} \\ &\quad + \sigma_{\bar{\nu}\nu Z} + \sigma_{e^+e^-Z} + \sigma_{e^+e^-\gamma} \\ &= 7.16\,\sigma_{e^+e^-\gamma}. \end{aligned} \tag{5.71}$$

Furthermore, the varied decay products of the W/Z allow more multi-messenger experiments to engage in the dark matter search. Charged leptons, protons and antiprotons, neutrinos, and even deuterons are expected, at calculable rates and with predictable spectra. Importantly, hadronic decay products are unavoidable, despite a purely leptonic 2-body→2-body annihilation. The tens of millions of Z events produced at CERN's e^+e^- collider show in detail what the branching fractions and spectra are for each kind of decay product. In Chapter 6 we reveal the favorable prospects for using W/Z-strahlung decay products as indirect signatures for dark matter.

The lifting of the helicity suppression is most significant in the limit where the mass of the boson mediating dark matter annihilation does not greatly exceed the mass of the dark matter particle. This is true both for photon bremsstrahlung and for W/Z-bremsstrahlung. In this limit, we find the three body final state annihilation channels can significantly dominate over two body annihilation channels. The region of parameter space where χ and η are approximately degenerate is of great interest in many models, since it coincides with the co-annihilation region where both $\chi\chi$ and $\chi\eta$ annihilations are important in determining the relic dark matter density at the time of freezeout in the early Universe, often a favored parameter region in SUSY scenarios.

6

Signals from Electroweak Bremsstrahlung

6.1 Introduction

Indirect DM detection has been the subject of much recent attention, due to measured cosmic ray excesses of positrons and electrons above those expected from conventional astrophysical processes. It has been proposed the excess electrons and positrons are not due to conventional astrophysics process, but arise instead from dark matter annihilation or decay in the Galactic halo. A plethora of DM models have been designed with this goal in mind, as discussed in detail in Section 1.3.6.

A viable resolution of the cosmic ray $e^{\pm}$ data by means of DM annihilation requires a large branching ratio to leptons. A large branching ratio to hadrons would make a contribution to cosmic ray antiproton fluxes, for which stringent observational bounds exist. Therefore, so called leptophilic models are preferred, in which DM couples (at tree level) only to leptons. However, recall from Chapter 5 that for many scenarios in which the DM particle is a Majorana fermion, annihilation to light fermions is helicity suppressed ($\propto m_f^2/s$) in the s-wave contribution, and of course velocity suppressed ($\propto v_{DM}^2$) in the p-wave contribution. This is the case for popular DM candidates such as the neutralino of supersymmetric models, if $\sqrt{s} \sim 2\,m_\chi$ is below the W^+W^- threshold; or Bino models with highly suppressed annihilation to W^+W^- and ZZ final states. Large boost factors would be required for such a scenario to explain any observed positron excess.

In Chapter 5 we have shown that in addition to the well-known lifting of helicity suppressions via emission of a gamma-ray, suppressions can also be lifted by the bremsstrahlung of a W or Z gauge boson. Where a helicity suppression is lifted, the cross sections for $\chi\chi \to \ell\bar{\ell}\gamma$, $\chi\chi \to \ell\bar{\ell}Z$ and $\chi\chi \to \ell\nu W$ can all greatly exceed that for the lowest order process $\chi\chi \to \ell\bar{\ell}$. The bremsstrahlung processes thus may allow for the indirect detection of many DM models which would otherwise be helicity suppressed.

Importantly, the decay of the W and Z gauge bosons inevitably leads to the production of secondary annihilation products, including gamma rays, hadrons, charged leptons and neutrinos, allowing multi-messenger searches. Note particularly, that even for DM models designed to be leptophilic, production of hadrons is unavoidable. (In fact, even for models in which on-shell production of W or Z gauge bosons is kinematically forbidden, some minimal hadron production is inescapable, due to loop processes, or the exchange of off-shell W or Z bosons.)

In this Chapter we examine the simple example model we used in Chapter 5, which has a helicity suppressed $2 \to 2$ cross section, provided by Ref. [86, 279]. We shall show that in this model, when electroweak bremsstrahlung lifts helicity suppression, the cross section required to produce positrons in sufficient quantity to account for the observed excess will lead to overproduction of antiprotons and gamma rays, and as such is ruled out as an explanation of the observed positron anomalies across most of the available parameter space. Though our calculation is performed for the reference scenario of Ref. [86, 279], we expect this conclusion to hold for all scenarios in which the dominant positron contributions arise from the 3-body W/Z-bremsstrahlung final states.

We calculate the spectra of both primary and secondary particles from unsuppressed electroweak–bremsstrahlung annihilation processes, and calculate the expected spectra and fluxes at Earth for a given annihilation cross section. We compare the Earthly fluxes with observational data to determine an upper limit on the annihilation cross section. Whilst our analysis techniques are conservative, there are large astrophysical uncertainties in the propagation of charged particles through galactic magnetic fields, and in the dark matter density profile which probably contains substructure. A rigorous treatment of these effects is beyond the scope of this work. Consequently, our constraints are illustrative of the upper limit on the cross section, but not robust.

6.2 Model

The example model we investigate is the Majorana DM version of the leptophilic model proposed in [86], as used in Chapter 5, which we briefly review here. The DM consists of a gauge-singlet Majorana fermion χ which annihilates to leptons via the interaction term

$$f\left(\nu\,\ell^-\right)_L\,\varepsilon\begin{pmatrix}\eta^+\\ \eta^0\end{pmatrix}\chi + h.c. = f(\nu_L\eta^0 - \ell_L^-\eta^+)\chi + h.c. \tag{6.1}$$

where f is a coupling constant, ε is the $SU(2)$-invariant antisymmetric matrix, and $(\eta^+,\,\eta^0)$ form the new $SU(2)$ doublet scalar which mediates the annihilation. For simplicity, we consider a coupling to the first generation of leptons only, and set $f=0$ for coupling to the $(\nu_\mu\,\mu^-)_L$ and $(\nu_\tau\,\tau^-)_L$ doublets. As described in Chapter 5, the p-wave contribution to the lowest order annihilation process $\chi\chi\to e^+e^-$ is suppressed by $v_\chi^2\sim 10^{-6}$, while the s-wave contribution is proportional to $(m_l/m_\chi)^2$. This cross section is given in Eqn. 5.8. The helicity suppressed s-wave term is absent in the $m_l=0$ limit, leaving only the v_χ^2-suppressed p-wave term.

While it is well known that photon bremsstrahlung $\chi\chi\to e^+e^-\gamma$ can lift this suppression [201, 193, 192, 200, 199, 194], we have shown in Chapter 5 that this is also the case for the electroweak bremsstrahlung channels $\chi\chi\to e^+e^-Z$, $\nu_e\bar{\nu}_eZ$, $e^+\nu_eW^-$, $e^-\bar{\nu}_eW^+$. For both W/Z and γ bremsstrahlung, the effect is most significant where the dark matter mass is nearly degenerate with the mass of the boson which mediates the annihilation process. In the high energy limit where the W/Z masses are negligible, the cross sections for W/Z bremsstrahlung reduce to that for γ bremsstrahlung, modulo different coupling constants. However, the respective sizes of the electromagnetic and electroweak coupling constants imply that the W/Z-strahlung cross section is a factor of several larger than that for γ-strahlung,

$$\sigma_{e^+\nu_e W^-} = \sigma_{e^-\bar{\nu}_e W^+} = \frac{1}{2\sin^2\theta_W}\,\sigma_{e^+e^-\gamma}, \tag{6.2}$$

$$\sigma_{\bar{\nu}_e\nu_e Z} = \frac{1}{4\cos^2\theta_W\sin^2\theta_W}\,\sigma_{e^+e^-\gamma}, \tag{6.3}$$

$$\sigma_{e^+e^-Z} = \frac{\left(\frac{1}{2}-\sin^2\theta_W\right)^2}{\cos^2\theta_W\sin^2\theta_W}\,\sigma_{e^+e^-\gamma}, \tag{6.4}$$

$$\tag{6.5}$$

and thus

$$v\,\sigma_{W/Z-\text{strahlung}} = 6.16\,v\,\sigma_{e^+e^-\gamma}. \tag{6.6}$$

At lower energies, the phase space for W/Z bremsstrahlung is somewhat reduced due to the effects of the finite W/Z masses.

The bremsstrahlung cross section dominates over that for the lowest order $2 \to 2$ process, provided that m_η does not greatly exceded m_χ. Recall that the ratio $R_W = v\sigma_{e^+\nu_e W^-}/(v\sigma_{e^+e^-})$ was plotted in Figs. 5.2 and 5.3, and is largest for $\mu = (m_\eta/m_\chi)^2 = 1$. However, the W-strahlung process dominates over the $2 \to 2$ annihilation even if a mild hierarchy between m_χ and m_η is assumed, with $R_W > 1$ for $\mu \lesssim 10$. Therefore, when $\mu \lesssim 10$, production of mono-energetic leptons will be subdominant to particles produced in the 3-body processes (both primary and through gauge boson decay), a feature which must be accounted for when analysing astrophysical signatures of these models.

We use the cross sections calculated in Chapter 5 and Refs. [199, 194] in combination with the PYTHIA code [282, 283] to determine the spectra of gamma rays, electrons, protons, and their antiparticles, per annihilation to the five 3-body final states listed above (one electromagnetic bremsstrahlung and four electroweak bremsstrahlung processes). After accounting for propagation effects for the charged particles, we constrain these cross sections by comparing the observed flux with the calculated annihilation signal.

Although the spectra of annihilation products which we show are unique to the particular model we have chosen, we expect the results to apply qualitatively to any model where W/Z-bremsstrahlung is the dominant annihilation mode (i.e. where helicity suppression of the $2 \to 2$ s-wave is lifted by electroweak bremsstrahlung).

6.3 Cross Section Channel

As previously mentioned, the model we look at is leptophilic in the $2 \to 2$ process, and therefore has five 3-body bremsstrahlung channels,

$$\chi\chi \to e^+e^-Z,\ \nu\bar{\nu}Z,\ e^+\nu W^-,\ e^-\bar{\nu}W^+,\ e^+e^-\gamma, \tag{6.7}$$

which simultaneously contribute to the dark–matter annihilation fluxes. The cross sections and spectra for the electroweak channels are specified in Eqns. 5.59, 5.66, 5.66, 5.67 and 5.68 while those for the electromagnetic channel are, from Refs. [199, 194],

$$\begin{aligned} \frac{dv\sigma_{e^+e^-\gamma}}{dE_\gamma} &= \frac{\alpha}{64\pi^2 m_\chi^3}(1-x)\Bigg(\frac{(1+\mu)(1+\mu-2x)}{(1+\mu-x)^3}\mathrm{Ln}\left[\frac{1+\mu-2x}{1+\mu}\right] \\ &+ \frac{4x}{(1+\mu)(1+\mu-2x)} - \frac{2x}{(1+\mu-x)^2}\Bigg), \end{aligned} \tag{6.8}$$

$$\begin{aligned} \frac{dv\sigma_{e^+e^-\gamma}}{dE_{e^+}} &= \frac{dv\sigma_{e^+e^-\gamma}}{dE_{e^-}} = \frac{\alpha}{256\pi^2 m_\chi^3}\frac{1}{(2y+\mu-1)^2} \\ &\times \Bigg(\left(4(1-y)^2 - 4y(1+\mu) + 3(1+\mu)^2\right)\mathrm{Ln}\left[\frac{1+\mu}{1+\mu-2y}\right] \\ &- \left(4(1-y)^2 - y(1+\mu) + 3(1+\mu)^2\right)\left(\frac{2y}{1+\mu}\right)\Bigg), \end{aligned} \tag{6.9}$$

where $\mu = (m_\eta/m_\chi)^2$, $x = E_\gamma/m_\chi$ and $y = E_e/m_\chi$. The total bremsstrahlung cross section is given by the sum

$$\begin{aligned} v\sigma_{\rm Brem} &= v\sigma_{e^+e^-Z} + v\sigma_{\nu\bar{\nu}Z} \\ &+ v\sigma_{e^+\nu W^-} + v\sigma_{e^-\bar{\nu}W^+} + v\sigma_{e^+e^-\gamma}. \end{aligned} \tag{6.10}$$

The total bremsstrahlung cross section is a factor of ∼ 7.2 larger than that for photon bremsstrahlung alone, due to the four W/Z channels, which are governed by somewhat larger coupling constants. We shall consider parameters for which the bremsstrahlung channels dominate the total cross section, so that $v\sigma_{\rm Brem} \simeq v\sigma_{total}$. We define the "branching ratio" for an individual channel $i \in \{e^+e^-Z, \nu_e\bar{\nu}_eZ,\, e^+\nu_eW^-,\, e^-\bar{\nu}_eW^+,\, e^+e^-\gamma\}$ as

$$BR_{\rm Brem}(i) = \frac{v\sigma_i}{v\sigma_{\rm Brem}}. \tag{6.11}$$

The spectrum per annihilation, for any given annihilation product, $k \in \{\gamma,\, e^-,\, e^+,\, \nu,\, \bar{\nu},\, p,\, \bar{p}\}$, is then given by

$$\left.\frac{dN_k}{dE_k}\right|_{\rm Brem} = \sum_i BR_{\rm Brem}(i) \left.\frac{dN_k}{dE_k}\right|_{{\rm per}\,\chi\chi\to i}. \tag{6.12}$$

Here, $\left.\frac{dN_k}{dE_k}\right|_{{\rm per}\,\chi\chi\to i}$ is the spectrum per annihilation for a given channel. The spectra for $\gamma, e^\pm$, ν and $\bar{\nu}$ include primary annihilation products and secondary annihilation products produced by gauge boson fragmentation. The spectra for p and $\bar{p}$ arise exclusively from gauge boson fragmentation. The branching ratios and spectra depend on the parameter $\mu = (m_\eta/m_\chi)^2$. However, as long as the 3-body final states remain the dominant channel, the spectra (and thus the final results) have little dependence on this parameter. We show results for $\mu = (m_\eta/m_\chi)^2 = 1.2$, but results remain qualitatively unchanged when bremsstrahlung channels dominate over 2 → 2 processes.

Finally, the flux of a given annihilation product is schematically

$$\frac{d\phi_k}{dE_k} \propto v\sigma_{\rm Brem} \left.\frac{dN_k}{dE_k}\right|_{\rm Brem}. \tag{6.13}$$

The detailed evaluation of these annihilation spectra is given below.

6.4 Annihilation Spectra

In order to place constraints on the cross section, we need the spectrum of stable particles (ν, e^-, p and their antiparticles, plus γ) produced per dark matter annihilation. As an example, we describe how we determine the spectrum of antiprotons per $\chi\chi \to \nu_e e^+ W^-$ event; the technique is very similar for other secondary particles, and other electroweak–bremsstrahlung annihilation channels. These partial spectra are then summed to form $\left.\frac{dN_k}{dE_k}\right|_{\mathrm{Brem}}$.

We use the PYTHIA code [282, 283] to find the spectrum of antiprotons per W^- decay, $dN_{\bar{p}}/dE|_{\mathrm{Wdecay}}$. We produce a W^- boson in its rest frame by colliding an anti-muon with a muon neutrino, with center of mass energy m_W, and turning off all processes other than $\mu^\pm \nu_\mu(\bar{\nu}_\mu) \to W^\pm$. (Similarly, to produce the Z boson, we collide a e^+e^- pair at CoM energy m_Z, leaving Z production as the only active process.) Unstable W^- decay products (mainly pions) themselves decay, finally leaving only neutrinos, electrons, protons and their antiparticles, plus gamma rays in the final state. These stable particles are placed in 2000 logarithmically-spaced energy bins. The final spectrum is found by averaging the PYTHIA spectra over 10,000 such events.

We use this energy spectrum, in combination with the W^- (or Z) energy distribution per annihilation, $dN_W/d\gamma = (1/v\sigma)(dv\sigma/d\gamma)$, where $\gamma = E_W/m_W$, to find the antiproton energy-spectrum per annihilation in the lab frame:

$$\begin{aligned}\frac{dN_{\bar{p}}(E)}{dE} &= \int_{-1}^{1} \frac{d\cos\theta'}{2} \int d\gamma \frac{dN_W}{d\gamma} \\ &\times \int dE' \, \frac{dN_{\bar{p}}}{dE'} \, \delta(E - [\gamma E' + \beta\gamma p' \cos\theta']) \,,\end{aligned} \tag{6.14}$$

with $p' = \sqrt{E'^2 - m_{\bar{p}}^2}$, $\beta\gamma = \sqrt{\gamma^2 - 1}$. The $\cos\theta'$ integral is easily done, and one gets

$$\frac{dN_{\bar{p}}(E)}{dE} = \frac{1}{2} \int_1^\infty \frac{d\gamma}{\sqrt{\gamma^2 - 1}} \frac{dN_W}{d\gamma} \int_{E'_-}^{E'_+} \frac{dE'}{p'} \frac{dN_{\bar{p}}}{dE'} \,, \tag{6.15}$$

with $E'_{\pm} = \gamma E \pm \beta\gamma p$. Equivalently, we get

$$\frac{dN_{\bar{p}}(E)}{dE} = \frac{1}{2}\int_{m_{\bar{p}}}^{\infty} \frac{dE'}{p'}\,\frac{dN_{\bar{p}}}{dE'}\,, \int_{\gamma_-}^{\gamma_+} \frac{d\gamma}{\sqrt{\gamma^2-1}}\,\frac{dN_W}{d\gamma}\,, \tag{6.16}$$

with $\gamma_{\pm} = (EE' \pm pp')/m_{\bar{p}}^2$ and $p = \sqrt{E^2 - m_{\bar{p}}^2}$. We have assumed the spectrum of antiprotons per W decay to be isotropic. If the W polarization is not neglected, then the W decay amplitude includes Wigner functions $d^1_{\mu_i\mu_f}(\theta)$, which introduce a linear $\cos\theta$ or $\sin\theta$ term into Eqn. 6.14.

As given, Eqn. 6.16 applies to any particle type in the W or Z's final state. For example, it could be used to calculate the positron spectrum from W production and decay, if the spectrum of positrons per W decay were input in place of the antiproton spectrum.

Figure 6.1 shows the total gamma-ray spectrum, as well as the relative contributions from primary and secondary annihilation products, clearly showing that the secondary gamma rays are subdominant, except at low energy. Figure 6.2 shows the same information for the positron spectra, including the relative contributions to the primary positron spectrum from photon bremsstrahlung and electroweak bremsstrahlung, as well as the secondary positrons produced via gauge boson decay. In Figure 6.3 we show the total spectra per annihilation for electrons, neutrinos, protons, and gamma rays. Note that the electron/positron spectra from W/Z and photon bremsstrahlung have differing kinematic cutoffs due to the masses of the $W^{\pm}$ and Z bosons, leading to a kink near the endpoint in the electron/positron spectra. This feature is absent from the neutrino spectrum, as there is no contribution from photon bremsstrahlung. The neutrino spectrum includes contributions from primary electron neutrinos, and all flavors of secondary neutrinos from $W^{\pm}/Z$ decay. (The flavor ratios of primary neutrino production are model-dependent, given by $f_e^2 : f_\mu^2 : f_\tau^2$. We have assumed $f_\mu = f_\tau = 0$.)

It is illuminating to compare our spectra to those for annihilation to a pair of gauge bosons. The photon spectrum for the WIMP annihilation channel $\chi\chi \to W^+W^-$, shown for example in Fig. 1 of Cembranos et al. [284], has a somewhat

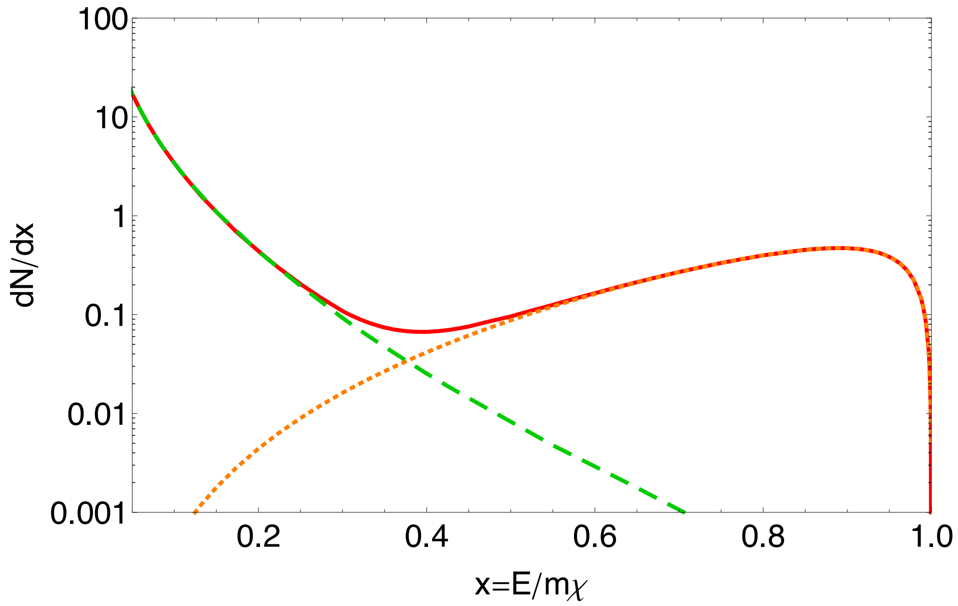

Figure 6.1: Contributions to the gamma-ray spectrum per annihilation, $\left.\frac{dN_\gamma}{dE}\right|_{\text{Brem}}$, from primary production in photon bremsstrahlung (dotted, orange), and W/Z decay products (dashed, green), for $m_\chi = 300$ GeV and $(m_\eta/m_\chi)^2 = 1.2$. The total gamma-ray spectrum is shown as a solid curve (red).

softer gamma spectrum, while we have a somewhat harder spectrum with more higher energy photons. This is to be expected, as gamma rays in Ref. [284] arise only from decay of mono-energetic W bosons ($E_W = m_\chi$), while the photon bremsstrahlung process contributes a harder primary gamma ray spectrum. The reverse holds true for the proton spectra, as our 3-body W/Z-bremsstrahlung process results in a broad distribution of W energies (the spectrum is shown in Fig. 5.5). In addition, the electron and neutrino spectra resulting from the $\chi\chi \to W^+W^-$ process would be quite different to those for electroweak bremsstrahlung, given that for the latter it is the primary leptons (not the secondaries from W/Z fragmentation) that make the dominant contribution. Of course, the spectra of charged particles observed at Earth will differ from that at production, due to the effect of energy loss processes during propagation. We address these effects in the following section.

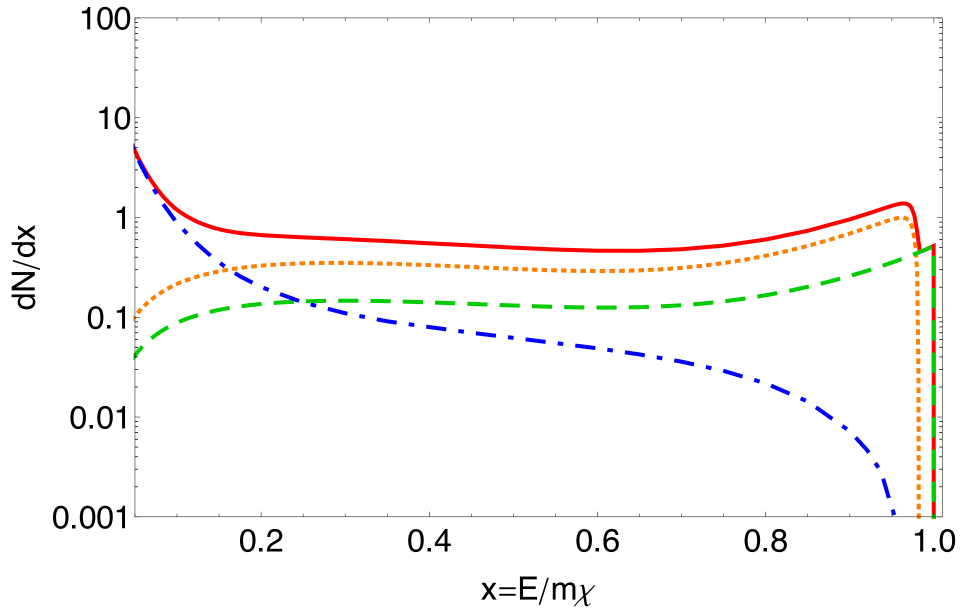

Figure 6.2: Contributions to the positron spectrum per annihilation, $\left.\frac{dN_{e^+}}{dE}\right|_{\text{Brem}}$, from primary production in electroweak bremsstrahlung channels (dotted, orange), primary production in the photon bremsstrahlung channel (dashed, green) and W/Z decay products (dot-dashed, blue), for $m_\chi = 300$ GeV and $(m_\eta/m_\chi)^2 = 1.2$. The total positron spectrum is shown as a solid curve (red). Note that the positron spectra from electroweak and photon bremsstrahlung have differing kinematic cutoffs due to the masses of the $W^\pm$ and Z bosons.

6.5 Constraints

In this section, we place upper limits on the thermally-averaged self-annihilation cross section, $\langle v\sigma\rangle_{\text{Brem}} \simeq \langle v\sigma\rangle_{total}$ as defined in Section 6.3 for the leptophilic model first described in Section 5.2.3. We do this by following the same technique as in Chapter 2 for the case of gamma rays, and a similar technique to Refs. [83, 74, 2] for charged particles and neutrinos. We compare the various predicted fluxes for a particular dark matter annihilation channel with the relevant observational flux measurements. We make the conservative assumption that the entire observed flux comes from DM annihilation; in reality, astrophysical backgrounds are likely to contribute a

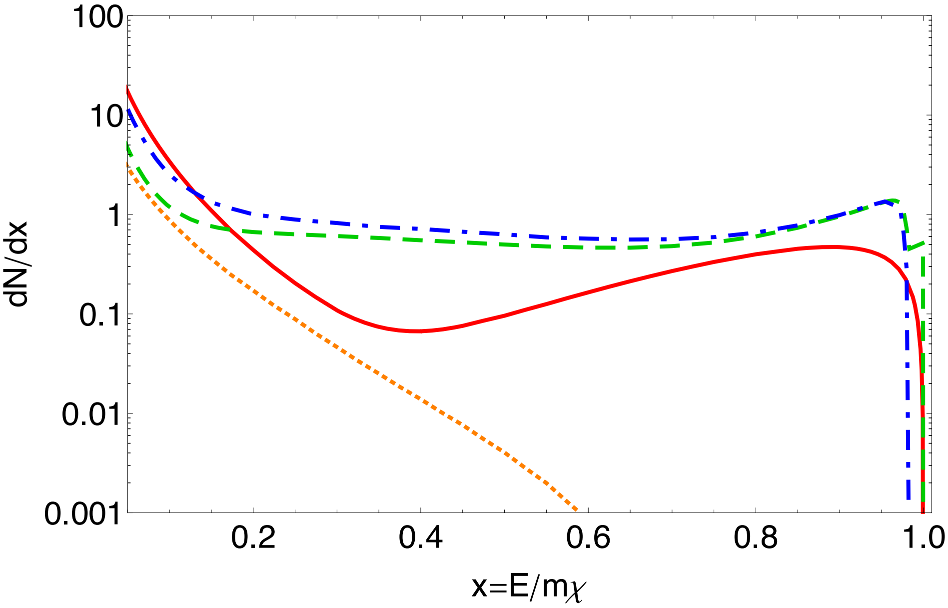

Figure 6.3: Spectrum per annihilation of photons (solid, red), protons (dotted, orange), electrons (dashed, green) and neutrinos (dot-dashed, blue), for $m_\chi = 300$ GeV and $(m_\eta/m_\chi)^2 = 1.2$. For protons, E is the kinetic energy. By CP–invariance, the particle and antiparticle spectra are the same, and antiparticles are not included in this figure. Note that the neutrino spectrum includes primary electron neutrinos, and all flavors of secondary neutrinos.

large fraction of the observed fluxes. The upper limit on the cross section is then determined such that the DM annihilation does not exceed any of the observed fluxes.

In calculating the constraints on $\langle v\sigma\rangle_{\rm Brem}$, we utilise the isotropic extragalactic gamma-ray flux measured by the Fermi collaboration [94], the positron fraction from the PAMELA collaboration [126], the Fermi $e^+ + e^-$ flux [125], as well as the antiproton flux and antiproton-to-proton ratio updated by the PAMELA collaboration in Ref. [270]. Throughout, we use the commonly-adopted Navarro, Frenk and White (NFW) dark matter density profile [28], defined in Section 1.1.7, with local dark matter density given by $\rho_\odot = 0.39$ GeV $/\text{cm}^{-3}$ [30]. In previous chapters, we used the Kravtsov profile, as our goal was to place robust, conservative upper limits.

Conversely, our goal here is to place indicative upper limits comparable with the limits produced by other groups, which motivates our adoption of the ‘canonical’ NFW profile. Wherever uncertainties in the flux are available, we use the 1-σ upper limit.

6.5.1 Gamma Rays

The isotropic diffuse gamma-ray flux will have contributions from both galactic and extragalactic dark matter annihilation. Although the galactic signal is expected to have a large directional dependence, there will be an underlying isotropic component, equal to the halo signal looking directly away from the Galactic center, where the $\mathcal{J}$ parameter defined in Eqn. 1.7 is lowest [2]. We include both contributions when computing constraints, though the galactic flux dominates over the extragalactic for the parameters of interest.

In order to calculate the cosmic annihilation signal, we follow the technique set out in Section 2.2.2. The isotropic gamma-ray flux from DM annihilations throughout the universe is given by Eqn. 2.8. As we are adopting the NFW profile, the normalization of the cosmic clustering parameter defined in Section 2.2.2 is $f_0 \simeq 5 \times 10^4$.

For Galactic annihilation, we again follow the technique from Section 2.2.1. The flux per steradian of gamma-rays from Galactic DM annihilation, in a direction at an angle ψ from the Galactic Center, is given in Eqn. 2.4. Since we are calculating the isotropic signal, we use the minimum value for $\mathcal{J}(\psi)$, corresponding to $\mathcal{J}(180°)$, shown in Fig. 1.3, once again adopting the NFW profile. As usual, we do not include the effects of any substructure.

The Extragalactic Gamma-Ray Background (EGB) reported by Fermi in [94] is the isotropic component of the diffuse gamma-ray flux, with a number of potential contributing sources. (See Section 1.3.4 for a description of the satellite). It is obtained by subtracting the components of the gamma-ray flux with known origin from the total flux, observed away from the galactic disk (Galactic latitude $|b| \geq 10°$).

Hence, it is a likely flux to contain a contribution from either galactic or extragalactic DM annihilation. We compare our calculated isotropic signal, from both cosmic and Galactic annihilation, to this isotropic flux. We do this for each data energy bin, integrating the signal over the width of each bin in turn. Our resulting upper limit on $\langle v\sigma\rangle$ is reported in Figure 6.4.

6.5.2 Electrons and Positrons

The flux of positrons (or electrons) at Earth from dark matter annihilation depends both on the propagation of the positrons through the turbulent galactic magnetic fields, and energy losses of the particles. This is governed by the diffusion-energy loss equation,

$$\frac{\partial f}{\partial t} - K(E)\cdot\nabla^2 f - \frac{\partial}{\partial E}\left(b(E)f\right) = Q, \tag{6.17}$$

where f is the number density of positrons per unit energy, $K(E)$ is the diffusion parameter which governs transport through the magnetic fields, $b(E)$ is the net energy loss rate, and Q is the source function,

$$Q = \frac{1}{2}\left(\frac{\rho}{m_\chi}\right)^2 \langle v\sigma\rangle \frac{dN_e}{dE}. \tag{6.18}$$

The flux per steradian at Earth is related to the positron number density at Earth $f_\odot$ via

$$\frac{d\Phi_e}{dE} = \frac{v_e\, f_\odot}{4\pi}, \tag{6.19}$$

where $v_e \simeq c$ in the energy regime we consider.

There are several alternative methods to finding f. One option is the GALPROP code, [285, 286], which solves Eqn. 6.17 numerically using a Crank-Nicholson method [285]. We instead opt for a semi-analytic solution to Eqn. 6.17, as done in e.g. Refs. [287, 288, 289]. To do this, simplifying assumptions have to be made. We adopt the same notation and set of assumptions as e.g. Ref [207]. It is reasonable to assume that the positron density is currently in equilibrium, and so the term $\partial f/\partial t$ is dropped from Eqn. 6.17. The diffusion parameter is assumed to be constant in space within the diffusion zone, but to follow a power law in energy, $K(E) = K_0(E/\mathrm{GeV})^\delta$. The energy loss of the positrons is mainly due to synchrotron radiation due to interaction with the interstellar magnetic field, and inverse Compton scattering off the cosmic microwave background and diffuse infrared starlight. With an average energy density of the Galactic magnetic field, cosmic microwave background, and diffuse starlight of 0.2, 0.3 and 0.6 eV cm^{-3} respectively, the loss rate is [287]

$$b(E) \simeq 10^{-16}(E/\mathrm{GeV})^2\mathrm{GeVs}^{-1}. \tag{6.20}$$

The diffusion zone of the Galaxy is generally modelled as a slab-like cylinder of radius $R = 20$ kpc and thickness $2L$, where L is commonly taken to be a value between 2 and 15 kpc.

The semi-analytic solution to the diffusion-energy loss equation, converted into a flux of positrons at Earth using Eqn. 6.19, can then be parameterised as [207]

$$\frac{d\Phi_e(E)}{dE} = \frac{\langle v\sigma\rangle\, \rho_\odot^2 c}{8\pi m_\chi^2 b(E)} \int_E^{m_\chi} dE' \frac{dN_e}{dE} I\left(\lambda_D\left(E, E'\right)\right), \tag{6.21}$$

where $I\left(\lambda_D\left(E, E'\right)\right)$ is the "halo function", $\lambda_D\left(E, E'\right)$ is the diffusion length between two energies E, E', and we recall $\rho_\odot$ is the local DM density. The "halo function" $I\left(\lambda_D\left(E, E'\right)\right)$ is an astrophysical parameter which encodes the dependence of the flux on the dark matter density profile, and on the model of positron diffusion and propagation. We use the numerical fit to $I\left(\lambda_D\left(E, E'\right)\right)$ from [207],

$$I\left(\lambda_D\left(E, E'\right)\right) = a_0 + a_1 \tanh\left(\frac{b_1 - \ell}{c_1}\right)\left[a_2 \exp\left(-\frac{(\ell - b_2)^2}{c_2}\right) + a_3\right], \tag{6.22}$$

where $\ell = \log_{10}\left(\lambda_D/\mathrm{kpc}\right)$. There is a degree of uncertainty in this function. Table 6.1 shows three choices of diffusion parameters from Ref. [288], where the 'min' and 'max' sets lead to smaller and larger fluxes respectively, and the 'med' set leads to an intermediate flux. The table also shows the fit parameters for use in Eqn. 6.22, corresponding to these three diffusion scenarios for the NFW DM density profile, from Ref [207]. We focus on the 'med' diffusion parameter set, and as usual, the NFW DM density profile, while while also showing results in the 'min' and 'max' scenarios.

	MIN	MED	MAX
L [kpc]	1	4	15
δ	0.55	0.70	0.46
K_0 [kpc^2 / Myr]	0.00595	0.0112	0.0765
a_0	0.500	0.502	0.502
a_1	0.774	0.621	0.756
a_2	-0.448	0.688	1.533
a_3	0.649	0.806	0.672
b_1	0.096	0.891	1.205
b_2	192.8	0.721	0.799
c_1	0.211	0.143	0.155
c_2	33.88	0.071	0.067

Table 6.1: Electron/positron diffusion parameters for use in Eqn. 6.22.

Our signal is then compared with the total $e^+ + e^-$ flux reported by the Fermi collaboration [125] to find an upper limit on $\langle v\sigma\rangle$, by demanding the signal integrated over the width of an energy bin be less than the total observed flux in that bin,

$$(\Phi_{e^+} + \Phi_{e^-})^{\mathrm{signal}} = 2\,\Phi_{e^+}^{\mathrm{signal}} \lesssim \Phi_{e^+ + e^-}^{\mathrm{obs}} . \tag{6.23}$$

We can also combine our positron flux with the Fermi data to find the positron fraction from dark matter annihilation. We compare this with the PAMELA data [126] for the positron fraction (f_{e^+}) to find an alternative upper limit on $\langle v\sigma\rangle$ by demanding

$$\frac{\Phi_{e^+}}{\Phi_{e^+ + e^-}^{\mathrm{obs}}} \leq f_{e^+} . \tag{6.24}$$

See Section 1.3.3 for a description of the PAMELA satellite, and Section 1.3.6 for a discussion of the PAMELA and Fermi positron data, and possible interpretations. We compare the DM-related positron fraction with the observed PAMELA fraction in each of the four energy bins where the Fermi energy range overlaps the PAMELA energy range, integrating the DM-signal and observed Fermi fluxes over the width of the PAMELA energy bins. For this, we use the simple power-law fit to the Fermi data, valid between around 20 GeV and 1 TeV [140],

$$\begin{aligned} \frac{d\Phi^{\rm obs}_{e^+ + e^-}}{dE} &= (175.40 \pm 6.09) \times 10^{-4}\,({\rm GeV\,cm^2\,s\,sr})^{-1} \\ &\times \; (E/{\rm GeV})^{(-3.045 \pm 0.008)}\,. \end{aligned} \tag{6.25}$$

Results using the 'min', 'med' and 'max' diffusion parameter sets are reported in Figs. 6.4, 6.5 and 6.6 respectively.

6.5.3 Protons and Antiprotons

The antiproton (or proton) flux at Earth has a similar functional form to that for positrons, except that the energy losses for the antiprotons as they propagate to Earth are negligible, since $m_p \gg m_e$. Because the energy for the antiprotons is the same as the injection energy, there is no need for an integral over energies at production. We do not include the effect of energy loss due to scattering interactions, or the solar modulation effect, both of which are only relevant at low energies. We again use the semi-analytic function from [207] to calculate the proton and antiproton signals at Earth from DM annihilation,

$$\frac{d\Phi_p(K)}{dK} = \frac{\langle v\sigma\rangle\, \rho_\odot^2\, v}{8\pi m_\chi^2} R(K) \tag{6.26}$$

where K is the kinetic energy of the (anti)-proton, and $R(K)$ is an astrophysics parametrization playing a similar role to $I\left(\lambda_D\left(E, E'\right)\right)$ from Section 6.5.2. Ref. [207] provides a numerical fit to $R(K)$ for several sets of propagation parameters from Ref. [290],

$$\log[R(K)/{\rm Myr}] = a_0 + a_1\,\tau + a_2\,\tau^2 + a_3\,\tau^3 + a_4\,\tau^4, \tag{6.27}$$

where $\tau = \log[K/{\rm GeV}]$ and diffusion parameters are shown in Table 6.2. We again focus on the 'med' parameter set, with the NFW DM density profile, while also showing results using the 'min' and 'max' sets.

	MIN	MED	MAX
L [kpc]	1	4	15
δ	0.85	0.70	0.46
K_0 [kpc^2 / Myr]	0.0016	0.0112	0.0765
$V_{\rm conv}$ [km/s]	13.5	12	5
a_0	0.913	1.860	2.740
a_1	0.601	0.517	-0.127
a_2	-0.309	-0.293	-0.113
a_3	-0.036	-0.0089	0.0169
a_4	0.0122	0.0070	-0.0009

Table 6.2: (anti)proton diffusion parameters for use in Eqn. 6.27.

We compare our antiproton flux with the total antiproton flux reported by the PAMELA collaboration [270], energy bin by energy bin. We can also constrain the cross section by demanding the ratio $\bar{p}/p$ due to antiprotons from DM annihilation not exceed the PAMELA $\bar{p}/p$ ratio [127, 270]. This comparison requires the observed proton flux. Following [83], we use the nucleon flux from [291], $\frac{d\Phi_p^{\rm obs}}{dE} \approx 0.79 \times 1.8(E/\mathrm{GeV})^{-2.7}\ (\mathrm{cm}^2\,\mathrm{s}\,\mathrm{GeV})^{-1}$, where 0.79 is the proton fraction of the total nucleon flux. We then simply demand $\Phi_{\bar{p}}/\Phi_p^{\rm obs} \lesssim f_{\bar{p}/p}$, where $f_{\bar{p}/p}$ is the PAMELA antiproton/proton flux ratio given in [270]. Energy bins have been handled in the same way as the positron case, giving us the upper limit on $\langle v\sigma\rangle$ shown in Figs. 6.4, 6.5 and 6.6.

6.5.4 Neutrinos

As with the gamma-ray flux, the isotropic neutrino flux will include a contribution from both cosmic and galactic dark matter annihilation. We make the approximation that 1/3 of all produced neutrinos will be observed as muon neutrinos,

$$\frac{dN_{\nu_\mu}}{dE} = \frac{1}{3}\frac{dN_\nu}{dE}. \tag{6.28}$$

Note that the neutrino spectrum in Fig. 6.3 includes primary electron neutrinos, and all flavors of secondary neutrinos. We then compare the $\nu_\mu + \bar{\nu}_\mu$ signal from dark matter annihilation with the atmospheric $\nu_\mu + \bar{\nu}_\mu$ flux, using the same technique as Ref. [2]. The calculation of the neutrino signal is the same as for gamma rays, except neutrinos do not suffer from attenuation in the energy range we consider, so that the cosmic flux becomes

$$\begin{aligned} \frac{d\Phi_\nu}{dE} &= \frac{\langle v\sigma\rangle}{2}\frac{c}{4\pi H_0}\frac{\rho_{\rm av}^2}{m_\chi^2} \\ &\times \int_0^{z_{up}} \frac{f(z)(1+z)^3}{h(z)}\frac{dN_\nu(E')}{dE'}dz\,. \end{aligned} \tag{6.29}$$

We compare the signal with the observed flux, integrating both over an energy bin width of $\Delta \log E = 0.3$. As expected, the resulting upper limit on the cross section, $\langle v\sigma\rangle \lesssim O(10^{-20})\,\mathrm{cm^3 s^{-1}}$, is significantly weaker than those for the other annihilation products considered, and is thus not reported in Fig. 6.4. Accordingly, the assumptions we made in this subsection concerning neutrino flavors are moot.

6.6 Discussion

Fig. 6.4 collects our upper limits on the bremsstrahlung cross section $\langle v\sigma\rangle_{\rm Brem}$, as calculated in the previous sections. The constraint from the antiproton ratio is stronger than that from the positron data by a factor of ~ 5. Nature provides a unique value for $\langle v\sigma\rangle$. Therefore, if the bremsstrahlung process saturates the allowed antiproton limit, then the same process produces positrons at a rate down from the observed value by about a factor of 5.[1] Conversely, if the observed positron fraction were attributed to the bremsstrahlung process, then the same process would overproduce antiprotons by about a factor of 5.

---

[1] Note that we have not compared the spectral shapes of the DM signals with those of the observed fluxes, nor tried to *fit* the data.

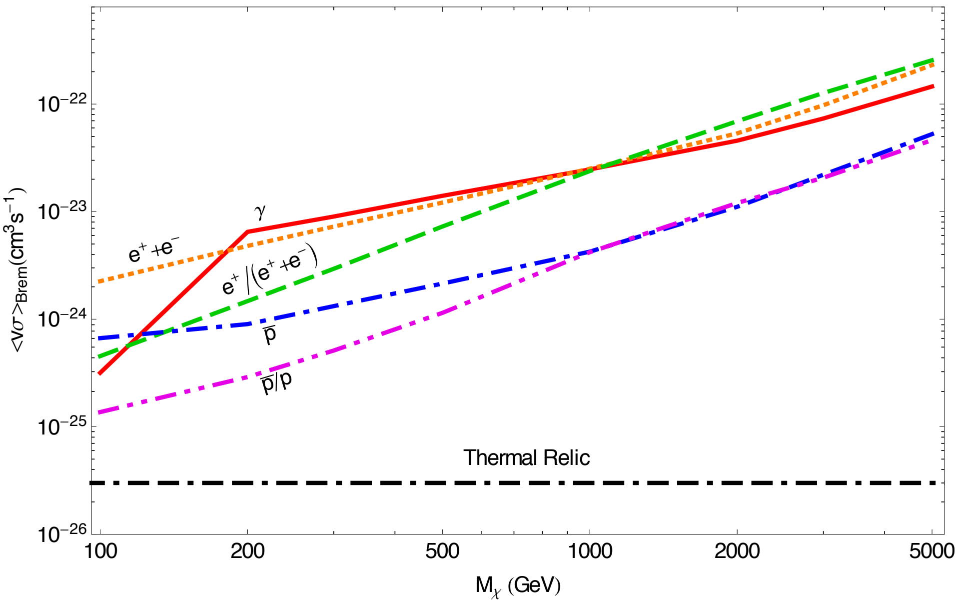

Figure 6.4: Upper limits on $\langle v\sigma\rangle_{\rm brem}$ using the 'med' diffusion parameter set. Shown are constraints based on gamma rays (solid, red), $e^+ + e^-$ flux (dots, orange), $e^+/(e^+ + e^-)$ ratio (dashes, green), $\bar{p}$ flux (dash-dots, blue), and $\bar{p}/p$ ratio (dot-dot-dashes, purple). Flux data are from Fermi, PAMELA and the PDG. Also shown for comparison is the expected cross section for thermal relic dark matter, $3 \times 10^{-26}\,{\rm cm}^3\,/{\rm s}$ (dash-dash-dots, black).

It is important to note that the observed antiproton flux and ratio are well reproduced by standard astrophysical processes, leaving little room for a dark matter contribution.[2] We have not attempted to model this standard background, so constraints from antiprotons are likely to be significantly stronger than presented here.

Annihilation to $\mu^+\mu^-$ or $\tau^+\tau^-$ is not as helicity suppressed as to electrons. Even so, the helicity factors which suppress the s-wave are $(m_\mu/m_\chi)^2 \simeq 10^{-7} \times (m_\chi/300\,{\rm GeV})^{-2}$ and $(m_\tau/m_\chi)^2 \simeq 3 \times 10^{-5} \times (m_\chi/300\,{\rm GeV})^{-2}$, which are compa-

---

[2] Reference [292] notes that a highly anisotropic diffusion model, as might be invoked to accommodate galactic winds, may suppress the antiproton flux to a value possibly below the PAMELA flux. We do not consider anisotropic diffusion in this work.

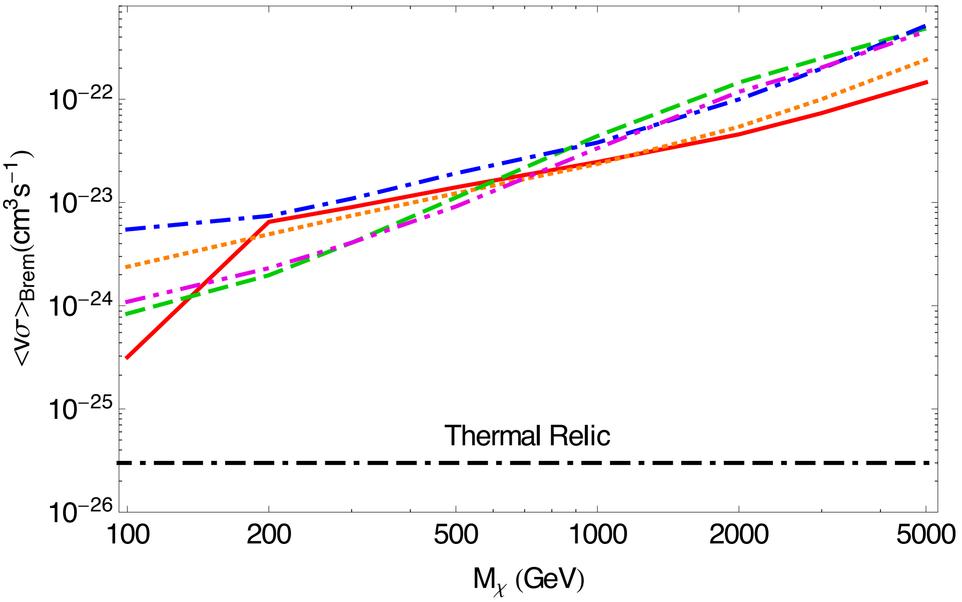

Figure 6.5: As for Fig. 6.4, using the 'min' diffusion parameter sets.

rable to the factor by which the p-wave is velocity suppressed, $v^2 \sim 10^{-6}$. Since bremsstrahlung overcomes both suppressions, it can also be important for annihilation to muons and taus. (And, of course, any helicity suppression is especially stringent for annihilation to ν_μ and ν_τ, as $m_\nu \simeq 0$.) In the case of relatively light dark matter annihilating to taus, the helicity suppression is not as pronounced. Furthermore, W/Z bremsstrahlung may be kinematically forbidden. In any case, we note that annihilation to τ can never be purely leptophilic, as the τ has significant hadronic decay modes.

Note that in the model we consider, emission of photons or massive gauge bosons will lift helicity suppression only if the dark matter and scalar exchange particles, χ and η, are nearly degenerate in mass (such as the co-annihilation region of mSUGRA). In the present work we consider such a region of parameter space. Specifically, we present results for $\mu = (m_\eta/m_\chi)^2 = 1.2$, though our conclusions remain valid for any value of μ where the bremsstrahlung processes dominate the 2 to 2 body processes. As we saw in Section 5.3, the rates for these two processes

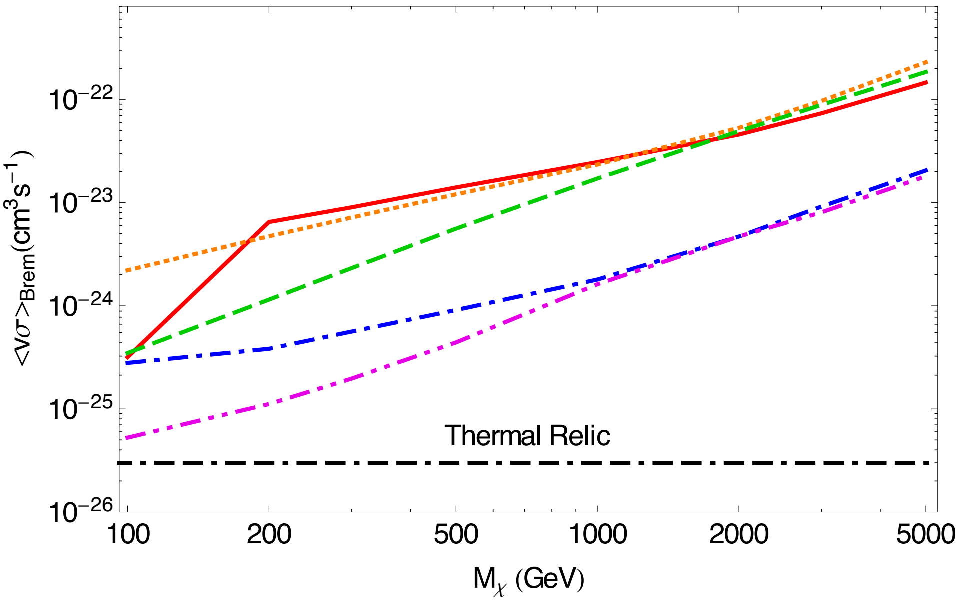

Figure 6.6: As for Fig. 6.4, using the 'max' diffusion parameter sets.

become comparable at $\mu \sim 10$.

Consider now scenarios where dark matter annihilation to a lepton pair is *not* helicity suppressed. As examples, one may have Majorana dark matter annihilating via an exchange of a pseudoscalar or scalar (the latter is still velocity suppressed at the dark matter vertex) or Dirac dark matter annihilating via the exchange of a vector, or one may have scalar dark matter annihilations. In these cases, there will still be a signal from electroweak bremsstrahlung emission [83, 84, 197], although it will no longer be the dominant channel. Even so, the W/Z decay products can still lead to restrictive constraints. Ref. [83] considered an example (exchange of a scalar) where EW bremsstrahlung makes only a subdominant contribution to the total dark matter annihilation rate. In this model, the main contribution to the annihilation rate comes from the 2-body annihilation channels, thus the monoenergetic $e^\pm$ and neutrino fluxes dwarf the gauge boson fragmentation products. Nonetheless, Ref. [83] found that the antiproton data still provide the most stringent cross section constraints for certain parameters. Note however, that the models of [83, 84] explicitly break gauge invariance. A detailed, model-independent, treatment of weak corrections may be found in Ref. [197].

It should be noted that the results presented here are not due to an exhaustive survey of all possible dark matter profiles and parameters. Uncertainties arise from the various choices made in order to present illustrative results. In most cases, we have made conservative choices for these parameters such that alterations to these selections should strengthen the results. In calculating the flux of protons, antiprotons, electrons and positrons, all the astrophysical parameters are encoded into a numerically-fit function [207] with propagation parameters which are consistent with a 'median' flux [290]. However, by assuming alternate parameters, e.g. from the 'max' or 'min' flux scenarios, our results may be strengthened or weakened by up to an order of magnitude, as shown in Figs. 6.5 and 6.6. Our conclusions hold in all cases considered, but for the extreme choice of 'min' diffusion parameter set, where the $e^+/(e^+ + e^-)$ limits become comparable to those for $\bar{p}/p$ and the $e^+ + e^-$ limits become comparable to those for gamma rays.

Obviously, the choice of profile can have a large effect on the parameter ranges, and we have adopted the NFW profile with $\rho_\odot = 0.39$ GeV/cm^{-3} throughout this work. If one considers non-spherical profiles or dark discs then the uncertainty in the value of the local dark matter density may be expanded to accommodate a value between 0.2 GeV/cm^{-3} and 0.7 GeV/cm^{-3}[31]. Note, however, that changes to the DM profile would move all the predicted fluxes, and thus the corresponding cross section constraints, in the same direction. As discussed in Section 2.2.2, for the calculation of the extragalactic fluxes, the cosmic source clustering factor can vary by an order of magnitude depending on the profile and inclusion or exclusion of subhalos. This would lead to tighter constraints coming from the gamma-ray signals.

We have also neglected the signals produced by inverse Compton scattering (gamma rays) and synchrotron radiation (radiowaves) of the electrons and positrons as they propagate in the galaxy (see, e.g., Ref. [293, 294]). Note, however, that these effects are properly included in the electron energy loss formalism we adopt. We expect the gamma rays produced directly from the annihilations to dominate the constraints. Additional gamma rays from inverse Compton would only strengthen our results (but make them less robust).

6.7 Conclusions

If dark matter is Majorana in nature, then its annihilation to fermions may be suppressed due to helicity considerations. However, when the dark matter mass is greater than $m_W/2$, both electroweak and photon bremsstrahlung may lift this suppression, thereby becoming the dominant channel for dark matter annihilation. This permits the indirect detection of models for which the annihilation cross section would otherwise be too suppressed to be of interest. Subsequent decay of the emitted W and Z gauge boson will produce fluxes of electrons, positrons, neutrinos, hadrons, and gamma rays. The aim of the present work has been to study the spectra of these particles as a tool for indirect detection of dark matter. By comparing these fluxes to cosmic ray data we have been able to constrain the dark matter annihilation cross-section in such models. From these constraints we find that the observational data pertaining to the flux of antiprotons combined with those of positrons make it difficult for helicity suppressed $2 \to 2$ leptophilic dark matter annihilation to be the source of the recently detected cosmic ray anomalies. For these models, the bremsstrahlung processes dominate. The primary culprit is the hadronization of the gauge bosons, which leads to a significant antiproton flux. This result highlights the difficulty of producing lepton-only final states even in a model expressly designed for just such a purpose with $2 \to 2$ annihilation.

7

Conclusion

Despite the now overwhelming evidence for the existence of Dark Matter, we still have little idea of its fundamental properties. Of particular interest is the self-annihilation cross section, which can in principle lead to an observable flux of standard model particles produced via dark matter annihilation in the Universe today.

In Chapter 2, we use gamma-ray data from observations of the Milky Way, Andromeda (M31), and the cosmic background as an upper limit on the flux due to DM annihilation, and compare this with the expected annihilation signal in order to place conservative upper limits on the dark matter self-annihilation cross section to monoenergetic gamma rays, $\langle v\sigma \rangle_{\gamma\gamma}$, over a wide range of dark matter masses. We use a conservative branching ratio of $Br(\gamma\gamma) \gtrsim 10^{-4}$ to define upper limits on the total cross section, although most of our limits on $\langle v\sigma \rangle_{\gamma\gamma}$ are effectively valid for any annihilation spectrum which produces at least two gamma rays with energies within a factor of ~ 2 of the DM mass. Large uncertainties are introduced via the poorly constrained dark matter density, both within our galaxy and on cosmic scales. We make conservative choices in these astrophysical parameters such that our constraints remain robust.

Leptophilic models have received much attention since the recent observation of an apparent excess in the positron flux, without an accompanying antiproton excess.

In Chapter 3, we examine such a leptophilic annihilation channel, $\chi\chi \to \ell^+\ell^-$, utilizing some of the techniques developed in Chapter 2. This final state is necessarily accompanied by gamma rays, produced via radiative corrections. Internal bremsstrahlung from the final state particles can produce hard gamma rays up to the dark matter mass, with an approximately model-independent spectrum. Focusing on annihilation into electrons, we again compute robust upper bounds on the dark matter self annihilation cross section, $\langle v\sigma\rangle_{e^+e^-}$, using gamma ray data from the Milky Way spanning a wide range of energies, $\sim 10^{-3} - 10^4$ GeV. We also compute corresponding bounds for the other charged leptons. We again make conservative assumptions about the astrophysical inputs, and demonstrate how our derived bounds would be strengthened if stronger assumptions about these inputs are adopted. The fraction of hard gamma rays near the endpoint accompanying annihilation to e^+e^- is only a factor of $\lesssim 10^2$ lower than for annihilation directly to monoenergetic gamma rays. The bound on $\langle v\sigma\rangle_{e^+e^-}$ is thus weaker than that for $\langle v\sigma\rangle_{\gamma\gamma}$ by this same factor. The upper bounds on the annihilation cross sections to gamma rays and charged leptons are compared with an upper bound on the *total* annihilation cross section defined by neutrinos.

Even in models with annihilation solely into neutrinos, non-leptonic final states will inevitably be produced through electroweak bremsstrahlung processes $\chi\chi \to \bar{\nu}\nu Z$ and $\chi\chi \to \bar{\nu}eW$. These modes lead to electromagnetic and hadronic showers and further constraints on the DM annihilation cross-section. In Chapter 4 we present an explicit calculation of the branching ratios for the electroweak bremsstrahlung processes $\chi\chi \to \bar{\nu}\nu Z$ and $\chi\chi \to \bar{\nu}eW$. In addition to annihilation, our calculations are also applicable to the case of dark matter decay.

Significantly, while many dark matter models feature a helicity suppressed annihilation rate to fermions, bremsstrahlung processes can remove this helicity suppression. It has been known for some time that photon bremsstrahlung may significantly boost DM annihilation yields, and we show in Chapter 5 that electroweak bremsstrahlung of W and Z gauge bosons can also lift suppression such that the branching ratios $\mathrm{Br}(\ell\nu W)$, $\mathrm{Br}(\ell^+\ell^- Z)$, and $\mathrm{Br}(\bar{\nu}\nu Z)$ dominate over $\mathrm{Br}(\ell^+\ell^-)$ and $\mathrm{Br}(\bar{\nu}\nu)$. We find this is most significant in the limit where the dark matter mass is nearly degenerate with the mass of the boson which mediates the annihilation process. Electroweak bremsstrahlung has important phenomenological consequences both for the magnitude of the total dark matter annihilation cross section and for the character of the astrophysical signals for indirect detection. Given that the W and Z gauge bosons decay dominantly via hadronic channels, it is impossible to produce final state leptons without accompanying protons, antiprotons, and gamma rays.

This has especially important implications in leptophilic models designed to produce leptons without overproducing gamma rays or hadrons in order to explain the observed positron excess without violating bounds on the antiproton flux. Models where suppression is lifted have large branching ratios to massive gauge bosons, whose decay products will undergo hadronization leading to an antiproton flux. In Chapter 6, we calculate the signal of both primary and secondary gamma rays, leptons and hadrons in our example leptophilic model, and apply techniques similar to those in Chapter 2 to place an upper limit on the self-annihilation cross section. We compare the gamma-ray signal with the Fermi isotropic gamma-ray background. For charged final states, we apply the appropriate diffusion-energy loss equations to calculate the signal at Earth, which we compare with Fermi and PAMELA electron/positron and proton/antiproton flux data. We find that for most choices of the diffusion parameters, the constraints derived from the antiproton and/or gamma-ray data are significantly stronger than those from the electron/positron data, making it difficult for this leptophilic model to act as an explanation for the positron excess without overproducing other particles.

Publications

1. G. D. Mack, T. D. Jacques, J. F. Beacom, N. F. Bell and H. Yuksel,
   “Conservative Constraints on Dark Matter Annihilation into Gamma Rays,”
   Phys. Rev. D **78**, 063542 (2008) [arXiv:0803.0157 [astro-ph]].
2. N. F. Bell, J. B. Dent, T. D. Jacques and T. J. Weiler,
   “Electroweak Bremsstrahlung in Dark Matter Annihilation,”
   Phys. Rev. D **78**, 083540 (2008) [arXiv:0805.3423 [hep-ph]].
3. N. F. Bell and T. D. Jacques,
   “Gamma-ray Constraints on Dark Matter Annihilation into Charged Particles,”
   Phys. Rev. D **79**, 043507 (2009) [arXiv:0811.0821 [astro-ph]].
4. N. F. Bell, J. B. Dent, T. D. Jacques and T. J. Weiler,
   “W/Z Bremsstrahlung as the Dominant Annihilation Channel for Dark Matter,”
   Phys. Rev. D **83**, 013001 (2011) [arXiv:1009.2584 [hep-ph]].
5. N. F. Bell, J. B. Dent, T. D. Jacques and T. J. Weiler,
   “Dark Matter Annihilation Signatures from
   Electroweak Bremsstrahlung,”
   arXiv:1101.3357 [hep-ph]
6. N. F. Bell, J. B. Dent, A. J. Galea, T. D. Jacques, L. M. Krauss and T. J. Weiler,
   “W/Z Bremsstrahlung as the Dominant Annihilation Channel for Dark Matter, Revisited,”
   arXiv:1104.3823 [hep-ph]

Bibliography

[1] M. Persic, P. Salucci, and F. Stel, Mon.Not.Roy.Astron.Soc. **281**, 27 (1996), arXiv:astro-ph/9506004.

[2] H. Yuksel, S. Horiuchi, J. F. Beacom, and S. Ando, Phys. Rev. **D76**, 123506 (2007), arXiv:0707.0196.

[3] Y. Sofue and V. Rubin, Ann.Rev.Astron.Astrophys. **39**, 137 (2001), arXiv:astro-ph/0010594.

[4] F. Zwicky, Helv. Phys. Acta **6**, 110 (1933).

[5] F. Zwicky, Astrophys. J. **86**, 217 (1937).

[6] J. Tyson, G. P. Kochanski, and I. P. Dell'Antonio, Astrophys.J. **498**, L107 (1998), arXiv:astro-ph/9801193.

[7] http://hubble.nasa.gov.

[8] M. Bartelmann and P. Schneider, Phys. Rept. **340**, 291 (2001), arXiv:astro-ph/9912508.

[9] D. Clowe *et al.*, Astrophys. J. **648**, L109 (2006), arXiv:astro-ph/0608407.

[10] http://chandra.nasa.gov.

[11] M. J. Jee *et al.*, Astrophys.J. **661**, 728 (2007), arXiv:0705.2171.

[12] M. Bradac *et al.*, (2008), arXiv:0806.2320.

[13] MACHO Collaboration, C. Alcock *et al.*, Astrophys.J. **542**, 281 (2000), arXiv:astro-ph/0001272.

[14] EROS-2 Collaboration, P. Tisserand *et al.*, Astron.Astrophys. **469**, 387 (2007), arXiv:astro-ph/0607207.

[15] W. Hu and S. Dodelson, Ann. Rev. Astron. Astrophys. **40**, 171 (2002), arXiv:astro-ph/0110414.

[16] N. Jarosik *et al.*, Astrophys. J. Supp. **192**, 14 (2011), arXiv:1001.4744.

[17] www.sdss.org.

[18] D. Larson *et al.*, (2010), arXiv:1001.4635.

[19] P. Gondolo and G. Gelmini, Nucl. Phys. **B360**, 145 (1991).

[20] G. Bertone, D. Hooper, and J. Silk, Phys. Rept. **405**, 279 (2005), arXiv:hep-ph/0404175.

[21] S. Hannestad, A. Mirizzi, and G. Raffelt, JCAP **0507**, 002 (2005), arXiv:hep-ph/0504059.

[22] M. Kaplinghat, L. Knox, and M. S. Turner, Phys. Rev. Lett. **85**, 3335 (2000), arXiv:astro-ph/0005210.

[23] M. Boylan-Kolchin, V. Springel, S. D. M. White, A. Jenkins, and G. Lemson, Mon. Not. Roy. Astron. Soc. **398**, 1150 (2009), arXiv:0903.3041.

[24] J. Bond, G. Efstathiou, and J. Silk, Phys.Rev.Lett. **45**, 1980 (1980).

[25] L. Bergstrom, P. Ullio, and J. H. Buckley, Astropart. Phys. **9**, 137 (1998), arXiv:astro-ph/9712318.

[26] J. N. Bahcall and R. M. Soneira, Astrophys. J. Suppl. **44**, 73 (1980).

[27] A. V. Kravtsov, A. A. Klypin, J. S. Bullock, and J. R. Primack, Astrophys. J. **502**, 48 (1998), arXiv:astro-ph/9708176.

[28] J. F. Navarro, C. S. Frenk, and S. D. M. White, Astrophys. J. **462**, 563 (1996), arXiv:astro-ph/9508025.

[29] B. Moore, T. R. Quinn, F. Governato, J. Stadel, and G. Lake, Mon. Not. Roy. Astron. Soc. **310**, 1147 (1999), arXiv:astro-ph/9903164.

[30] R. Catena and P. Ullio, (2009), arXiv:0907.0018.

[31] M. Weber and W. de Boer, (2009), arXiv:0910.4272.

[32] P. Salucci, F. Nesti, G. Gentile, and C. F. Martins, (2010), arXiv:1003.3101.

[33] I. Cholis and L. Goodenough, JCAP **1009**, 010 (2010), arXiv:1006.2089.

[34] A. W. Graham, D. Merritt, B. Moore, J. Diemand, and B. Terzic, Astron. J. **132**, 2685 (2006), arXiv:astro-ph/0509417.

[35] J. F. Navarro *et al.*, (2008), arXiv:0810.1522.

[36] J. Diemand, M. Kuhlen, and P. Madau, Astrophys. J. **657**, 262 (2007), arXiv:astro-ph/0611370.

[37] J. C. Fabris, I. L. Shapiro, and F. Sobreira, JCAP **0902**, 001 (2009), arXiv:0806.1969.

[38] M. Abdelqader and F. Melia, Mon. Not. Roy. Astron. Soc. **388**, 1869 (2008), arXiv:0806.0602.

[39] A. H. G. Peter, C. E. Moody, and M. Kamionkowski, Phys. Rev. **D81**, 103501 (2010), arXiv:1003.0419.

[40] E. D'Onghia, V. Springel, L. Hernquist, and D. Keres, Astrophys. J. **709**, 1138 (2010), arXiv:0907.3482.

[41] A. Schneider, L. Krauss, and B. Moore, Phys. Rev. **D82**, 063525 (2010), arXiv:1004.5432.

[42] L. Bergstrom, Rept. Prog. Phys. **63**, 793 (2000), arXiv:hep-ph/0002126.

[43] G. Jungman, M. Kamionkowski, and K. Griest, Phys. Rept. **267**, 195 (1996), arXiv:hep-ph/9506380.

[44] F. D. Steffen, Eur. Phys. J. **C59**, 557 (2009), arXiv:0811.3347.

[45] J. Einasto, (2009), arXiv:0901.0632.

[46] H. Baer, E.-K. Park, and X. Tata, New J. Phys. **11**, 105024 (2009), arXiv:0903.0555.

[47] L. Bergstrom, New J. Phys. **11**, 105006 (2009), arXiv:0903.4849.

[48] M. Maniatis, Int. J. Mod. Phys. **A25**, 3505 (2010), arXiv:0906.0777.

[49] G. L. Kane, C. F. Kolda, L. Roszkowski, and J. D. Wells, Phys. Rev. **D49**, 6173 (1994), arXiv:hep-ph/9312272.

[50] S. P. Martin, (1997), arXiv:hep-ph/9709356.

[51] U. Amaldi, W. de Boer, and H. Furstenau, Phys.Lett. **B260**, 447 (1991).

[52] V. D. Barger, M. S. Berger, and P. Ohmann, Phys. Rev. **D49**, 4908 (1994), arXiv:hep-ph/9311269.

[53] A. Brignole, L. E. Ibanez, and C. Munoz, (1997), arXiv:hep-ph/9707209.

[54] M. Beltran, D. Hooper, E. W. Kolb, and Z. C. Krusberg, Phys. Rev. **D80**, 043509 (2009), arXiv:0808.3384.

[55] T. Kaluza, Sitzungsber.Preuss.Akad.Wiss.Berlin (Math.Phys.) , 966 (1921).

[56] O. Klein, Z.Phys. **37**, 895 (1926).

[57] T. Appelquist, H.-C. Cheng, and B. A. Dobrescu, Phys. Rev. **D64**, 035002 (2001), arXiv:hep-ph/0012100.

[58] D. Hooper and S. Profumo, Phys.Rept. **453**, 29 (2007), arXiv:hep-ph/0701197.

[59] S. Arrenberg, L. Baudis, K. Kong, K. T. Matchev, and J. Yoo, Phys. Rev. **D78**, 056002 (2008), arXiv:0805.4210.

[60] The MiniBooNE Collaboration, A. Aguilar-Arevalo *et al.*, Phys.Rev.Lett. **105**, 181801 (2010), arXiv:1007.1150.

[61] S. Dodelson and L. M. Widrow, Phys. Rev. Lett. **72**, 17 (1994), arXiv:hep-ph/9303287.

[62] A. Boyarsky, O. Ruchayskiy, and M. Shaposhnikov, Ann. Rev. Nucl. Part. Sci. **59**, 191 (2009), arXiv:0901.0011.

[63] R. Peccei and H. R. Quinn, Phys.Rev.Lett. **38**, 1440 (1977).

[64] F. Wilczek, Phys.Rev.Lett. **40**, 279 (1978).

[65] S. Weinberg, Phys.Rev.Lett. **40**, 223 (1978).

[66] M. P. Hertzberg, M. Tegmark, and F. Wilczek, Phys. Rev. **D78**, 083507 (2008), arXiv:0807.1726.

[67] L. J. Rosenberg and K. A. van Bibber, Phys. Rept. **325**, 1 (2000).

[68] S. J. Asztalos, L. J. Rosenberg, K. van Bibber, P. Sikivie, and K. Zioutas, Ann.Rev.Nucl.Part.Sci. **56**, 293 (2006).

[69] L. Dugger, T. E. Jeltema, and S. Profumo, JCAP **1012**, 015 (2010), arXiv:1009.5988, * Temporary entry *.

[70] X.-L. Chen and M. Kamionkowski, Phys.Rev. **D70**, 043502 (2004), arXiv:astro-ph/0310473.

[71] L. Hui, Phys. Rev. Lett. **86**, 3467 (2001), arXiv:astro-ph/0102349.

[72] K. Griest and M. Kamionkowski, Phys. Rev. Lett. **64**, 615 (1990).

[73] A. Kusenko and P. J. Steinhardt, Phys. Rev. Lett. **87**, 141301 (2001), arXiv:astro-ph/0106008.

[74] J. F. Beacom, N. F. Bell, and G. D. Mack, Phys. Rev. Lett. **99**, 231301 (2007), arXiv:astro-ph/0608090.

[75] D. Fargion, R. Konoplich, M. Grossi, and M. Khlopov, Astropart. Phys. **12**, 307 (2000), arXiv:astro-ph/9809260.

[76] E. A. Baltz and L. Wai, Phys. Rev. **D70**, 023512 (2004), arXiv:astro-ph/0403528.

[77] D. P. Finkbeiner, (2004), arXiv:astro-ph/0409027.

[78] S. Palomares-Ruiz and S. Pascoli, Phys. Rev. **D77**, 025025 (2008), arXiv:0710.5420.

[79] P.-f. Yin, J. Liu, Q. Yuan, X.-j. Bi, and S.-h. Zhu, (2008), arXiv:0806.3689.

[80] S. Palomares-Ruiz, Phys. Lett. **B665**, 50 (2008), arXiv:0712.1937.

[81] Y. Gong and X. Chen, Phys. Rev. **D77**, 103511 (2008), arXiv:0802.2296.

[82] M. Kachelriess and P. D. Serpico, Phys. Rev. **D76**, 063516 (2007), arXiv:0707.0209.

[83] M. Kachelriess, P. D. Serpico, and M. A. Solberg, Phys. Rev. **D80**, 123533 (2009), arXiv:0911.0001.

[84] N. F. Bell, J. B. Dent, T. D. Jacques, and T. J. Weiler, Phys. Rev. **D78**, 083540 (2008), arXiv:0805.3423.

[85] J. B. Dent, R. J. Scherrer, and T. J. Weiler, (2008), arXiv:0806.0370.

[86] Q.-H. Cao, E. Ma, and G. Shaughnessy, Phys. Lett. **B673**, 152 (2009), arXiv:0901.1334.

[87] pamela.roma2.infn.it.

[88] http://fermi.gsfc.nasa.gov/.

[89] LAT Collaboration, W. B. Atwood *et al.*, Astrophys. J. **697**, 1071 (2009), arXiv:0902.1089.

[90] R. Essig, N. Sehgal, L. E. Strigari, M. Geha, and J. D. Simon, Phys. Rev. **D82**, 123503 (2010), arXiv:1007.4199.

[91] A. A. Abdo *et al.*, Astrophys. J. **712**, 147 (2010), arXiv:1001.4531.

[92] N. W. Evans, F. Ferrer, and S. Sarkar, Phys. Rev. **D69**, 123501 (2004), arXiv:astro-ph/0311145.

[93] A. Charbonnier *et al.*, (2011), arXiv:1104.0412.

[94] Fermi-LAT Collaboration, A. A. Abdo *et al.*, Phys. Rev. Lett. **104**, 101101 (2010), arXiv:1002.3603.

[95] Fermi-LAT Collaboration, A. A. Abdo *et al.*, JCAP **1004**, 014 (2010), arXiv:1002.4415.

[96] WMAP Collaboration, D. N. Spergel *et al.*, Astrophys. J. Suppl. **170**, 377 (2007), arXiv:astro-ph/0603449.

[97] G. Dobler and D. P. Finkbeiner, Astrophys. J. **680**, 1222 (2008), arXiv:0712.1038.

[98] D. Hooper, D. P. Finkbeiner, and G. Dobler, Phys. Rev. **D76**, 083012 (2007), arXiv:0705.3655.

[99] G. Caceres and D. Hooper, Phys. Rev. **D78**, 123512 (2008), arXiv:0808.0508.

[100] I. Cholis, G. Dobler, D. P. Finkbeiner, L. Goodenough, and N. Weiner, Phys. Rev. **D80**, 123518 (2009), arXiv:0811.3641.

[101] P. L. Biermann *et al.*, (2009), arXiv:0910.1197.

[102] M. Kaplinghat, D. J. Phalen, and K. M. Zurek, JCAP **0912**, 010 (2009), arXiv:0905.0487.

[103] D. T. Cumberbatch, J. Zuntz, H. K. K. Eriksen, and J. Silk, (2009), arXiv:0902.0039.

[104] P. Mertsch and S. Sarkar, JCAP **1010**, 019 (2010), arXiv:1004.3056.

[105] G. Dobler, D. P. Finkbeiner, I. Cholis, T. R. Slatyer, and N. Weiner, Astrophys. J. **717**, 825 (2010), arXiv:0910.4583.

[106] G. Dobler, I. Cholis, and N. Weiner, (2011), arXiv:1102.5095.

[107] L. Bouchet *et al.*, (2008), arXiv:0801.2086.

[108] J. Knodlseder *et al.*, Astron. Astrophys. **411**, L457 (2003), arXiv:astro-ph/0309442.

[109] P. Jean *et al.*, Astron. Astrophys. **407**, L55 (2003), arXiv:astro-ph/0309484.

[110] J. Knodlseder *et al.*, Astron. Astrophys. **441**, 513 (2005), arXiv:astro-ph/0506026.

[111] J. F. Beacom, N. F. Bell, and G. Bertone, Phys. Rev. Lett. **94**, 171301 (2005), arXiv:astro-ph/0409403.

[112] J. F. Beacom and H. Yuksel, Phys. Rev. Lett. **97**, 071102 (2006), arXiv:astro-ph/0512411.

[113] C. D. Dermer and R. J. Murphy, (2001), arXiv:astro-ph/0107216.

[114] P. A. Milne, J. D. Kurfess, R. L. Kinzer, and M. D. Leising, New Astron. Rev. **46**, 553 (2002), arXiv:astro-ph/0110442.

[115] G. Bertone, A. Kusenko, S. Palomares-Ruiz, S. Pascoli, and D. Semikoz, Phys. Lett. **B636**, 20 (2006), arXiv:astro-ph/0405005.

[116] M. Casse, B. Cordier, J. Paul, and S. Schanne, Astrophys. J. **602**, L17 (2004), arXiv:astro-ph/0309824.

[117] J. M. Cline, A. R. Frey, and F. Chen, (2010), arXiv:1008.1784.

[118] W. de Boer, C. Sander, V. Zhukov, A. V. Gladyshev, and D. I. Kazakov, Astron. Astrophys. **444**, 51 (2005), arXiv:astro-ph/0508617.

[119] F. W. Stecker, S. D. Hunter, and D. A. Kniffen, Astropart. Phys. **29**, 25 (2008), arXiv:0705.4311.

[120] I. V. Moskalenko and A. W. Strong, Astrophys. J. **493**, 694 (1998), arXiv:astro-ph/9710124.

[121] J. Chang *et al.*, Nature **456**, 362 (2008).

[122] PPB-BETS Collaboration, S. Torii *et al.*, (2008), arXiv:0809.0760.

[123] H.E.S.S. Collaboration, F. Aharonian *et al.*, Phys. Rev. Lett. **101**, 261104 (2008), arXiv:0811.3894.

[124] H.E.S.S. Collaboration, F. Aharonian *et al.*, Astron. Astrophys. **508**, 561 (2009), arXiv:0905.0105.

[125] Fermi LAT Collaboration, A. A. Abdo *et al.*, Phys. Rev. Lett. **102**, 181101 (2009), arXiv:0905.0025.

[126] PAMELA Collaboration, O. Adriani *et al.*, Nature **458**, 607 (2009), arXiv:0810.4995.

[127] O. Adriani *et al.*, Phys. Rev. Lett. **102**, 051101 (2009), arXiv:0810.4994.

[128] T. Kobayashi, Y. Komori, K. Yoshida, and J. Nishimura, Astrophys. J. **601**, 340 (2004), arXiv:astro-ph/0308470.

[129] L. O. Drury, F. A. Aharonian, and H. J. Volk, Astron. Astrophys. **287**, 959 (1994), arXiv:astro-ph/9305037.

[130] N. J. Shaviv, E. Nakar, and T. Piran, Phys. Rev. Lett. **103**, 111302 (2009), arXiv:0902.0376.

[131] Y. Fujita *et al.*, Phys. Rev. **D80**, 063003 (2009), arXiv:0903.5298.

[132] J. P. Ostriker and J. E. Gunn, Astrophys. J. **157**, 1395 (1969).

[133] X. Chi, E. C. M. Young, and K. S. Cheng, Astrophys. J. **459**, L83 (1995).

[134] L. Zhang and K. S. Cheng, Astron. Astrophys. **368**, 1063 (2001).

[135] D. Malyshev, I. Cholis, and J. Gelfand, Phys. Rev. **D80**, 063005 (2009), arXiv:0903.1310.

[136] D. Hooper, P. Blasi, and P. D. Serpico, JCAP **0901**, 025 (2009), arXiv:0810.1527.

[137] H. Yuksel, M. D. Kistler, and T. Stanev, Phys. Rev. Lett. **103**, 051101 (2009), arXiv:0810.2784.

[138] S. Profumo, (2008), arXiv:0812.4457.

[139] V. Barger, Y. Gao, W. Y. Keung, D. Marfatia, and G. Shaughnessy, Phys. Lett. **B678**, 283 (2009), arXiv:0904.2001.

[140] FERMI-LAT Collaboration, D. Grasso *et al.*, Astropart. Phys. **32**, 140 (2009), arXiv:0905.0636.

[141] D. Malyshev, JCAP **0907**, 038 (2009), arXiv:0905.2611.

[142] K. Kashiyama, K. Ioka, and N. Kawanaka, (2010), arXiv:1009.1141.

[143] H.-B. Hu *et al.*, (2009), arXiv:0901.1520.

[144] S. Dado and A. Dar, (2009), arXiv:0903.0165.

[145] P. Blasi, Phys. Rev. Lett. **103**, 051104 (2009), arXiv:0903.2794.

[146] P. Mertsch and S. Sarkar, Phys. Rev. Lett. **103**, 081104 (2009), arXiv:0905.3152.

[147] R. Cowsik and B. Burch, (2009), arXiv:0905.2136.

[148] B. Katz, K. Blum, and E. Waxman, (2009), arXiv:0907.1686.

[149] L. Stawarz, V. Petrosian, and R. D. Blandford, Astrophys. J. **710**, 236 (2010), arXiv:0908.1094.

[150] N. Arkani-Hamed, D. P. Finkbeiner, T. Slatyer, and N. Weiner, (2008), arXiv:0810.0713.

[151] X.-G. He, Mod. Phys. Lett. **A24**, 2139 (2009), arXiv:0908.2908.

[152] Y.-Z. Fan, B. Zhang, and J. Chang, Int. J. Mod. Phys. **D19**, 2011 (2010), arXiv:1008.4646.

[153] M. Boezio *et al.*, New J. Phys. **11**, 105023 (2009).

[154] M. Cirelli, M. Kadastik, M. Raidal, and A. Strumia, Nucl. Phys. **B813**, 1 (2009), arXiv:0809.2409.

[155] J. Diemand *et al.*, Nature **454**, 735 (2008), arXiv:0805.1244.

[156] A. Sommerfeld, Annalen der Physik **403** (1931).

[157] M. Cirelli, A. Strumia, and M. Tamburini, Nucl.Phys. **B787**, 152 (2007), arXiv:0706.4071.

[158] J. Hisano, S. Matsumoto, and M. M. Nojiri, Phys.Rev.Lett. **92**, 031303 (2004), arXiv:hep-ph/0307216.

[159] J. March-Russell, S. M. West, D. Cumberbatch, and D. Hooper, JHEP **07**, 058 (2008), arXiv:0801.3440.

[160] J. Hisano, S. Matsumoto, M. M. Nojiri, and O. Saito, Phys. Rev. **D71**, 063528 (2005), arXiv:hep-ph/0412403.

[161] T. R. Slatyer, JCAP **1002**, 028 (2010), arXiv:0910.5713.

[162] M. Kamionkowski and S. Profumo, Phys.Rev.Lett. **101**, 261301 (2008), arXiv:0810.3233.

[163] J. B. Dent, S. Dutta, and R. J. Scherrer, Phys. Lett. **B687**, 275 (2010), arXiv:0909.4128.

[164] C. Arina, F.-X. Josse-Michaux, and N. Sahu, Phys. Lett. **B691**, 219 (2010), arXiv:1004.0645.

[165] J. L. Feng, M. Kaplinghat, and H.-B. Yu, Phys. Rev. **D82**, 083525 (2010), arXiv:1005.4678.

[166] D. P. Finkbeiner, L. Goodenough, T. R. Slatyer, M. Vogelsberger, and N. Weiner, (2010), arXiv:1011.3082.

[167] D. N. Spergel, Phys. Rev. **D37**, 1353 (1988).

[168] B. Morgan, A. M. Green, and N. J. C. Spooner, Phys. Rev. **D71**, 103507 (2005), arXiv:astro-ph/0408047.

[169] C. J. Copi, J. Heo, and L. M. Krauss, Phys. Lett. **B461**, 43 (1999), arXiv:hep-ph/9904499.

[170] C. J. Copi and L. M. Krauss, Phys. Rev. **D63**, 043507 (2001), arXiv:astro-ph/0009467.

[171] XENON100 Collaboration, E. Aprile *et al.*, Phys. Rev. Lett. **105**, 131302 (2010), arXiv:1005.0380.

[172] DAMA Collaboration, R. Bernabei *et al.*, Eur. Phys. J. **C56**, 333 (2008), arXiv:0804.2741.

[173] R. Bernabei *et al.*, Eur. Phys. J. **C67**, 39 (2010), arXiv:1002.1028.

[174] CDMS-II Collaboration, Z. Ahmed *et al.*, Science **327**, 1619 (2010), arXiv:0912.3592.

[175] XENON100 Collaboration, E. Aprile *et al.*, Phys.Rev.Lett. (2011), arXiv:1104.2549.

[176] D. Hooper, J. I. Collar, J. Hall, and D. McKinsey, Phys. Rev. **D82**, 123509 (2010), arXiv:1007.1005.

[177] R. Foot, Phys. Rev. **D78**, 043529 (2008), arXiv:0804.4518.

[178] F. Petriello and K. M. Zurek, JHEP **09**, 047 (2008), arXiv:0806.3989.

[179] CoGeNT Collaboration, C. Aalseth *et al.*, Phys.Rev.Lett. **106**, 131301 (2011), arXiv:1002.4703.

[180] ALEPH Collaboration, R. Barate *et al.*, Phys.Lett. **B499**, 67 (2001), arXiv:hep-ex/0011047.

[181] CDF Collaboration, T. Aaltonen *et al.*, Phys.Rev.Lett. **102**, 121801 (2009), arXiv:0811.2512.

[182] D0 Collaboration, V. Abazov *et al.*, Phys.Lett. **B660**, 449 (2008), arXiv:0712.3805.

[183] H. Baer, C. Balazs, A. Belyaev, T. Krupovnickas, and X. Tata, JHEP **06**, 054 (2003), arXiv:hep-ph/0304303.

[184] J. Goodman *et al.*, (2010), arXiv:1008.1783.

[185] J. Goodman *et al.*, Phys. Lett. **B695**, 185 (2011), arXiv:1005.1286.

[186] D. S. M. Alves, E. Izaguirre, and J. G. Wacker, (2010), arXiv:1008.0407.

[187] Atlas Collaboration, G. Aad *et al.*, (2011), arXiv:1102.2357.

[188] CMS Collaboration, V. Khachatryan *et al.*, Phys. Lett. **B698**, 196 (2011), arXiv:1101.1628.

[189] Atlas Collaboration, J. B. G. da Costa *et al.*, (2011), arXiv:1102.5290.

[190] LHC/LC Study Group, G. Weiglein *et al.*, Phys. Rept. **426**, 47 (2006), arXiv:hep-ph/0410364.

[191] L. Bergstrom, T. Bringmann, M. Eriksson, and M. Gustafsson, Phys. Rev. Lett. **94**, 131301 (2005), arXiv:astro-ph/0410359.

[192] L. Bergstrom, Phys. Lett. **B225**, 372 (1989).

[193] E. A. Baltz and L. Bergstrom, Phys. Rev. **D67**, 043516 (2003), arXiv:hep-ph/0211325.

[194] T. Bringmann, L. Bergstrom, and J. Edsjo, JHEP **01**, 049 (2008), arXiv:0710.3169.

[195] V. Berezinsky, M. Kachelriess, and S. Ostapchenko, Phys. Rev. Lett. **89**, 171802 (2002), arXiv:hep-ph/0205218.

[196] P. Ciafaloni and A. Urbano, (2010), arXiv:1001.3950.

[197] P. Ciafaloni *et al.*, (2010), arXiv:1009.0224.

[198] P. Ciafaloni *et al.*, (2011), arXiv:1104.2996.

[199] L. Bergstrom, T. Bringmann, and J. Edsjo, Phys. Rev. **D78**, 103520 (2008), arXiv:0808.3725.

[200] R. Flores, K. A. Olive, and S. Rudaz, Phys. Lett. **B232**, 377 (1989).

[201] V. Barger, Y. Gao, W. Y. Keung, and D. Marfatia, Phys. Rev. **D80**, 063537 (2009), arXiv:0906.3009.

[202] S. Rudaz and F. W. Stecker, Astrophys. J. **368**, 406 (1991).

[203] A. Bouquet, P. Salati, and J. Silk, Phys. Rev. **D40**, 3168 (1989).

[204] A. R. Pullen, R.-R. Chary, and M. Kamionkowski, Phys. Rev. **D76**, 063006 (2007), arXiv:astro-ph/0610295.

[205] P. D. Serpico and G. Zaharijas, Astropart. Phys. **29**, 380 (2008), arXiv:0802.3245.

[206] S. Profumo, Phys. Rev. **D78**, 023507 (2008), arXiv:0806.2150.

[207] M. Cirelli, R. Franceschini, and A. Strumia, Nucl. Phys. **B800**, 204 (2008), arXiv:0802.3378.

[208] M. Pospelov and A. Ritz, Phys. Rev. **D78**, 055003 (2008), arXiv:0803.2251.

[209] S. Profumo, (2011), arXiv:1105.5162.

[210] S. Matsumoto, J. Sato, and Y. Sato, (2005), arXiv:hep-ph/0505160.

[211] M. Gustafsson, E. Lundstrom, L. Bergstrom, and J. Edsjo, Phys. Rev. Lett. **99**, 041301 (2007), arXiv:astro-ph/0703512.

[212] F. Ferrer, L. M. Krauss, and S. Profumo, Phys. Rev. **D74**, 115007 (2006), arXiv:hep-ph/0609257.

[213] M. Fornasa, M. Taoso, and G. Bertone, Phys. Rev. **D76**, 043517 (2007), arXiv:astro-ph/0703757.

[214] N. Fornengo, L. Pieri, and S. Scopel, Phys. Rev. **D70**, 103529 (2004), arXiv:hep-ph/0407342.

[215] L. E. Strigari *et al.*, (2007), arXiv:0709.1510.

[216] X.-J. Bi, Nucl. Phys. **B741**, 83 (2006), arXiv:astro-ph/0510714.

[217] D. Hooper and P. D. Serpico, JCAP **0706**, 013 (2007), arXiv:astro-ph/0702328.

[218] G. Bertone, A. R. Zentner, and J. Silk, Phys. Rev. **D72**, 103517 (2005), arXiv:astro-ph/0509565.

[219] S. Horiuchi and S. Ando, Phys. Rev. **D74**, 103504 (2006), arXiv:astro-ph/0607042.

[220] L. Bergstrom, J. Edsjo, and P. Ullio, Phys. Rev. Lett. **87**, 251301 (2001), arXiv:astro-ph/0105048.

[221] P. Ullio, L. Bergstrom, J. Edsjo, and C. G. Lacey, Phys. Rev. **D66**, 123502 (2002), arXiv:astro-ph/0207125.

[222] M. H. Salamon and F. W. Stecker, Astrophys. J. **493**, 547 (1998), arXiv:astro-ph/9704166.

[223] R. C. Gilmore, P. Madau, J. R. Primack, R. S. Somerville, and F. Haardt, (2009), arXiv:0905.1144.

[224] J. R. Primack, R. S. Somerville, J. S. Bullock, and J. E. G. Devriendt, AIP Conf. Proc. **558**, 463 (2001), arXiv:astro-ph/0011475.

[225] F. W. Stecker, M. A. Malkan, and S. T. Scully, Astrophys. J. **648**, 774 (2006), arXiv:astro-ph/0510449.

[226] J. Zavala, V. Springel, and M. Boylan-Kolchin, Mon. Not. Roy. Astron. Soc. **405**, 593 (2010), arXiv:0908.2428.

[227] J. E. Taylor and J. Silk, Mon. Not. Roy. Astron. Soc. **339**, 505 (2003), arXiv:astro-ph/0207299.

[228] S. Ando, Phys. Rev. Lett. **94**, 171303 (2005), arXiv:astro-ph/0503006.

[229] http://cossc.gsfc.nasa.gov/docs/cgro/cgro/comptel.html.

[230] http://cossc.gsfc.nasa.gov/docs/cgro/cgro/egret.html.

[231] A. W. Strong, H. Bloemen, R. Diehl, W. Hermsen, and V. Schoenfelder, Astrophys. Lett. Commun. **39**, 209 (1999), arXiv:astro-ph/9811211.

[232] A. W. Strong *et al.*, Astron. Astrophys. **444**, 495 (2005), arXiv:astro-ph/0509290.

[233] http://www.mpi-hd.mpg.de/hfm/hess/hess.html.

[234] H.E.S.S. Collaboration, F. Aharonian *et al.*, Nature **439**, 695 (2006), arXiv:astro-ph/0603021.

[235] http://www.sciops.esa.int/integral.

[236] B. J. Teegarden and K. Watanabe, Astrophys. J. **646**, 965 (2006), arXiv:astro-ph/0604277.

[237] R. Diehl *et al.*, Nature **439**, 45 (2006), arXiv:astro-ph/0601015.

[238] H. Yuksel, J. F. Beacom, and C. R. Watson, Phys. Rev. Lett. **101**, 121301 (2008), arXiv:0706.4084.

[239] J. J. Blom, T. A. D. Paglione, and A. Carraminana, (1998), arXiv:astro-ph/9811389.

[240] http://doc.in2p3.fr/themis/celeste/.

[241] J. Lavalle *et al.*, Astron. Astrophys. **450**, 1 (2006), arXiv:astro-ph/0601298.

[242] http://www-hegra.desy.de/.

[243] HEGRA Collaboration, F. A. Aharonian *et al.*, Astron. Astrophys. **400**, 153 (2003), arXiv:astro-ph/0302347.

[244] E. Churazov *et al.*, Astron. Astrophys. **467** (2007).

[245] G. Weidenspointner *et al.*, AIP Conf. Proc. **510** (2000).

[246] A. W. Strong, I. V. Moskalenko, and O. Reimer, Astrophys. J. **613**, 956 (2004), arXiv:astro-ph/0405441.

[247] http://heasarc.nasa.gov/docs/heasarc/missions/solarmax.html.

[248] K. Watanabe, M. D. Leising, G. H. Share, and R. L. Kinzer, AIP Conf. Proc. **510** (2000).

[249] H. Yuksel and M. D. Kistler, Phys. Rev. **D78**, 023502 (2008), arXiv:0711.2906.

[250] G. D. Mack, T. D. Jacques, J. F. Beacom, N. F. Bell, and H. Yuksel, Phys. Rev. **D78**, 063542 (2008), arXiv:0803.0157.

[251] G. Vertongen and C. Weniger, (2011), arXiv:1101.2610.

[252] A. A. Abdo *et al.*, Phys. Rev. Lett. **104**, 091302 (2010), arXiv:1001.4836.

[253] D. Hooper, Phys. Rev. **D77**, 123523 (2008), arXiv:0801.4378.

[254] S. Profumo, Phys. Rev. **D77**, 103510 (2008), arXiv:0801.0740.

[255] G. Servant and T. M. P. Tait, Nucl. Phys. **B650**, 391 (2003), arXiv:hep-ph/0206071.

[256] H.-C. Cheng, J. L. Feng, and K. T. Matchev, Phys. Rev. Lett. **89**, 211301 (2002), arXiv:hep-ph/0207125.

[257] D. Hooper and G. D. Kribs, Phys. Rev. **D70**, 115004 (2004), arXiv:hep-ph/0406026.

[258] R. Harnik and G. D. Kribs, Phys. Rev. **D79**, 095007 (2009), arXiv:0810.5557.

[259] R. Aloisio, P. Blasi, and A. V. Olinto, JCAP **0405**, 007 (2004), arXiv:astro-ph/0402588.

[260] E. Borriello, A. Cuoco, and G. Miele, (2008), arXiv:0809.2990.

[261] L. Zhang and G. Sigl, JCAP **0809**, 027 (2008), arXiv:0807.3429.

[262] P. Grajek, G. Kane, D. J. Phalen, A. Pierce, and S. Watson, (2008), arXiv:0807.1508.

[263] T. E. Jeltema and S. Profumo, (2008), arXiv:0805.1054.

[264] A. Birkedal, K. T. Matchev, M. Perelstein, and A. Spray, (2005), arXiv:hep-ph/0507194.

[265] L. Bergstrom, T. Bringmann, M. Eriksson, and M. Gustafsson, Phys. Rev. Lett. **95**, 241301 (2005), arXiv:hep-ph/0507229.

[266] D. R. G. Schleicher, S. C. O. Glover, R. Banerjee, and R. S. Klessen, (2008), arXiv:0809.1523.

[267] M. E. Peskin and D. V. Schroeder, *An Introduction to Quantum Field Theory* (Addison-Wesley, Reading, 1995).

[268] F. A. Berends and A. Bohm, *High Energy Electron-Positron Physics, Chapter 2* (World Scientific, Singapore, 1998, edited by A. Ali and P. Soding).

[269] H. U. Martyn, *Quantum Electrodynamics, Chapter 5* (World Scientific, Singapore, 1990, edited by T. Kinoshita).

[270] PAMELA Collaboration, O. Adriani *et al.*, Phys. Rev. Lett. **105**, 121101 (2010), arXiv:1007.0821.

[271] C. C. Nishi, Am. J. Phys. **73**, 1160 (2005), arXiv:hep-ph/0412245.

[272] C. Itzykson and J. B. Zuber, New York, Usa: Mcgraw-hill (1980) 705 P.(International Series In Pure and Applied Physics).

[273] Y. Takahashi, Porgress in Quantum Field Theory, ed. H. Ezawa and S. Kamefuchi (North Holland, Amsterdam, 1986) .

[274] S. Weinberg, Cambridge, UK: Univ. Pr. (1995) 609 p.

[275] M. Srednicki, *Quantum Field Theory* (Cambridge, UK: Univ. Pr. 641 p, 2007).

[276] H. Goldberg, Phys. Rev. Lett. **50**, 1419 (1983).

[277] L. M. Krauss, Nucl.Phys. **B227**, 556 (1983), Revised version.

[278] H. E. Haber and G. L. Kane, Phys. Rept. **117**, 75 (1985).

[279] E. Ma, Phys. Rev. Lett. **86**, 2502 (2001), arXiv:hep-ph/0011121.

[280] G. B. Gelmini, E. Osoba, and S. Palomares-Ruiz, Phys. Rev. **D81**, 063529 (2010), arXiv:0912.2478.

[281] L. D. Landau and E. M. Lifschitz, *The Classical Theory of Fields*, 4^{th} revised english edition, pages 32-34 ed. (Pergamon Press, 1975).

[282] T. Sjostrand, S. Mrenna, and P. Z. Skands, JHEP **05**, 026 (2006), arXiv:hep-ph/0603175.

[283] T. Sjostrand, S. Mrenna, and P. Z. Skands, Comput. Phys. Commun. **178**, 852 (2008), arXiv:0710.3820.

[284] J. A. R. Cembranos, A. de la Cruz-Dombriz, A. Dobado, R. A. Lineros, and A. L. Maroto, (2010), arXiv:1009.4936.

[285] A. W. Strong and I. V. Moskalenko, Astrophys. J. **509**, 212 (1998), arXiv:astro-ph/9807150.

[286] http://galprop.stanford.edu/.

[287] E. A. Baltz and J. Edsjo, Phys. Rev. **D59**, 023511 (1998), arXiv:astro-ph/9808243.

[288] T. Delahaye, R. Lineros, F. Donato, N. Fornengo, and P. Salati, Phys. Rev. **D77**, 063527 (2008), arXiv:0712.2312.

[289] J. Hisano, S. Matsumoto, O. Saito, and M. Senami, Phys. Rev. **D73**, 055004 (2006), arXiv:hep-ph/0511118.

[290] F. Donato, N. Fornengo, D. Maurin, and P. Salati, Phys. Rev. **D69**, 063501 (2004), arXiv:astro-ph/0306207.

[291] Particle Data Group, K. Nakamura *et al.*, J. Phys. **G37**, 075021 (2010).

[292] P. Grajek and K. Hagiwara, (2010), arXiv:1012.0587.

[293] M. Cirelli *et al.*, JCAP **1103**, 051 (2011), arXiv:1012.4515.

[294] R. M. Crocker, N. F. Bell, C. Balazs, and D. I. Jones, Phys. Rev. **D81**, 063516 (2010), arXiv:1002.0229.

A

Initial $(\chi\chi)$ or final $(\nu\nu)$ state Majorana fermions

Two identical fermions comprise a Majorana pair. A fermion pair can have total spin S in the symmetric state $S = 1$ or in the antisymmetric state $S = 0$. The parity of the two-fermion state is $P = (-)^{L+1}$, where L is the orbital angular momentum of the pair. This parity formula holds for both Dirac and Majorana pairs. The negative intrinsic parity of the pair, independent of the orbital parity $(-)^L$, is the same for Dirac and Majorana pairs for different reasons. In the Dirac case, the u and v spinors (equivalently, the positive and negative energy states) are independent and have opposite parity corresponding to the ± 1 eigenvalues of the parity operator γ^0. Reinterpreting the two spinor types, or positive and negative energy states, as particle and antiparticle, then leads directly to opposite intrinsic parity for the particle-antiparticle pair. In the Majorana case, the fermion has intrinsic parity $\pm i$, and so the two-particle state has intrinsic parity $(\pm i)^2 = -1$.

On general grounds, the L^{th} partial wave contribution to the annihilation rate is suppressed as v^{2L}, where v is the relative velocity between the heavy, non-relativistic $\chi\chi$ pair. The virial velocity in our Galactic halo is only $v \sim 300$ km/s $\sim 10^{-3}c$, so even for $L = 1$ the suppression is considerable. Thus only the $L = 0$ partial wave gives an unsuppressed annihilation rate in today's Universe. The $L \geq 2$ states are too suppressed to contribute to observable rates.

A Majorana pair is even under charge-conjugation (particle-antiparticle exchange), and so from the general relation $C = (-)^{L+S} = +1$ one infers that L and S must be either both even, or both odd for the pair. The origin of the $C = (-)^{L+S} = +1$ rule is as follows: Under particle-antiparticle exchange, the spatial wave function contributes $(-)^L$, and the spin wave function contributes $(+1)$ if in the symmetric triplet $S = 1$ state, and (-1) if in the antisymmetric $S = 0$ singlet state, i.e., $(-)^{S+1}$. In addition, there is an overall (-1) from anti-commutation of the two particle-creation operators $b^\dagger d^\dagger$ for the Dirac case, and $b^\dagger b^\dagger$ for the Majorana case.

Consider the $L \leq 2$ states. In spectroscopic notation ${}^{(2S+1)}L_J$ and spin-parity notation (J^{PC}), the vector ${}^3S_1$ (1^{--}), C-odd axial vector ${}^1P_1$ (1^{+-}), and assorted ${}^3D_J$ (J^{--}) states are all C-odd and therefore disallowed. The pseudoscalar ${}^1S_0$ (0^{-+}), scalar ${}^3P_0$ (0^{++}), axial vector ${}^3P_1$ (1^{++}), C-even tensor ${}^3P_2$ (2^{++}), and pseudotensor ${}^1D_2$ (2^{-+}) are all C-even and therefore allowed. In particular, the sole $L = 0$ state, with no v^{2L} suppression, is the pseudoscalar ${}^1S_0$ (0^{-+}).

Incidentally, at threshold, defined by $s = (2m_\chi)^2$ or $v = \sqrt{1 - 4m_\chi^2/s} = 0$, the orbital angular momentum L is necessarily zero. With two identical Majorana fermions, the two-particle wave function must be antisymmetric under particle interchange. Since $L = 0$ at threshold, the $\chi\chi$ spatial wave function is even, and the wave function must be antisymmetrized in its spin. The antisymmetric spin wave function is the $S = 0$ state. Thus, the only contributing partial wave at threshold is the ${}^1S_0$ state. We have just seen that this is also the only state with no v^{2L} suppression, so one may expect an unsuppressed Majorana annihilation rate at threshold if and only if there is a ${}^1S_0$ partial wave.

One may also invoke CP invariance to note that the spin S of initial and final two-fermion states, Dirac or Majorana, are the same. This follows simply from $CP = (-)^{L+S}(-)^{L+1} = (-)^{S+1}$, and the fact that $S = 0$, 1 are the only possibilities for a pair of spin 1/2 particles.

What does this all mean for a model with an s-channel exchange particle coupling to Majorana bilinears? It means that among the basis fermion bilinears, the candidates are just the pseudoscalar $\bar{\Psi}i\gamma_5\Psi$ (0^{-+}), the scalar $\bar{\Psi}\Psi$ (0^{++}), and the axial vector $\bar{\Psi}\gamma^\mu\gamma_5\Psi$ (1^{++}). The vector $\bar{\Psi}\gamma^\mu\Psi$ (1^{--}), tensor $\bar{\Psi}\sigma^{\mu\nu}\Psi$ (2^{+-}), and pseudotensor $\bar{\Psi}i\gamma_5\sigma^{\mu\nu}\Psi$ (2^{--}) bilinears are C-odd and therefore disallowed. The only s-channel particles which may couple to these candidate bilinears are the pseudoscalar, scalar, or axial vector.

There is some subtlety associated with the s-channel exchange of an axial-vector. The axial-vector is an $L = 1$ mode, and we have seen that this mode elicits a v^2 suppression in the rate. However, the exchange particle is off-shell (away form resonance) and so has a time-like pseudoscalar piece in addition to the axial three-vector piece. This pseudoscalar coupling is effectively $\partial_\mu\left(\bar{\Psi}\gamma^\mu\gamma_5\Psi\right)$. The weak interaction coupling of the pion to the axial vector current provides a familiar example of such a coupling. The axial current is not conserved, and so the pseudoscalar coupling is nonzero. One has $\partial_\mu\left(\bar{\Psi}\gamma^\mu\gamma_5\Psi\right) = 2im_\nu\bar{\Psi}\gamma_5\Psi - \frac{\alpha_W}{\pi}\epsilon^{\mu\nu\alpha\beta}k_\mu\lambda_\nu(k)\bar{k}_\alpha\lambda_\beta(\bar{k})$. The first term shows an m_ν-dependence in the amplitude, leading to $(m_\nu/m_\chi)^2$ helicity-suppression of the $L = 0$ piece, while the second term is the famous anomalous VVA coupling. It offers W^+W^- and ZZ production (with momenta k, $\bar{k}$ and helicities $\lambda(k)$, $\lambda(\bar{k})$), but at higher order $\alpha_W = g_V^2/4\pi$ in the electroweak $W\nu\nu$ or $Z\nu\nu$ coupling g_V. The linear combination of a v^2-suppressed $L = 1$ piece and a m_f^2-suppressed $L = 0$ piece to the rate from axial vector exchange was first noticed by Goldberg [276].

B

Fundamental Fierzing

In Chapter 5 we have made use of standard Fierz transformations, helicity-basis Fierz transformations, and generalizations of the two. In this Appendix, we derive these transformations. The procedure for standard Fierz transformation can be found in, e.g., [272], while more general Fierz transformations are laid down in [271]. The starting point is to define a basis $\{\Gamma^B\}$ and a dual basis $\{\Gamma_B\}$, each spanning 4×4 matrices over the complex number field $\mathcal{C}$, such that an orthogonality relation holds. The standard Fierz transformation uses the "hermitian" bases

$$\{\Gamma^B\} = \{\mathbb{1}, i\gamma_5, \gamma^\mu, \gamma_5\gamma^\mu, \sigma^{\mu\nu}\}\,, \quad \text{and} \quad \{\Gamma_B\} = \{\mathbb{1}, (-i\gamma_5), \gamma_\mu, (-\gamma_5\gamma_\mu), \frac{1}{2}\sigma_{\mu\nu}\}\,, \tag{B.1}$$

respectively. Because of their Lorentz and parity transformation properties, these basis matrices and their duals are often labeled as S and $\tilde{S}$ (scalars), P and $\tilde{P}$ (pseudoscalars), V and $\tilde{V}$ (vectors, four for V, four for $\tilde{V}$), A and $\tilde{A}$ (axial vector, four for A, four for $\tilde{A}$), and T and $\tilde{T}$ (antisymmetric tensor, six for T, six for $\tilde{T}$). As usual, spacetime indices are lowered with the Minkowski metric, $\gamma_5 = \gamma^5 = i\gamma^0\gamma^1\gamma^2\gamma^3$, $\sigma^{\mu\nu} \equiv \frac{i}{2}[\gamma^\mu, \gamma^\nu]$, (and $\gamma^5\sigma^{\mu\nu} = \frac{i}{2}\epsilon^{\mu\nu\alpha\beta}\sigma_{\alpha\beta}$). Note the change of sign between the the basis and dual for the P and A matrices. The bases are "hermitian" in that $\gamma^0\,\Gamma_B^\dagger\gamma^0 = \Gamma_B$, so that the associated Dirac bilinears satisfy $[\bar{\Psi}_1\Gamma^B\Psi_2]^\dagger = \bar{\Psi}_2\Gamma^B\Psi_1$ and $[\bar{\Psi}_1\Gamma_B\Psi_2]^\dagger = \bar{\Psi}_2\Gamma_B\Psi_1$. Importantly, we have $\Gamma_B = (\Gamma^B)^{-1}$ in the sense of the accompanying orthogonality relation

$$Tr\,[\Gamma_C\,\Gamma^B\,] = 4\,\delta_C^B\,, \quad B,\,C = 1,\ldots,16\,. \tag{B.2}$$

Note that the factor of $\frac{1}{2}$ in the definition of $\tilde{T} = \frac{1}{2}\sigma_{\mu\nu}$ (but not in $T = \sigma^{\mu\nu}$) provides the normalization required by Eqn. B.2:

$$Tr\,[\Gamma_B\,\Gamma^B]_{(\text{nosum})} = \sum_C Tr\,[\Gamma_C\,\Gamma^B] = 4\,. \tag{B.3}$$

The orthogonality relation allows us to expand any 4×4 complex matrix X in terms of the basis as

$$\begin{aligned} \mathrm{X} &= \mathrm{X}_B\,\Gamma^B = \mathrm{X}^B\,\Gamma_B\,, \quad \text{with} \quad \mathrm{X}_B = \frac{1}{4}Tr\,[\,\mathrm{X}\,\Gamma_B\,]\,,\ \text{and}\ \mathrm{X}^B = \frac{1}{4}Tr\,[\,\mathrm{X}\,\Gamma^B\,]\,, \\ \text{i.e.,}\quad \mathrm{X} &= \frac{1}{4}\,Tr\,[\mathrm{X}\,\Gamma^B]\,\Gamma_B = \frac{1}{4}\,Tr\,[\mathrm{X}\,\Gamma_B]\,\Gamma^B\,. \end{aligned} \tag{B.4}$$

One readily finds that the particular matrix element $(\mathrm{X})_{ab}$ satisfies

$$(\mathrm{X})_{cd}\,\delta_{db}\,\delta_{ac} = \frac{1}{4}\,[(\mathrm{X})_{cd}\,(\Gamma_B)_{dc}\,]\,(\Gamma^B)_{ab}\,. \tag{B.5}$$

Since each element $(\mathrm{X})_{cd}$ is arbitrary, Eqn. B.5 is equivalent to a completeness relation

$$(\mathbb{1})\,[\mathbb{1}] = \frac{1}{4}\,(\Gamma_B\,]\,[\Gamma^B\,) = \frac{1}{4}\,(\Gamma^B\,]\,[\Gamma_B\,)\,, \tag{B.6}$$

where we have adopted Takahashi's notation [273] where matrix indices are replaced by parentheses $(\cdots)$ and brackets $[\cdots]$, in an obvious way. Thus, any 4×4 matrices X and Y may be expressed as

$$(\mathrm{X})\,[\mathrm{Y}] = (\mathrm{X}\mathbb{1})\ [\mathbb{1}\mathrm{Y}] = \frac{1}{4}\,(\mathrm{X}\,\Gamma^B\,\mathrm{Y}\,]\ [\,\Gamma_B\,) = \frac{1}{4^2}\,Tr\,[\mathrm{X}\,\Gamma^B\,\mathrm{Y}\,\Gamma_C]\ (\Gamma^C\,]\ [\Gamma_B\,)\,. \tag{B.7}$$

Alternatively, we may express any 4×4 matrices X and Y as

$$(\mathrm{X})\,[\mathrm{Y}] = (\mathrm{X}\mathbb{1})\ [Y\mathbb{1}] = \frac{1}{4}\,(\mathrm{X}\,\Gamma^B]\ [Y\,\Gamma_B\,) = \frac{1}{4^3}\,Tr\,[\mathrm{X}\,\Gamma^B\,\Gamma_C]\,Tr\,[\mathrm{Y}\,\Gamma_B\,\Gamma^D]\,(\Gamma^C\,]\,[\Gamma_D\,)\,. \tag{B.8}$$

The RHS's of Eqns. B.7 and B.8 offer two useful options for Fierzing matrices. The first option sandwiches both LHS matrices into one of the two spinor bilinears, and ultimately into a single long trace. The second option sandwiches each LHS matrix into a separate spinor bilinear, and ultimately into separate trace factors. Eqn. B.7 seems to be more useful than B.8. One use we will make of Eqn. B.7 will be to express chiral vertices in terms of Fierzed standard vertices. But first we reproduce the standard Fierz transformation rules by setting X = Γ^D and Y = Γ_E in Eqn. B.7, to wit:

$$(\Gamma^D)\,[\Gamma_E] = \frac{1}{4^2}\,Tr\,[\Gamma^D\,\Gamma^B\,\Gamma_E\,\Gamma_C]\,(\Gamma^C]\,[\Gamma_B)\,. \tag{B.9}$$

(An additional minus sign arises if the matrices are sandwiched between anticommuting field operators, rather than between Dirac spinors.) Evaluation of the trace in Eqn. B.9 for the various choices of (B, C) leads to the oft-quoted result [272]

$$\begin{pmatrix} (S)\;[\tilde{S}] \\ (V)\;[\tilde{V}] \\ (T)\;[\tilde{T}] \\ (A)\;[\tilde{A}] \\ (P)\;[\tilde{P}] \end{pmatrix} = \frac{1}{4}\begin{pmatrix} 1 & 1 & 1 & 1 & 1 \\ 4 & -2 & 0 & 2 & -4 \\ 6 & 0 & -2 & 0 & 6 \\ 4 & 2 & 0 & -2 & -4 \\ 1 & -1 & 1 & -1 & 1 \end{pmatrix}\begin{pmatrix} (S]\;[\tilde{S}) \\ (V]\;[\tilde{V}) \\ (T]\;[\tilde{T}) \\ (A]\;[\tilde{A}) \\ (P]\;[\tilde{P}) \end{pmatrix}. \tag{B.10}$$

More relevant for us, as will be seen, is the ordering P, S, A, V, T, which leads to a Fierz matrix obtained from the one above with the swapping of matrix indices $1 \to 2 \to 4 \to 3 \to 5 \to 1$. The result is

$$\begin{pmatrix} (P)\;[\tilde{P}] \\ (S)\;[\tilde{S}] \\ (A)\;[\tilde{A}] \\ (V)\;[\tilde{V}] \\ (T)\;[\tilde{T}] \end{pmatrix} = \frac{1}{4}\begin{pmatrix} 1 & 1 & -1 & -1 & 1 \\ 1 & 1 & 1 & 1 & 1 \\ -4 & 4 & -2 & 2 & 0 \\ -4 & 4 & 2 & -2 & 0 \\ 6 & 6 & 0 & 0 & -2 \end{pmatrix}\begin{pmatrix} (P]\;[\tilde{P}) \\ (S]\;[\tilde{S}) \\ (A]\;[\tilde{A}) \\ (V]\;[\tilde{V}) \\ (T]\;[\tilde{T}) \end{pmatrix}. \tag{B.11}$$

(The zeroes make it clear that Fierzing induces no coupling between tensor interactions and vector and axial vector interactions.) As an example of how to read this matrix,

$$(A)\;[\tilde{A}] = -(P]\;[\tilde{P}) + (S]\;[\tilde{S}) - \frac{1}{2}(A]\;[\tilde{A}) + \frac{1}{2}(V]\;[\tilde{V}), \tag{B.12}$$

or, multiplying by spinors and giving the explicit forms of the gamma-matrices,

$$\begin{aligned}&(\overline{u}\gamma_5\gamma^\mu u)\;\;(\overline{v}(-\gamma_5\gamma_\mu)v) = -\,(\overline{u}i\gamma_5 v)\;\;(\overline{v}\,(-i\gamma_5))\,u)\\ &+(\overline{u}v)\;\;(\overline{v}u) - \frac{1}{2}\,(\overline{u}\gamma_5\gamma^\mu v)\;\;(\overline{v}\,(-\gamma_5\gamma_\mu)\,u) + \frac{1}{2}\,(\overline{u}\gamma^\mu v)\;\;(\overline{v}\gamma_\mu u)\,.\end{aligned} \tag{B.13}$$

The Fierz matrix M for the standard basis is nonsingular, and hence has five nonzero eigenvalues λ_j. Since two swaps of Dirac indices returns the indices to their original order, the matrix is idempotent, with $M^2 = \mathbb{1}$, or equivalently, $M^{-1} = M$. Accordingly, the five eigenvalues satisfy $\lambda_j^2 = 1$, so individual eigenvalues must be $\lambda_j = \pm 1$. Also, the corresponding eigenvectors are invariant under the interchange of two Dirac indices. In Table B.1 we list the eigenvalues and "Fierz-invariant" eigenvectors.

Table B.1: Fierz-invariant combinations in the standard basis.

Fierz-invariant combination	eigenvalue
$3\;(S\otimes\tilde{S} + P\otimes\tilde{P}) + T\otimes\tilde{T}$	$+1$
$2\;(S\otimes\tilde{S} - P\otimes\tilde{P}) + (V\otimes\tilde{V} + A\otimes\tilde{A})$	$+1$
$V\otimes\tilde{V} - A\otimes\tilde{A}$	-1
$S\otimes\tilde{S} + P\otimes\tilde{P} - T\otimes\tilde{T}$	-1
$2\;(S\otimes\tilde{S} - P\otimes\tilde{P}) - (V\otimes\tilde{V} + A\otimes\tilde{A})$	-1

Helicity projection operators are often present in theories where the DM couple to the $SU(2)$ lepton doublet, so it is worth considering Fierz transformations in the more convenient chiral basis.

One derivation of chiral Fierz transformations utilizes the following chiral bases (hatted) [271]:

$$\begin{aligned}\{\hat{\Gamma}^B\} &= \{P_R,\, P_L,\, P_R\gamma^\mu,\, P_L\gamma^\mu,\, \frac{1}{2}\sigma^{\mu\nu}\}\,,\\ \text{and}\quad \{\hat{\Gamma}_B\} &= \{P_R,\, P_L,\, P_L\gamma_\mu,\, P_R\gamma_\mu,\, \frac{1}{2}\,\sigma_{\mu\nu}\}\,,\end{aligned} \tag{B.14}$$

where $P_R \equiv \frac{1}{2}(1+\gamma_5)$ and $P_L \equiv \frac{1}{2}(1-\gamma_5)$ are the usual helicity projectors. The orthogonality property between the chiral basis and its dual is

$$Tr\,[\hat{\Gamma}_C\,\hat{\Gamma}^B\,] = 2\,\delta^B_C\,, \quad B, C = 1, \ldots, 16\,, \tag{B.15}$$

which implies the normalization

$$Tr\,[\hat{\Gamma}_B\,\hat{\Gamma}^B]_{(\text{no sum})} = \sum_C Tr\,[\hat{\Gamma}_C\,\hat{\Gamma}^B] = 2\,. \tag{B.16}$$

Notice that because $\{\gamma_5, \gamma^\mu\} = 0$, the dual of $P_R\gamma^\mu$ is $P_L\gamma_\mu$, and the dual of $P_L\gamma^\mu$ is $P_R\gamma_\mu$. Notice also that the normalization for the chiral bases necessitates factors of $\frac{1}{2}$ in both $\hat{T} = \frac{1}{2}\sigma^{\mu\nu}$ and $\tilde{\hat{T}} = \frac{1}{2}\sigma_{\mu\nu}$, in contrast to the tensor elements of the standard bases, given in Eqn. B.1.

In the chiral basis, one is led to a general expansion

$$\mathrm{X} = \frac{1}{2}\,Tr\,[\mathrm{X}\,\hat{\Gamma}^B]\,\hat{\Gamma}_B = \frac{1}{2}\,Tr\,[\mathrm{X}\,\hat{\Gamma}_B]\,\hat{\Gamma}^B\,, \tag{B.17}$$

and to a completeness relation

$$(\mathbb{1})\,[\mathbb{1}] = \frac{1}{2}\,(\hat{\Gamma}_B\,]\,[\hat{\Gamma}^B\,) = \frac{1}{2}\,(\hat{\Gamma}^B\,]\,[\hat{\Gamma}_B\,)\,. \tag{B.18}$$

Thus, any 4×4 matrices X and Y may be expressed as

$$(\mathrm{X})\,[\mathrm{Y}] = (\mathrm{X}\mathbb{1})\,[\mathbb{1}\mathrm{Y}] = \frac{1}{2}(\mathrm{X}\,\hat{\Gamma}_B\,\mathrm{Y}\,]\,[\,\hat{\Gamma}^B\,) = \frac{1}{4}\,Tr\,[\mathrm{X}\,\hat{\Gamma}^C\,\mathrm{Y}\,\hat{\Gamma}_B]\;(\hat{\Gamma}^B\,]\,[\hat{\Gamma}_C\,)\,. \tag{B.19}$$

Substituting $\mathrm{X} = \hat{\Gamma}^D$ and $\mathrm{Y} = \hat{\Gamma}_E$ into Eqn. B.19, one gets

$$(\hat{\Gamma}^D)\,[\hat{\Gamma}_E] = \frac{1}{4}\,Tr\,[\hat{\Gamma}^D\,\hat{\Gamma}^C\,\hat{\Gamma}_E\,\hat{\Gamma}_B]\;(\hat{\Gamma}^B]\;[\hat{\Gamma}_C)\,. \tag{B.20}$$

Evaluating the trace in Eqn. B.20 leads to the chiral-basis analog of B.10 or B.11, presented in Eqn. 5.5 of the main text.

As a check, we note that the matrix M in Eqn. 5.5 is idempotent, $M^2 = \mathbb{1}$, as it must be. The eigenvalues are therefore ±1. Eigenvalues and Fierz-invariant eigenvectors for the chiral basis are given in Table B.2. The final two eigenvectors

Table B.2: Fierz-invariant combinations in the chiral basis.

Fierz-invariant combination	eigenvalue
$3\,(P_R \otimes P_R + P_L \otimes P_L) + \hat{T} \otimes \tilde{\hat{T}}$	$+1$
$2\,P_R \otimes P_L + P_R\gamma^\mu \otimes P_L\gamma_\mu$	$+1$
$2\,P_L \otimes P_R + P_L\gamma^\mu \otimes P_R\gamma_\mu$	$+1$
$P_R \otimes P_R + P_L \otimes P_L - \hat{T} \otimes \tilde{\hat{T}}$	-1
$2\,P_R \otimes P_L - P_R\gamma^\mu \otimes P_L\gamma_\mu$	-1
$2\,P_L \otimes P_R - P_L\gamma^\mu \otimes P_R\gamma_\mu$	-1
$P_R\gamma^\mu \otimes P_R\gamma_\mu$	-1
$P_L\gamma^\mu \otimes P_L\gamma_\mu$	-1

in the Table simply express again the invariance of $V \pm A$ interactions under Fierz-transposition of Dirac indices. This invariance is also evident in the diagonal nature of the bottom two rows of the matrix 5.5.

One may instead want the Fierz transformation that takes chiral bilinears to standard bilinears. Since models are typically formulated in terms of chiral fermions, a projection onto standard s-channel bilinears would be well- suited for a partial wave analysis. Since different partial waves do not interfere with one another, the calculation simplifies in terms of s-channel partial waves.

Setting X $= \hat{\Gamma}^D$ and Y $= \hat{\Gamma}_E$ in Eqn. B.7, we readily get

$$(\hat{\Gamma}^D)\,[\hat{\Gamma}_E] = \frac{1}{4^2}\,Tr\,[\hat{\Gamma}^D\,\Gamma^B\,\hat{\Gamma}_E\,\Gamma_C]\,(\Gamma^C]\,[\Gamma_B)\,. \tag{B.21}$$

We (should) get the same result by resolving the RHS vector in Eqn. 5.5 into standard basis matrices. The result is

$$\begin{pmatrix} (P_R)\,[P_R] \\ (P_L)\,[P_L] \\ (P_R\gamma^\mu)\,[P_L\gamma_\mu] \\ (P_L\gamma^\mu)\,[P_R\gamma_\mu] \\ (\hat{T})\,[\hat{T}] \\ (\gamma_5\hat{T})\,[\hat{T}] \\ (P_R)\,[P_L] \\ (P_L)\,[P_R] \\ (P_R\gamma^\mu)\,[P_R\gamma_\mu] \\ (P_L\gamma^\mu)\,[P_L\gamma_\mu] \end{pmatrix} = \frac{1}{8} \left(\begin{array}{rrrrrr|rrrr} 1 & 1 & 1 & 1 & 1 & 1 & 0 & 0 & 0 & 0 \\ 1 & 1 & -1 & -1 & 1 & -1 & 0 & 0 & 0 & 0 \\ 4 & -4 & 4 & -4 & 0 & 0 & 0 & 0 & 0 & 0 \\ 4 & -4 & -4 & 4 & 0 & 0 & 0 & 0 & 0 & 0 \\ 6 & 6 & 0 & 0 & -2 & 0 & 0 & 0 & 0 & 0 \\ 0 & 0 & 6 & 6 & 0 & 2 & 0 & 0 & 0 & 0 \\ \hline 0 & 0 & 0 & 0 & 0 & 0 & 1 & -1 & 1 & -1 \\ 0 & 0 & 0 & 0 & 0 & 0 & 1 & -1 & -1 & 1 \\ 0 & 0 & 0 & 0 & 0 & 0 & -2 & -2 & -2 & -2 \\ 0 & 0 & 0 & 0 & 0 & 0 & -2 & -2 & 2 & 2 \end{array}\right) \begin{pmatrix} (\mathbb{1}]\,[\mathbb{1}) \\ (\gamma_5]\,[\gamma_5) \\ (\gamma_5]\,[\mathbb{1}) \\ (\mathbb{1}]\,[\gamma_5) \\ (T]\,[\tilde{T}) \\ (\gamma_5 T]\,[\tilde{T}) \\ (\gamma^\mu]\,[\gamma_\mu) \\ (\gamma_5\gamma^\mu]\,[\gamma_5\gamma_\mu) \\ (\gamma_5\gamma^\mu]\,[\gamma_\mu) \\ (\gamma^\mu]\,[\gamma_5\gamma_\mu) \end{pmatrix}$$

All relations are invariant under the simultaneous interchanges $P_R \leftrightarrow P_L$ and $\gamma_5 \to -\gamma_5$. This matrix, relating two different bases, is not idempotent. In fact, it is singular.

C

Non-Relativistic and Extreme-Relativistic Limits of Fermion Bilinears

We work in the chiral representation of the Dirac algebra, and we follow the notation of [267]. Accordingly,

$$\gamma_0 = \begin{pmatrix} 0 & \mathbb{1} \\ \mathbb{1} & 0 \end{pmatrix} , \quad \vec{\gamma} = \begin{pmatrix} 0 & \vec{\sigma} \\ -\vec{\sigma} & 0 \end{pmatrix} , \quad \gamma_5 = \begin{pmatrix} -\mathbb{1} & 0 \\ 0 & \mathbb{1} \end{pmatrix} . \tag{C.1}$$

The rest-frame four-spinor is

$$u(\vec{p} = 0) = \sqrt{M} \begin{pmatrix} \xi \\ \xi \end{pmatrix} , \tag{C.2}$$

where ξ is a two-dimensional spinor. The spinor with arbitrary momentum is obtained by boosting. One gets

$$u(p) = \begin{pmatrix} \sqrt{p \cdot \sigma}\, \xi \\ \\ \sqrt{p \cdot \overline{\sigma}}\, \xi \end{pmatrix} , \tag{C.3}$$

where $\sigma \equiv (1, \vec{\sigma})$ and $\overline{\sigma} \equiv (1, -\vec{\sigma})$.

In a standard fashion, we choose the up and down spin eigenstates of σ_3 as the basis for the two-spinors. These basis two-spinors are

$$\xi_+ \equiv \begin{pmatrix} 1 \\ 0 \end{pmatrix}, \quad \xi_- \equiv \begin{pmatrix} 0 \\ 1 \end{pmatrix}. \tag{C.4}$$

In terms of the chosen basis, we have for the NR u-spinors,

$$u_\pm \xrightarrow{NR} \sqrt{M} \begin{pmatrix} \xi_\pm \\ \xi_\pm \end{pmatrix}. \tag{C.5}$$

We get the ER limit of the u-spinors from Eqn. C.3. After a bit of algebra, one finds

$$u_+ \xrightarrow{ER} \sqrt{2E} \begin{pmatrix} 0 \\ 0 \\ \xi_+ \end{pmatrix}, \quad u_- \xrightarrow{ER} \sqrt{2E} \begin{pmatrix} \xi_- \\ 0 \\ 0 \end{pmatrix}. \tag{C.6}$$

The arbitrary v-spinor is given by

$$v(p) = \begin{pmatrix} \sqrt{p \cdot \sigma}\, \eta \\ \\ -\sqrt{p \cdot \overline{\sigma}}\, \eta \end{pmatrix}. \tag{C.7}$$

In the Dirac bilinear the two-spinor η is independent of the two-spinor xi, and so it is given an independent name, η. However, the basis $\eta^\pm$ remains $\xi^\pm$ as defined above. It is the minus sign in the lower components of v relative to the upper components that distinguishes v in Eqn. C.7 from u in Eqn. C.3 in a fundamental way. After a small amount of algebra, one finds the limits

$$v_\pm \xrightarrow{NR} v_\pm(\vec{p} = 0) = \sqrt{M} \begin{pmatrix} \eta_\pm \\ -\eta_\pm \end{pmatrix}, \tag{C.8}$$

and

$$v_+ \xrightarrow{ER} \sqrt{2E} \begin{pmatrix} 0 \\ 0 \\ -\eta_+ \end{pmatrix}, \quad v_- \xrightarrow{ER} \sqrt{2E} \begin{pmatrix} \eta_- \\ 0 \\ 0 \end{pmatrix}. \tag{C.9}$$

Finally, we apply the above to determine the values of Dirac bilinears in the NR and ER limits. The $\bar{u} \equiv u^\dagger \gamma_0$ and $\bar{v} \equiv v^\dagger \gamma_0$ conjugate spinors are are easily found from the u and v spinors. We let Γ denote any of the hermitian basis Dirac-matrices $\{\mathbb{1},\ i\,\gamma_5,\ \gamma^\mu,\ \gamma_5\,\gamma^\mu,\ \sigma^{\mu\nu}\}$. Then, the NR limit of $\bar{u}(p_1)\,\Gamma\,v(p_2)$ is just

$$\bar{u}(p_1)\,\Gamma\,v(p_2) \xrightarrow{NR} M\left[(\xi_1,\ \xi_1)\ \Gamma\begin{pmatrix} \eta_2 \\ -\eta_2 \end{pmatrix}\right]. \tag{C.10}$$

Non-relativistic results for the various choices of basis Γ's and spin combinations are listed in Table 5.2 of the text.

To give a succinct formula for the ER limit of $\bar{u}(p_1)\,\Gamma\,v(p_2)$, we take $\hat{p}_1 = -\hat{p}_2 = \hat{3}$, i.e. we work in a frame where $\hat{p}_1$ and $\hat{p}_2$ are collinear, and we quantize the spin along this collinear axis. The result is

$$\bar{u}(p_1)\,\Gamma\,v(p_2) \xrightarrow{ER} \sqrt{4E_1E_2}\ \left[\xi_1\ \ (\Lambda_+,\ \Lambda_-)\,\Gamma\begin{pmatrix} \Lambda_+ \\ -\Lambda_- \end{pmatrix}\ \eta_2\right], \tag{C.11}$$

where the matrices $\Lambda_\pm$ are just up and down spin projectors along the quantization axis $\hat{3}$:

$$\lambda_+ = \begin{pmatrix} 1 & 0 \\ 0 & 0 \end{pmatrix}, \quad \Lambda_- = \begin{pmatrix} 0 & 0 \\ 0 & 1 \end{pmatrix}. \tag{C.12}$$

Extreme-relativistic results for the various choices of basis Γ's and spin combinations are listed in Table 5.2.

D

s-channel Cross Sections

In Section 5.2.2 we found a general way to determine the suppression of s-channel DM annihilation to a lepton pair. To test our conclusions, we explicitly calculate the cross section for some of these processes. First we present a convenient form of the phase space integral for these processes,

$$d\sigma = \frac{1}{2\sqrt{s(s-4m_\chi^2)}}\frac{1}{4}\sum_{\text{spins}}|\mathcal{M}|^2\delta^4(k_1+k_2-p_1-p_2)\frac{d^3p_1\,d^3p_2}{16\pi^2 E_\ell E_{\bar{\ell}}}. \tag{D.1}$$

Performing the integral over d^3p_1, and moving to the center of momentum frame,

$$\begin{aligned}\sigma &= \int \frac{1}{2\sqrt{s(s-4m_\chi^2)}}\frac{1}{4}\sum_{\text{spins}}|\mathcal{M}|^2\delta(2E_\chi-2E_\ell)\frac{\sqrt{E_\ell-m_\ell}}{E_\ell}dE_\ell d\Omega \\ &= \int_{-1}^{1}\int_0^{2\pi}\frac{1}{2^6\pi^2 s}\sqrt{\frac{s-4m_\ell^2}{s-4m_\chi^2}}\frac{1}{4}\sum_{\text{spins}}|\mathcal{M}|^2 d\phi d\cos\theta,\end{aligned} \tag{D.2}$$

where ϕ and θ define the direction of motion of the particles.

We now consider annihilation to a lepton pair via exchange of a scalar particle B. This is similar to the calculation performed in Section 4.2, but we now consider DM annihilation rather than B decay. The matrix element is

$$\mathcal{M}_{\chi\chi\to\ell\bar{\ell}} = \left(\bar{v}(k_2)\,f_B\,u(k_1)\right)\frac{1}{s-M_B^2}\left(\bar{u}(p_1)\,g_B\,v(p_2)\right), \tag{D.3}$$

where k_1, k_2, p_1, p_2 are the momenta of the incoming DM and outgoing leptons respectively, $s = m_\chi^2/(1-v^2)$ is the center of mass energy squared, M_B is the mass of the scalar B, and f_B, g_B are the coupling strengths of the B particle with the DM and leptons respectively. This leads to the spin-averaged matrix-element squared,

$$\begin{aligned}\frac{1}{4}\sum_{\text{spins}}|\mathcal{M}|^2 &= \frac{1}{4}\left(\frac{f_B\,g_B}{s-M_B^2}\right)^2 \mathrm{Tr}[(\not{k}_1+m_\chi)(\not{k}_2-m_\chi)]\mathrm{Tr}[(\not{p}_1+m_\ell)(\not{p}_2-m_\ell)] \\ &= 4\left(\frac{f_B\,g_B}{s-M_B^2}\right)^2 (k_1\cdot k_2-m_\chi^2)(p_1\cdot p_2-m_\ell^2) \\ &= 16\left(\frac{f_B\,g_B}{s-M_B^2}\right)^2 (s-4m_\chi^2)(s-4m_\ell^2), \qquad \boxed{\text{D.4}}\end{aligned}$$

where we have made use of Eqn. 5.41. Using Eqn. D.2, the cross section multiplied by the DM velocity is

$$\begin{aligned}v\sigma &= \frac{v}{16\pi}\left(\frac{f_B\,g_B}{s-M_B^2}\right)^2 \sqrt{s-4m_\chi^2}\,\frac{(s-4m_\ell^2)^{3/2}}{s} \\ &= \frac{v^2}{4\pi m_\chi}\left(\frac{f_B\,g_B}{4m_\chi^2-M_B^2}\right)^2 (m_\chi^2-m_\ell^2)^{3/2}+o(v^4), \qquad \boxed{\text{D.5}}\end{aligned}$$

after substituting $s \to 4m_\chi^2/(1-v^2)$, and expanding in powers of v. As expected from Table 5.2, the cross section suffers from v^2 suppression. Next we calculate the cross section for a similar process, where the DM now annihilates via a pseudoscalar B. The matrix element for this process is

$$\mathcal{M}_{\chi\chi\to\ell\bar{\ell}} = (\bar{v}(k_2)\,f_B\gamma_5\,u(k_1))\,\frac{1}{s-M_B^2}\,(\bar{u}(p_1)\,g_B\gamma_5\,v(p_2))\,, \qquad \boxed{\text{D.6}}$$

and following the same steps as above, we find the cross section,

$$v\sigma = \left(\frac{f_B\,g_B}{4m_\chi^2-M_B^2}\right)^2 \frac{m_\chi^2}{4\pi}\left(1+\left(\frac{4m_\chi^2+M_B^2}{4m_\chi^2-M_B^2}\right)v^2+o(v^4)\right). \qquad \boxed{\text{D.7}}$$

This contains an unsuppressed term of order v^0, confirming that pseudoscalar annihilation does not suffer from v^2 or helicity suppression.

Finally we have the axial-vector coupling, with matrix element

$$\mathcal{M}_{\chi\chi\to\ell\bar{\ell}} = (\bar{v}(k_2)\,f_B\gamma_\mu\gamma_5\,u(k_1))\,\frac{1}{s-M_B^2}\,(\bar{u}(p_1)\,g_B\gamma^\mu\gamma_5\,v(p_2))\,, \qquad \boxed{\text{D.8}}$$

leading to the spin-averaged matrix-element squared,

$$
\begin{aligned}
&\frac{1}{4}\sum_{\text{spins}}|\mathcal{M}|^2 = \\
&\frac{1}{4}\left(\frac{f_B\,g_B}{s-M_B^2}\right)^2 \mathrm{Tr}[(\not k_2 - m_\chi)\gamma_\mu\gamma_5(\not k_1 + m_\chi)\gamma_\nu\gamma_5]\mathrm{Tr}[(\not p_1 + m_\ell)\gamma^\mu\gamma_5(\not p_2 - m_\ell)\gamma^\nu\gamma_5] \\
&= \frac{1}{4}\left(\frac{f_B\,g_B}{s-M_B^2}\right)^2 \mathrm{Tr}[\not k_2\gamma_\mu\not k_1\gamma_\nu + m_\chi^2\gamma_\mu\gamma_\nu]\mathrm{Tr}[\not p_1\gamma^\mu\not p_2\gamma^\nu + m_\ell^2\gamma^\mu\gamma^\nu]. \qquad \text{(D.9)}
\end{aligned}
$$

Evaluating the traces and resulting dot products, we find the cross section,

$$
\begin{aligned}
v\sigma \;=\;& \int_{-1}^{1}\left(\frac{f_B\,g_B}{s-M_B^2}\right)^2 \frac{v}{2^6\pi\, s}\sqrt{\frac{s-4m_\ell^2}{s-4m_\chi^2}} \\
&\left(\left(s+\sqrt{(s-4m_\chi^2)(s-4m_\ell^2)}\cos\theta\right)^2 + \left(s-\sqrt{(s-4m_\chi^2)(s-4m_\ell^2)}\cos\theta\right)^2\right. \\
&\left. -8s(m_\chi^2+m_\ell^2) + 2^6 m_\chi^2 m_\ell^2\right) d\cos\theta \\
=\;& \left(\frac{f_B\,g_B}{4m_\chi^2-M_B^2}\right)^2 \frac{1}{4\pi}\left(\frac{m_\ell^2}{m_\chi}\sqrt{m_\chi^2-m_\ell^2}\right. \\
&\left. -\frac{4}{3}\frac{m_\chi^3 M_B^2 + m_\chi^5}{(4m_\chi^2-M_B^2)\sqrt{m_\chi^2-m_\ell^2}}v^2 + o(m_\ell^2 v^2) + o(v^4)\right), \qquad \text{(D.10)}
\end{aligned}
$$

confirming that this annihilation channel is suppressed.

Author/s:
Jacques, Thomas David

Title:
Dark matter indirect detection and Bremsstrahlung Processes

Date:
2011

Citation:
Jacques, T. D. (2011). Dark matter indirect detection and Bremsstrahlung Processes. PhD thesis, Science, School of Physics, The University of Melbourne.

Persistent Link:
http://hdl.handle.net/11343/36390

File Description:
Dark matter indirect detection and Bremsstrahlung Processes